

Department of Chemical and Environmental Engineering

Influence of geometrical parameters on gas-liquid intermittent flows.

By

Josep Escrig Escrig

Thesis submitted to the University of Nottingham

for the degree of Doctor of Philosophy

August 2017

ABSTRACT

The influence of geometrical parameters on the development of intermittent flow is studied in this thesis. The geometrical parameters considered are the diameter of the pipe, the angle of inclination of the pipe, and the distribution of the area of the gas injection.

Intermittent flow in gas-liquid two-phase flows occurs when, from a fixed point, a gas dominated structure followed by a liquid dominated structure seems to repeat at a certain mean frequency. It is mainly slug flow but churn and cap bubble flow also fall into this broad category.

Intermittent gas-liquid two-phase flow was investigated in a 67 mm diameter, 6 m long rig and also in a 127 mm diameter, 12 m long rig. The test section of the 67 mm rig was mounted in a steel frame supported by a pivot that allowed changing the inclination of the pipe from vertical to horizontal in steps of 15°. The 127 mm rig can only be operated in the upwards vertical position. The fluids utilised were air and silicon oil of viscosity = 5 cP and density = 0.912 kg/m^3. The interfacial surface tension was measured at 0.02 N/m. The facilities were both operated at atmospheric pressure. The gas superficial velocity (U_{gs}) was varied from 0.17 to 2.9 m/s and liquid superficial velocity (U_{ls}) from 0.023 to 0.47 m/s. The void fraction generated by each set of conditions was captured for 60 seconds using a Wire Mesh Sensor and a twin plane Electrical Capacitance Tomography probe.

The effect of the diameter and the angle of inclination of the pipe under different gas and liquid superficial velocities was reported. The main findings can be summarised as that the velocity of the periodic structures was found to be higher in large diameter pipes

and increases with increasing the angle of inclination reaching a maximum around 50° then decreases. In addition, the frequency of the gas structures was found to be higher in small diameter pipes and increases with increasing the inclination of the pipe for all the gas and liquid superficial velocities investigated.

Additionally, two correlations to predict the velocity and the frequency of the periodic gas structures as a function of the diameter, the inclination of the pipe, the gas superficial velocity and the liquid superficial velocity were developed. The proposed correlations were found to not only be in excellent agreement with the present experimental results (less than 20% difference), but also in good agreement with data published by other researchers. This include data produced using different fluids, different diameters of pipe and different gas and liquid superficial velocities to the ones investigated in this work.

It was also found that the gas injection area, modified using different gas-liquid mixers, do not have an influence on the development of the intermittent two-phase flows at 75 diameters axial length from the mixing point.

ACKNOWLEDGEMENTS

I would like to express my sincere gratitude to my main supervisor Dr. Buddhika Hewakandamby, for his guidance and his trust during these four years at the University of Nottingham. My appreciation goes to my second supervisors Prof. Barry Azzopardi and Dr. Gerogios Dimitrakis for their support and invaluable advice throughout the stages my PhD study.

My sincere thanks are also extended to the technical staff of L3 lab. In particular to Mel, Phil, Fred and Marion for building and assessing the rigs and the instrumentation.

Special thanks to Dr. Sergio Chiva, for recommending me as a PhD candidate to the multiphase flow group at the University of Nottingham, also for his guidance during my stay at the Universitat Jaume I. Big thanks to my colleagues during that period: Guillem, Lledó and Raul.

I would like to thank my colleagues at the University of Nottingham (Katerina, Voon Long, Shara, Zoe, Vicky, Komo, Rajab, João, Ibrahim, Matt, Yousuf and Mustapha) for the encouragement, help and good moments in academia. My thanks also go to the colleagues in the shared postgraduate room (Pablo, Miquel, Miguel Angel and Miguel) for the long discussions over lunch time.

Big thanks to the new friends that I met in Nottingham (Susana, Sergio, Paco, Helena, Monika, Sergio, Ola and Caro) for the great moments that we shared which have been essentials to finish this journey successfully.

Finally, I would like to thank my parents and my sister and all my friends and family in Atzeneta for their constant support and contact while far away.

This project was funded by TOTAL.SA and PETROBRAS.SA under the auspicious of Transient Multiphase Flow Consortium and supported by the University of Nottingham. My sincere gratitude goes to all of them for making my PhD feasible.

CONTENTS

Abstract ..... **i**

Acknowledgements ..... **iii**

Contents ..... **v**

List of figures ..... **x**

List of tables ..... **xvii**

Nomenclature ..... **xix**

CHAPTER 1. Introduction **1**

1.1 Introduction 1

1.2 Objectives 3

1.3 Methodology 4

1.3.1 Experimental 4

1.3.2 Processing of the data 6

1.3.3 Analysis and modelling 6

1.4 Structure of the thesis 6

CHAPTER 2. Literature review **9**

2.1 Introduction 9

2.1.1 Gas-liquid two-phase flow 9

2.2 Gas-liquid flow regimes 10

2.2.1 Flow patterns in vertical pipes 11

2.2.2 Flow patterns in horizontal pipes 12

2.3 Flow pattern transitions and maps 13

2.3.1 Bubbly to slug flow transition 14

2.3.2 Slug to churn flow transition 15

2.3.3 Churn to annular flow transition 16
2.3.4 Transition to dispersed flow 18
2.3.5 Flow pattern maps 18
2.4 Intermittent flows 20
2.4.1 Characterization of intermittent flow 22
2.4.1.1 Velocity of the periodic structures in intermittent flows 22
2.4.1.2 Frequency of the periodic structures in intermittent flows 24
2.5 Current limitations in the understanding of intermittent flows 27

CHAPTER 3. Experimental Arrangement 32

3.1 Fluid properties 32
3.2 Rigs description 32
3.2.1 67 mm diameter rig 33
3.2.2 127 mm diameter rig 35
3.3 Measurements of the two-phase flow 39
3.4 Measurement Techniques 40
3.4.1 Wire Mesh Sensor 41
3.4.1.1 Uncertainty of the WMS 42
3.4.2 Electrical Capacitance Tomography 43
3.4.2.1 Uncertainty of the ECT 45
3.5 Testing of the experimental facilities 46
3.5.1 Testing of the flowmeters 46
3.5.1.1 Gas flowmeters 46
3.5.1.2 Liquid flowmeters 47
3.5.2 Testing of the sensors 48
3.5.3 Testing the repeatability of the experiments 50

CHAPTER 4. Data processing and analytical methods 52

4.1 Normalized capacitance 53

4.2 Cross-sectional permittivity distribution 54
4.2.1 WMS permittivity distribution 55
4.2.2 ECT permittivity distribution 57
4.3 Void fraction cross-sectional distribution 62
4.4 Diametrical time traces 65
4.5 Cross-sectional void fraction time series 67
4.5.1 Statistical moments 67
4.5.2 Probability density function 68
4.6 Void fraction average radial distribution 69
4.7 Velocities of the gas structures 70
4.8 Identification of the gas structures 71
4.9 Frequency of the gas structures 72
4.10 Bubbles detection and bubble size distribution 75
4.11 Conclusions 79

CHAPTER 5. The influence of diameter of the pipe 81

5.1 Introduction 81
5.2 Experimental Arrangement 82
5.3 Results 83
5.3.1 Flow image reconstruction 83
5.3.2 Velocity of the gas structures 86
5.3.3 Frequency of the gas structures 88
5.4 Discussion 90
5.4.1 Velocity of the gas structures 90
5.4.2 Gas structures frequency 97
5.5 Conclusions 103

CHAPTER 6. The influence of angle of inclination 105

6.1 Introduction 105

6.2 Experimental Arrangement 106
6.3 Results 107
6.3.1 Flow image reconstruction 108
6.3.2 Gas structure velocities 111
6.3.3 Gas structure frequencies 113
6.4 Discussion 115
6.4.1 Velocity of the gas structures 115
6.4.2 Gas structures frequency 122
6.5 Conclusions 129

CHAPTER 7. The influence of gas injection 131
7.1 Introduction 131
7.2 Experimental arrangement 132
7.3 Results and discussion 134
7.4 Conclusions 143

CHAPTER 8. General discussions and conclusions 145
8.1 Introduction 145
8.2 General discussions 146
8.2.1 Velocity of the gas structures 146
8.2.2 Frequency of the gas structures 150
8.3 General conclusions 154
8.4 Recommendations of future work 156

References 157

A. Analysis of errors 162
A.1. Uncertainty of the liquid superficial velocity 162
A.2. Uncertainty of the gas superficial velocity 163
A.3. Uncertainty of the gas structure velocity 164

B. Experimental matrix and results 165

B.1. Experimental campaign 1 (Chapter 5) 165

B.2. Experimental campaign 2 (Chapter 6) 169

B.3. Experimental campaign 3 (Chapter 7) 178

LIST OF FIGURES

Figure 2.1 Main flow regimes in vertical and horizontal pipes (Bratland, 2010). 11

Figure 2.2 Taitel et al. (1980), Weisman and Kang (1981) and Mishima and Ishii (1984) flow pattern maps 19

Figure 3.1. 67 mm rig flows diagram. 34

Figure 3.2. 127 mm rig flows diagram 37

Figure 3.3. Mixer diagram 38

Figure 3.4. WMS and ECT results representation. Black is oil, white is air and yellow and orange tones are a mixture of both. 40

Figure 3.5. Simplified scheme of the wire mesh sensor (Da Silva et al., 2007) 42

Figure 3.6. Electrodes arrangement in the ECT sensor 44

Figure 3.7. Air volumetric flowmeters and a pressure gauge in the 67 mm diameter rig. 46

Figure 3.8. Calibration curves of the volumetric liquid flowmeters in the 67 mm diameter rig. 48

Figure 3.9. Different liquid levels and the image reconstructions with the WMS and the ECT in the 67 mm diameter rig. Below, void fraction (VF) of each image. 49

Figure 3.10. Different liquid levels and the image reconstructions with the WMS and the ECT in the 127 mm diameter rig. Below, void fraction (VF) of each image. 50

Figure 3.11. Comparison of the average void fraction obtained under the same conditions on different days in the 67 mm diameter rig using WMS and ECT. 51

Figure 3.12. Comparison of the average void fraction obtained under the same conditions on different days in the 127 mm diameter rig using WMS and ECT. 51

Figure 4.1. Data processing flow diagram. 53

Figure 4.2. WMS 16x16 grid. Blue continuous lines are the wires, the black circle is the pipe perimeter, the dashed black lines enclose the cells, filled green cells are inside the pipe and white cells are out of the pipe 56

Figure 4.3. ECT permittivity cells in a 32x32 grid. 58

Figure 4.4. Reconstruction of virtual images with different algorithms: LBP, SVD and Tikh. 61

Figure 4.5. Reconstruction of virtual images with different number of iterations using Tikhonov regularisation. 62

Figure 4.6. Real, parallel and series phase distribution in a cell. 63

Figure 4.7. Real void fraction against relative permittivity for parallel and serial models. 64

Figure 4.8. Diametrical time traces (400 acquisitions). The first image is WMS (24 cells in the diameter). The second image is from the ECT sensor (32 cells in the diameter). 65

Figure 4.9. DTT modified to equivalent length for WM and ECT and Us equals to 0.5, 1 and 2 m/s. 66

Figure 4.10. Void fraction time series and DTT for the same cross-section obtained over 0.3 seconds. 67

Figure 4.11. Three different void fraction time series and their corresponding PDF. They are identified as bubble, slug and churn flow. 69

Figure 4.12. Void fraction radial profiles for three different flow regimes. 0 is the centre of the pipe and 1 is the wall. 70

Figure 4.13. (a) Simultaneous ECT void fraction time series in two twin planes. (b) The second series are delayed to find the maximum cross-correlation. 70

Figure 4.14. Gas structures identification using one and two thresholds compared with the DTT. 72

Figure 4.15. Three different samples of void fraction time series and their corresponding PSD, the PSD by applying averaging and overlapping, and the frequency obtained by counting peaks. 74

Figure 4.16. Four different samples showing identified bubbles represented in different colours. 76

Figure 4.17. Number of bubbles of each size distribution considering DXY, b 77

Figure 4.18. Number of bubbles of each size distribution considering De, b..... 77

Figure 4.19. Number of bubbles of each size distribution in logarithmic scale considering De, b. 78

Figure 4.20. Void fraction of each bubble size distribution considering DXY, b 79

Figure 4.21. Void fraction of each bubble size distribution considering De, b. 79

Figure 5.1. Experimental matrix on Taitel et al. (1980) flow pattern map 83

Figure 5.2. Flow reconstruction in 67 and 127 mm pipes and four different U_{gs}. U_{ls} = 0.35 m/s..... 84

Figure 5.3. Flow reconstruction in 67 and 127 mm pipes and four different U_{gs}. U_{ls} = 0.115 m/s. Axial scale = Radial scale x10 85

Figure 5.4. Flow reconstruction in 67 and 127 mm pipes and four different U_{gs}. U_{ls} = 0.47 m/s. Axial scale = Radial scale x10 86

Figure 5.5. Velocity of the gas structures at different U_{gs} and U_{ls} and at 67 and 127 mm diameter pipes 87

Figure 5.6. Gas structures frequency at different U_{gs} and U_{ls} in 67 and 127 mm diameter pipes 89

Figure 5.7. Gas structure velocities in the 67 and 127 mm diameter pipes plotted against the mixture velocity and the fitting curves of the form of Nicklin et al. (1962)..... 91

Figure 5.8. Comparison of gas velocity experimental results with the values calculated using an equation of the form of Nicklin et al. (1962) and the drift velocity of Davies and Taylor (1950) 92

Figure 5.9. Comparison of the experimental values of the gas structure velocities with the calculated results using the proposed correlation [5.8]..... 96

Figure 5.10. Comparison of the experimental values of the gas structures velocities with the correlation function [5.8] at different U_{gs} and U_{ls} in both pipe diameters..... 96

Figure 5.11. Strouhal number based in U_{gs} plotted against the liquid volumetric fraction at the U_{ls} and U_{gs} used in the experiments of this chapter and at different diameters of the pipe..... 97

Figure 5.12. Lockhart-Martinelli parameter calculated using expression [2.35] compared with the simplified version calculated with equation [5.10] at different U_{gs} and U_{ls} and different diameters 98

Figure 5.13. Strouhal numbers calculated using U_{gs}, U_{ls}, U_{ms} and U_b plotted against Lockhart-Martinelli parameter and their regressions lines and the determination coefficient (R^2) of each line. 99

Figure 5.14. Strouhal number based in U_{gs} plotted against the modified Lockhart-Martinelli parameter (equation [5.11]) for 67 and 127 mm diameter pipe and different gas and liquid superficial velocities. 101

Figure 5.15. Comparison of the frequency experimental values with the new correlation [5.13] for different U_{ls} and for both pipe diameters. 102

Figure 6.1. Experimental matrix on both Taitel et al. (1980) and Weisman and Kang (1981) flow pattern maps 107

Figure 6.2. Flow reconstruction at different inclination angles of the pipe. The gas and liquid superficial velocities were fixed at U_{ls} = 0.35 m s-1 and U_{gs} = 0.52 m s-1,..... 108

Figure 6.3. Flow reconstruction at U_{gs}=0.17 m/s and U_{ls}=0.47 m/s at different angles. Axial scale = Radial scale x10 110

Figure 6.4. Flow reconstruction at U_{gs}=2.9 m/s and U_{ls}=0.47 m/s at different angles. Axial scale = Radial scale x10 110

Figure 6.5. Flow reconstruction at U_{gs}=0.17 m/s and U_{ls}=0.023 m/s at different angles. Axial scale = Radial scale x10 110

Figure 6.6 Flow reconstruction at U_{gs}=2.9 m/s and U_{ls}=0.023 m/s at different angles. Axial scale = Radial scale x10 110

Figure 6.7. Gas structures velocity. Each graph corresponds to one U_{ls}, the y-axis is the structure velocity, the x-axis is the angles variation and each colour line represents a different U_{gs}..... 112

Figure 6.8. Gas structures frequency. Each graph corresponds to one angle, the y-axis is the structure frequency, the x-axis is U_{gs} variation and each colour line represents a different U_{ls} 114

Figure 6.9 Fitting of the experimental data in horizontal position to a straight line considering $Vdh > 0$ (in blue) and fitting to a curve with origin in zero $Vdh = 0$ (in red) 118

Figure 6.10. Comparison of experimental results with the values calculated using the correlation of Bendiksen (1984) 120

Figure 6.11. Comparison of experimental results with the values calculated using the correlation of Hasan and Kabir (1988) 120

Figure 6.12 Comparison of experimental results with the values calculated using the correlation of Hasan and Kabir (1988) and C_0 as a function of the Reynolds number 121

Figure 6.13 Comparison of the experimental values with the correlation function [6.7] at different U_{gs} and U_{ls} and at different angles of inclination. 122

Figure 6.14 Strouhal number calculated using the U_{gs} plotted against Lockart-Martinelli parameter at different angle of inclination in logarithmic scale 123

Figure 6.15 Comparison of frequency experimental results with the values calculated using Zabaras (1999) correlation. 124

Figure 6.16 Comparison of frequency experimental results with values calculated using the new correlation [6.14] 128

Figure 6.17 Comparison of the frequency experimental values with the correlation function [6.14] at different U_{ls} and at different angles of inclination..... 128

Figure 7.1 Perforated, Concentric and Sparger mixers geometry..... 132

Figure 7.2. Gas and liquid superficial velocities chosen to test plotted on Taitel flow patterns map 134

Figure 7.3 Concentric-Perforated and Sparger-Perforated void fraction average comparison for different gas and liquid flow rates using ECT and WMS sensors.... 136

Figure 7.4 Concentric-Perforated and Sparger-Perforated void fraction standard deviation comparison for different gas and liquid flow rates using ECT and WMS sensors. 136

Figure 7.5. Probability Density Function of the void fraction in a cross section of the pipe for different U_{ls}, U_{gs} and gas-liquid mixers..... 137

Figure 7.6 Logarithmic Probability Density Function of the void fraction in a cross section of the pipe for different U_{ls}, U_{gs} and gas-liquid mixers. 138

Figure 7.7 Concentric-Perforated and Sparger-Perforated structure velocities comparison for different gas and liquid flow rates using ECT twin plane sensor. 139

Figure 7.8 Concentric-Perforated and Sparger-Perforated structures frequency comparison for different gas and liquid flow rates using ECT and WMS sensors. ... 140

Figure 7.9 Concentric-Perforated and Sparger-Perforated structures length comparison for different gas and liquid flow rates using ECT and WMS sensors..... 141

Figure 7.10. Radial distribution average of the void fraction in a cross section of the pipe for different U_{ls}, U_{gs} and gas-liquid mixers..... 142

Figure 7.11. Distribution of the void fraction in different bubbles size at different U_{ls}, U_{gs} and gas-liquid mixers..... 143

Figure 8.1. Comparison of the measured values with the calculated values at different U_{gs} and U_{ls} in 67 and 127 diameter vertical pipes..... 148

Figure 8.2. Comparison of the measured values with the calculated values at different U_{gs} and U_{ls} in a pipe of 67 mm diameter with different inclinations 148

Figure 8.3. Comparison of experimental results of Hernandez-Perez (2008) with the values calculated using the correlation [8.2]..... 149

Figure 8.4. Comparison of experimental results of Van Hout et al. (2003) with the values calculated using the correlation [8.2]..... 149

Figure 8.5. Comparison of the frequency measured values with the calculated values at different U_{gs} and U_{ls} in 67 and 127 diameter vertical pipes..... 151

Figure 8.6. Comparison of the frequency measured values with the calculated values at different U_{gs} and U_{ls} in a pipe of 67 mm diameter with different inclinations 151

Figure 8.7. Comparison of experimental results of Cheng and Burkhardt (2003) and Zheng and Che (2006) with the values calculated using the correlation [8.4]..... 154

Figure 8.8. Comparison of experimental results of Van Hout et al. (2003) with the values calculated using the correlation [8.4]..... 154

LIST OF TABLES

Table 3.1. Silicone oil and air physical properties at 20 °C and 1 bar 32

Table 3.2. The length of the electrodes of the ECT in the 67 mm pipe and the gaps between them. Distances in the axial direction in millimetres. 44

Table 3.3. The length of the electrodes of the ECT in the 127 mm pipe and the gaps between them. Distances in the axial direction in millimetres. 44

Table 5.1. Gas and liquid superficial velocities used in the experiments 82

Table 5.2. C_o, V_d, Fr and R^2 obtained at different diameters of pipe 90

Table 5.3. C_o, Fr and R^2 considering both diameters 91

Table 5.4. Parameter of C_o and Froude number 93

Table 5.5. Fitting parameter C, n, $V0$ and m and the determination coefficient R^2 95

Table 5.6. Fitting parameter A, B and C obtained adjusting the present data to the equation of Fossa et al. (2003) and the determination coefficient R^2 97

Table 5.7. *A* parameter that gives the best fitting in equation [5.11] and the determination coefficient 100

Table 5.8. A and B parameters in equation [5.12] that give better fitting with the data and the determination coefficient R^2 101

Table 6.1. Gas and liquid superficial velocities used 106

Table 6.2. C_o, V_d that fit better with the experimental results at different inclinations angles and their corresponding Froude number, Fr, and the determination coefficient, R^2 116

Table 6.3. Parameters C and n of the equation [6.2] that fit better with the experimental data in the horizontal position and the determination coefficient 118

Table 6.4. Distribution coefficient C_o, drift velocity in horizontal and vertical positions Vdh , Vdv and determination coefficient R^2 119

Table 6.5. Distribution coefficient C_o, drift velocity vertical positions Vdv and determination coefficient R^2 120

Table 6.6. Fitting parameters C and n, velocity in vertical positions Vdv and determination coefficient R^2 121

Table 6.7. Parameters a and b of equation [6.8] that give better fitting with the experimental data and the determination coefficients R^2 124

Table 6.8. Coefficients given to equation [6.10] and the determination coefficient obtained after compared them with the experimental results. 126

Table 7.1. Gas and liquid superficial velocities used in the experiments 133

Table 8.1. Fitting parameters and determination coefficient 147

Table 8.2. Experimental conditions of the present experiments, Hernandez-Perez (2008) and (Van Hout et al., 2003)..... 148

Table 8.3. Fitting parameters and determination coefficient 151

Table 8.4. Experimental conditions of the present experiments and Cheng and Burkhardt (2003), Zheng and Che (2006) and (Van Hout et al., 2003)..... 152

NOMENCLATURE

Abbreviations

BSD	Bubble Size Distribution
DFT	Discrete Fourier Transform
ECT	Electrical Capacitance Tomography
LBP	Linear Back Projection
PDF	Probability Density Function
PSD	Power Spectral Density
SVD	Singular Value Decomposition
VF	Void Fraction
WMS	Wire Mesh Sensor

Latin upper case

A	area, fitting coefficient	$\dot{M}$	mass flow
B	fitting coefficient	N	number
C	capacitance, fitting coefficient	R	cross-correlation
Co	distribution coefficient	R^2	determination coefficient
D	diameter	Re	Reynolds number
E	fitting coefficient	S	normalized sensitivity
F	fitting coefficient	St	Strouhal number
Fr	Froude number	T	period
J	sensitivity	U	superficial velocity
K	gain	V	velocity, voltage, volume
L	equivalent length	X	volume fraction
M	capacitance measurements		

Latin lower case

a	fitting coefficient, weight coefficient	p	pitch, pressure
b	radial weigh coefficient	t	time
d	distance	x	distance in x-axis, mean
f	frequency		void fraction
g	gravity, normalized permittivity	y	distance in y-axis
l	length	z	distance in z-axis

Greek

$\forall$	volume	ν	viscosity
Δ	increment	ρ	density
α	angle of inclination, void fraction	σ	surface tension, standard deviation
ε	void fraction, permittivity	τ	delay
λ	normalized capacitance	χ	Lockhart-Marinelli parameter

Superscript

b	bubble (structure)	m	mixture, radial position
c	critical, cell	p	plane, projected
d	drift	s	superficial, section
e	equivalent	t	time, total
g	gas	x	position x
l	liquid, length		

Subscript

h	horizontal	v	vertical

CHAPTER 1.

INTRODUCTION

1.1 Introduction

Driving fluids into pipes has been a very efficient way for their transportation. This approach is widely used for water supply, sanitation or irrigation purposes. Pipes are also preferred in many other industrial processes, instead of storing fluids in tanks and transport them using vehicles, including; cooling water systems, gas and steam supplies, drainage, oil and gas pipelines, penstock for hydroelectric installations, etc.

The movement of a single fluid flowing in a pipe is a well understood problem. It is possible to predict with good accuracy the velocity and the pressure of the fluid at any point of the pipe or any point of a complex system of pipes. Moreover, it is also possible to know the stress supported by the material of the pipe and the efforts applied to the joints. But the problem is not completely solved whenever there are two or more fluids (or fluidized solids), that are immiscible, flowing together in the same pipe. That is the case of oil and water, water and air or water and sand mixtures, in general any mixture of immiscible materials allowing different phases to be distinguished in the flow. These flow conditions are known as multiphase flow.

One aspect of multiphase flows, but probably the most studied of all, is the gas-liquid two-phase flow. Its significance can be realised in its complexity and the wide applications in the industry nowadays. It can being encountered in boilers, condensers, oil wells, nuclear reactors, and many processes in the chemical and food industries among others. Furthermore, the complexity of the gas-liquid two-phase flow lies in the interface between the phases. One of the simplest cases of gas-liquid two-phase flow

consists of small gas bubbles dispersed in a continuous liquid phase, such as in sparkling water. That type of flow is often encountered at low gas flow rates. A higher gas flow rates, the gas-liquid interface encloses irregular, chaotic and unstable gas structures that are in a continuous movement. Despite the complexity of these different interphases, sometimes the two-phase flows reflect similarities that can be arranged to flow regimes or flow patterns. The four major types of flow regimes or patterns are bubbly, slug, churn, and annular flows.

Slug flow, and sometimes bubbly and churn flow as well, can be considered intermittent flows. They present a pattern in which, when observed from a fixed point along the pipe, a gas dominated structure followed by a liquid dominated structure is seen to be repeated with a characteristic mean frequency.

Four main characteristics define an intermittent flow: velocity, frequency and lengths of the gas and liquid dominated structures. And these three characteristics are sources of a diversity of problems in the industry. For example, liquid dominated structures moving at a certain velocity accumulate a momentum higher than the average momentum of the flow, causing this momentum to be discharged in bends, pipe reductions or in-line equipment. Additionally, the frequency of the gas and liquid structures produces vibrations in the pipe that can generate noise, resonance, displacement of the pipe, fatigue of the materials, or loosening of the bolts. Finally, when the length of the liquid or gas structure is multiplied by the pertinent phase fraction in them, can result in a much bigger volume of one of the phases. Therefore, in line equipment, such as separators, must then be designed to be able to receive higher amounts of liquid or gas than the average flow.

The periodic structures in gas-liquid two-phase flow appear at certain conditions, depending on the amount of gas and liquid flowing in the pipe. These periodic structures

also depend on the physical properties of the fluids, such as: density, viscosity, and the surface tension in between both phases. For example, the intermittencies are more likely to appear in viscous liquids. Apart from the physical properties of the flow, geometrical parameters of the pipe (diameter, length, inclination, etc.) also have a direct influence on the development of intermittent flows. Lastly, it worth mentioning that in narrow pipes, the intermittency is better defined compared to the case in large diameter pipes due to the effect of the wall.

Within this context, the aim of this thesis is to study the influence of geometrical parameters, such as the diameter of the pipe, its angle of inclination and the type of gas injection in the development of gas-liquid intermittent flows.

1.2 Objectives

1. To generate intermittent flows at different gas and liquid rates in two large diameter pipes with different angles of pipe inclination.
2. To acquire void fraction time series of intermittent flow generated using Wire Mesh Sensor (WMS) and Electrical Capacitance Tomography (ECT).
3. To develop methods to identify, observe and measure the gas and liquid structures from the data of the WMS and ECT sensors.
4. To study the influence of the diameter of the pipe on:
    - Velocities of the gas structures
    - Frequencies of the gas structures
5. To study the influence of the angle of inclination of the pipe on:
    - Velocities of the gas structures
    - Frequencies of the gas structures

6. To propose a model to predict the velocity of the gas structures, depending on the gas and liquid flow rates, diameter and inclination of the pipe.
7. To propose a model to predict the frequency of the gas structures, depending on the gas and liquid flow rates, diameter and inclination of the pipe.
8. To study the influence of the gas injection in the development of intermittent flows.

1.3 Methodology

All the methodology followed in this thesis is generally categorised into three main parts: experimental, data processing, and modelling; a summary of them is provided below.

1.3.1 Experimental

The fluids employed in all cases were air as the gas phase and silicone oil as the liquid phase. The rationale for choosing air for the gas phase was that it has a similar density to other common gases such as water vapour, N_2 or natural gas, in addition to being much easier to work with and safer too. Moreover, the choice of air will allow the comparison of the results with previously published data where air is employed, which is the case for the vast majority of investigations. Silicone oil was chosen for the liquid phase because it is a non-conductive fluid, which is an essential requirement for the electrical capacitance tomography (ECT) sensing. Additionally, it has a viscosity and a surface tension similar to the viscosity of the petroleum oil whose two-phase flow development poses a great interest for the industry.

The experiments were performed in two different rigs, which will be described in more detail in Chapter 3. Both are a close two-phase flow loop with the test pipe in vertical position with the fluids moving upwards. The main difference between the rigs is the diameter of the test pipe; namely 67 and 127 mm for the small rig and the big rig

respectively. These diameters were chosen based on relevancy to industrial requirements, especially the oil industry where there is a constant demand to increase the pipe diameter. In contrast to the majority of the previous studies which were carried out in pipes with diameters ranging between 1 to 2 inches, the diameters of 67 and 127 millimetres are considered intermediate diameters in the multi-phase flow perspective. The first set of experiments were performed using these two different diameter rigs to examine the influence of the diameter of the pipe on intermittent flows.

The second experimental campaign was done in the 67 mm rig. The test pipe of this rig can be rotated and the inclination angle of the pipe can be changed to different positions. Seven inclination angles from horizontal to vertical in steps of 15° were selected to study the influence of the angle of inclination on the development of intermittent flows.

Finally, the last set of experiments were done in the 67 mm rig in the vertical position while changing the gas and liquid mixer at the base of the test pipe. This was performed to investigate the influence of the gas injection on the development of intermittent flows.

The measurement techniques implemented in this study were Electrical Capacitance Tomography (ECT) and the Wire Mesh Sensor (WMS). ECT is a non-intrusive technique that allows for calculation of the velocity of the gas and liquid structures using cross-correlation techniques. On the other side, WMS is currently one of the most advanced measurement techniques used in multiphase flows research, providing high temporal and spatial resolution information of the flow development. However, it is highly intrusive. These two techniques complement each other, allowing a deeper and more thorough understanding of the flow when used combined.

1.3.2 Processing of the data

The data obtained in the experiments from the ECT and WMS sensors were processed employing Matlab codes. As most of the software packages included with the sensors were not open source, it was decided to create in-house codes instead. This approach was preferred because having full control of the codes permits a better understanding of the limitations of data processing in addition to allowing further more detailed analysis. However, some of the codes and algorithms used here were adopted from the manuals provided with the sensors and the scientific/technical publications produced by the sensors' developers (Prasser et al., 1998, Prasser et al., 2001).

The description of the codes and data processing are explained in detail in Chapter 4.

1.3.3 Analysis and modelling

The last part of the methodology was the analysis of the collected data from the experiments and the development of physical models that can explain and predict the experimental observations. This is shown at the end of each of the results chapters and compiled also in the last chapter of this thesis.

1.4 Structure of the thesis

The thesis is divided into the following chapters:

Chapter 1. Introduction.

This chapter provides a first overview of the contents and justification of the thesis. It explains the importance of the intermittent two-phase flows for the industry, the problems associated with them, and the importance of having a good understanding to prevent these problems in order to optimise the design of the industrial facilities. Additionally, it summarises and justifies the methodology used in the work.

Chapter 2. Literature review.

In this chapter, a review of the related literature is given. The gas-liquid intermittent two-phase flows are contextualised in the two-phase flow regimes. The mechanisms and conditions that activate the transition to intermittent flow are detailed. The work of other authors is explained, emphasizing the findings on the velocity and frequency of the periodic structures in intermittent flows.

Chapter 3. Experimental arrangements

The fluids employed are described in this chapter, including their physical properties. Chapter 3 also includes a description of the two-phase flow facilities in which the experiments were conducted and the measurement techniques employed.

Chapter 4. Processing of the data

In this chapter, it is explained how the raw data from the ECT and WMS sensors was processed to obtain information about the two-phase flow. It includes temporal void fraction, mean void fraction, void fraction profiles, structures velocity, frequency, length, etc.

Chapter 5. The influence of the angle of inclination in intermittent flows

In the fifth chapter, the data obtained at different angles of inclination of the pipe are presented. At the end of the chapter, the results are discussed and compared with predictions previously reported in the literature. Two new correlations to predict the velocity and the frequency of the periodic structures depending on the angle of inclination are also proposed.

Chapter 6. The influence of the diameter of the pipe in intermittent flows.

The results obtained at different diameters of the pipe are presented in this chapter, as well as discussed and compared with predictions suggested in the literature. Two new

correlations to predict the velocity and the frequency of the periodic structures depending on the diameter of the pipe are proposed.

Chapter 7. The influence of the gas entrance in intermittent flows.

Chapter 7 is the final results chapter that shows the results obtained using three different gas and liquid mixers. The results obtained are discussed and compared, for the purpose of elucidating the influence of the gas injection method on the development of intermittent two-phase flows.

Chapter 8. General discussions and conclusions

The correlations developed for the velocity and frequency in Chapters 5 and 6 are unified into two correlations, one for the velocity and the other for the frequency. The correlations take into consideration both the angle of inclination and the diameter of the pipe. These correlations are also compared against data already published in the literature. The main conclusions of the thesis and some ideas for future work are outlined at the end of this chapter.

CHAPTER 2.

LITERATURE REVIEW

2.1 Introduction

Co-flow of two distinct phases in a conduit is considered multiphase flow. The fluids can be the same material with two states existing side by side (water and steam) or different materials (water and air) but separated by an interface. The phases can combine in various forms: gas-liquid (air and water), liquid-liquid (oil and water), solid-liquid (sand and water), etc. There can be more than two phases flowing together, for example, a hydrocarbon well where natural gas, petroleum, water and sand can be found. The research presented in this thesis is focused on gas-liquid two-phase flow.

2.1.1 Gas-liquid two-phase flow

One of the widely used variables to describe gas-liquid two-phase flow is the void fraction. Typically, it is the area occupied by the gas at a given cross-section as the ratio to the total cross-sectional area. It is calculated as:

$$\varepsilon_g = \frac{\mathrm{A}_g}{A_g + A_l} \qquad [2.1]$$

where A_g is the area of the cross-section occupied with gas and A_l is the part occupied with liquid. $A_g + A_l$ is equal to the area of the pipe, $A_s = D^2\,\pi/4$

Alternatively, the liquid hold up is the opposite of the void fraction, expressed as

$$\varepsilon_l = \frac{\mathrm{A}_l}{A_g + A_l} = 1 - \varepsilon_g \qquad [2.2]$$

In multiphase flows, the amount of each phase flowing through the pipe is normally specified by superficial velocities. It is the mean velocity that a single phase would have if it occupies the whole cross-section of the pipe alone without the presence of the other phase. For gas and liquid phase they are expressed as:

$$U_{gs} = \frac{\dot{\mathrm{M}}_g}{\rho_g A_s} \quad [2.3]$$

$$U_{ls} = \frac{\dot{\mathrm{M}}_l}{\rho_l A_s} \quad [2.4]$$

where $\dot{\mathrm{M}}_g$ and $\dot{\mathrm{M}}_l$ are the gas and liquid mass flows and ρ_g and ρ_l are the gas and liquid densities respectively.

In reality, if two fluids are flowing together, then the velocities of the phases are different to the superficial velocities because they do not occupy the whole area of the pipe. The mean velocity of each phase can be calculated by dividing the superficial velocity by the void fraction (or liquid hold up):

$$U_g = \frac{U_{gs}}{\varepsilon_g} \quad [2.5]$$

$$U_l = \frac{U_{ls}}{1 - \varepsilon_g} \quad [2.6]$$

where U_g and U_l are the gas and liquid mean velocities respectively.

2.2 Gas-liquid flow regimes

As noted above, in multiphase flow, the different phases are separated by a deformable interface. This interface can adopt very complicated forms and it is in a continuous rapid dynamic movement. However, even if it is not possible at the moment to precisely determine the shape of the interface, they show similarities across pipe geometries

allowing us to classify multiphase flow into broad bands called flow regimes (or flow patterns).

Many classifications of the flow regimes have been proposed in vertical pipes (Wallis, 1969, Hewitt and Roberts, 1969, Taitel et al., 1980) and in horizontal pipes (Hubbard and Dukler, 1966, Wallis, 1969, Taitel and Dukler, 1976); but there is a wide agreement in the general patterns. These patterns are bubbly, slug, churn and annular flow in vertical pipes and dispersed bubble, slug, stratified and annular in horizontal pipes. They are illustrated in Figure 2.1 (Bratland, 2010)

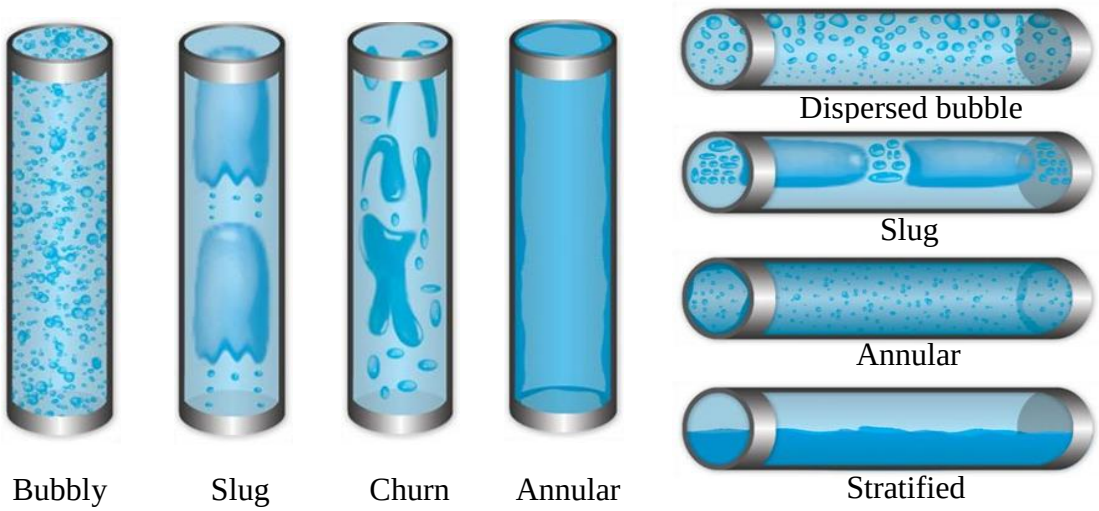


Figure 2.1 Main flow regimes in vertical and horizontal pipes (Bratland, 2010).

2.2.1 Flow patterns in vertical pipes

The main four flow patterns in vertical pipes: bubbly, slug, churn and annular flow; are described below.

Bubbly flow: can be homogeneous or heterogeneous. It is homogeneous when there are homogeneously dispersed small bubbles in the liquid phase and it is heterogeneous when some of the small bubbles coalesce forming bigger bubbles whereby both small

and big bubbles coexist. Heterogeneous bubbly flow is sometimes termed cap bubble flow.

Slug: as the gas velocity increases bigger bubbles known as Taylor bubbles appear in the flow. These bubbles occupy more than two thirds of the pipe diameter. Sometimes the bubbles could occupy the totality of the pipe diameter, constrained by the pipe walls. This constriction shapes the bubbles to an elongated form whose length can be several times the pipe diameter. The Taylor bubbles are separated by liquid slugs which contain small dispersed bubbles. Also, the Taylor bubbles are surrounded by the liquid film which may flow downward.

Churn: further increase of gas flow would make the slug flow very irregular. The liquid film around Taylor bubbles would start to oscillate upwards and downwards. The liquid slugs in between the bubbles become short and very aerated.

Annular: it happens at higher gas velocities where big bubbles connect to form a continuous gas core. The liquid film in contact with the wall flows always upward. There are waves on the liquid film that can break and release small droplets which become entrained by the upwardly flowing gas core.

2.2.2 Flow patterns in horizontal pipes

Some of the experiments presented in this work involve flows in horizontal pipes. Therefore, a brief introduction to the flow regimes in horizontal pipes is given here. The main four flow patterns in horizontal pipes are dispersed bubble, stratified, slug and annular flow. They are described below.

Dispersed bubble: gas bubbles disperse in the liquid phase. Normally, there is a higher concentration of bubbles at the upper half part of the pipe due to buoyancy. At higher

liquid velocities, the bubbles tend to disperse more uniformly because the turbulence and shear forces agitate and distribute the bubbles across the pipe cross-section.

Stratified: it takes place at low liquid flow where the two phases are separated. The liquid rests on the lower part of the pipe and the gas on top and they travel along the pipe without mixing with each other. At relatively higher gas flowrates the liquid-gas interface phase becomes wavy, then the regime is identified as wavy stratified.

Slug: with increasing the gas flow, waves start to appear at the interface of the stratified flow. These waves can touch the top of the pipe and bridge the entire pipe cross-section, forming liquid slugs. The slug flow consists of elongated bubbles travelling on the upper part of the pipe but occupying most of the pipe cross-section followed by liquid slugs that may contain dispersed bubbles in them.

Annular: at even higher gas flowrates the liquid is forced away to the walls where the centre of the pipe becomes occupied by a gas core with entrained droplets. The liquid forms a film around the pipe wall that is thicker on the lower part compared to the upper part due to the act of gravity. The film contains ripples and some liquid droplets can be entrained from the film to the gas core.

2.3 Flow pattern transitions and maps

The aforementioned flow regimes and their transitions from one to another can be determined by direct or indirect observation of the flow and then apply personal judgments to classify them. Some authors have attempted to define the mechanisms that produce the changes of flow regimes and the flow conditions necessary to trigger these mechanisms (Taitel et al., 1980, Weisman and Kang, 1981, Mishima and Ishii, 1984). Some of these analysis are summarized in the following section.

2.3.1 Bubbly to slug flow transition

Taitel et al. (1980) proposed that the transition from bubbly to slug flow in vertical pipes occurs when the void fraction is equal to 0.25. Based on this assumption and applying the equation of Harmathy (1960) to calculate the bubbles' rise velocity, they suggested the following expression for the transition from bubbly to slug flow.

$$U_{ls} = 3U_{gs} - 1.148\left(\frac{g\sigma(\rho_l - \rho_g)}{\rho_l^2}\right)^{0.25} \quad [2.7]$$

Mishima and Ishii (1984) posed a similar proposal to Taitel et al. (1980). But they considered that the transition occurs when the void fraction is equal to 0.30. They supported this value by geometrical calculations considering a tetrahedral packing of the bubbles. Additionally, they used a drift flux model to calculate the velocity of the bubbles. As a result, they obtained the following equation to calculate the transition from bubbly to slug flow:

$$U_{ls} = \left(\frac{3.33}{C_0} - 1\right)U_{gs} - \frac{0.76}{C_0}\left(\frac{g\sigma(\rho_l - \rho_g}{\rho_l^2}\right)^{0.25} \quad [2.8]$$

where C_0 is given by,

$$C_0 = 1.2 - 0.2\sqrt{\rho_g/\rho_l} \quad \text{for round tubes} \quad [2.9]$$

$$C_0 = 1.35 - 0.35\sqrt{\rho_g/\rho_l} \quad \text{for rectangular tubes} \quad [2.10]$$

Weisman and Kang (1981) proposed a correlation to find the transition from bubble to slug flow at any inclination angle of the pipe, from horizontal to vertical. They observed that the transition was a function of the Froude number of the gas phase and the Froude number of the mixture. They also observed that the relationship depends on the angle of inclination of the pipe. They proposed the expression below:

$$\frac{U_{gs}}{\sqrt{g\,D}} = 0.45\left(\frac{U_{gs}+U_{ls}}{\sqrt{g\,D}}\right)^{0.78}(1-0.65\cos\alpha) \qquad [2.11]$$

2.3.2 Slug to churn flow transition

Taitel et al. (1980) considered churn flow a non-developed slug flow. They stated that close to the gas entrance the gas bubbles and the liquid slugs in between them are too short. The slugs are not consistent and they break up causing the liquid of the slug to drain and be collected by the following slug. At the same time, the bubbles coalesce forming longer bubbles. This process is repeated over a certain length of the pipe's length until the liquid slugs are long enough to be consistent and the elongated bubbles stop coalescing. They developed a model to calculate the velocity of the Taylor bubbles as a function of the slug length and the gas and liquid superficial velocities. Then they calculated the distance from the mixer (l_i) at which the Taylor bubbles would stop coalescing. As a result, they (Taitel et al. (1980)) proposed an expression to calculate the transition from slug to churn flow taking into account the distance from the inlet.

$$\frac{l_i}{D} = 40.6\left(\frac{U_{gs}+U_{ls}}{\sqrt{g\,D}}+0.22\right) \qquad [2.12]$$

where l_i is the distance from the gas and liquid inlet to the point of the pipe where the flow is observed.

Mishima and Ishii (1984) suggested that the transition happens when the mean void fraction of the entire region (the slug unit that consists of the slug and the bubbles) is equal to the mean void fraction of the bubbles in the liquid slug. They calculated the total mean void fraction, ε_t, using a drift flux model and the void fraction of the bubbles in the liquid slug , ε_b, developing their own model. Equations for ε_t and ε_b are:

$$\varepsilon_t = \frac{U_{gs}}{C_0 U_{ms} + 0.35\sqrt{(\rho_l - \rho_g)gD/\rho_l}} \quad [2.13]$$

$$\varepsilon_b = 1 - 0.813\left(\frac{(C_0 - 1)U_{ms} + 0.35\sqrt{(\rho_l - \rho_g)gD/\rho_l}}{U_{gs} + 0.75\sqrt{(\rho_l - \rho_g)gD/\rho_l}\left((\rho_l - \rho_g)gD^3/\rho_l \nu_l^2\right)^{\frac{1}{18}}}\right)^{0.75} \quad [2.14]$$

Another mechanism to define the transition from the slug to churn flow is the flooding of the liquid film around the Taylor bubble (Nicklin et al., 1962). It happens when the liquid falling around the Taylor bubble starts moving upwards concurrently with the gas stream. Wallis (1969) proposed a correlation to predict the flooding phenomenon in vertical gas-liquid flows as:

$$\left[U_{gs}\left(\frac{\rho_g}{(\rho_l - \rho_g)gD}\right)^{\frac{1}{2}}\right]^{\frac{1}{2}} + \left[U_{ls}\left(\frac{\rho_l}{(\rho_l - \rho_g)gD}\right)^{\frac{1}{2}}\right]^{\frac{1}{2}} = 1 \quad [2.15]$$

Weisman and Kang (1981) studied the regimes transitions in gas-liquid flows inclined pipes, but churn flow only exists in vertical pipes. They did not distinguish between slug and churn flows, however called them both intermittent flows in their flow pattern map.

2.3.3 Churn to annular flow transition

Taitel et al. (1980) proposed that annular flow can only exist if the gas velocity in the core of the annular flow is high enough to lift entrained droplets from the liquid film. They formulated a force balance between the weight of the droplets and the drag with the air to conclude that they would equate if the following expression is satisfied:

$$U_{gs} = 3.1 \frac{\left[\left(\rho_l - \rho_g\right) g \sigma\right]^{1/4}}{{\rho_g}^{1/2}} \qquad [2.16]$$

where σ is the surface tension between the gas and liquid phases.

Mishima and Ishii (1984) developed models for the transition from churn to annular flow proposing two different mechanisms. The first is the flow reversal of the liquid film along the wall surrounding big bubbles. The second is the destruction of liquid slugs or big waves generated by entrainment or deformation. They proposed the expressions [2.17] and [2.18] respectively for the two possible transition mechanisms.

$$U_{gs} = \sqrt{\frac{\left(\rho_l - \rho_g\right) g D}{\rho_g}} \left(\varepsilon_b - 0.11\right) \qquad [2.17]$$

$$U_{gs} = \left[\frac{g \sigma \left(\rho_l - \rho_g\right)}{{\rho_g}^2}\right]^{1/4} \left[\mu_l \Big/ \left(\sigma \rho_l \sqrt{\frac{\sigma}{g\left(\rho_l - \rho_g\right)}}\right)^{1/2}\right]^{-0.2} \qquad [2.18]$$

where ε_b is the void fraction in the big bubble calculated using equation [2.14]

Weisman and Kang (1981) affirmed that the transition from churn to annular flow is unaffected by the angle of inclination. And they introduced a correlation for this transition by fitting the results of the experiments of Simpson et al. (1981) for different liquids and pipe diameters. The resulting correlation, which is independent of the angle of inclination, is:

$$1.9\left(U_{gs}/U_{ls}\right)^{1/8} = \left[\frac{U_{gs} \rho_g}{\left[g \sigma \left(\rho_l - \rho_g\right)\right]^{1/4}}\right]^{0.2} \left[\frac{U_{gs}^2}{gD}\right]^{0.18} \qquad [2.19]$$

2.3.4 Transition to dispersed flow

Taitel et al. (1980) explained that at high liquid velocities the turbulence forces break the gas phase and disperse it into small bubbles. Although, they added that there is a maximum void fraction, ε_{max} equals to 0.52, above which the bubble flow cannot exist regardless of how much turbulence energy the flow has. To predict velocities at which these two conditions are satisfied they developed the expressions below.

$$U_{ls} + U_{gs} = 4.0 \frac{D^{0.429}(\sigma/\rho_l)^{0.089}}{\nu_l^{0.072}} \left[\frac{g(\rho_l - \rho_g)}{\rho_l}\right]^{0.446} \quad [2.20]$$

$$0.52 = \frac{U_{gs}}{U_{ls} + U_{gs}} \quad [2.21]$$

Weisman and Kang (1981) presented an expression to calculate the transition to the dispersed flow that was independent of the angle of inclination of the pipe. They performed a force balance between the turbulent and the buoyancy forces and they corrected it to include the surface tension and pipe diameter effects. The resultant expression is as follows:

$$\left[\frac{(dp/dx)_{ls}}{(\rho_l - \rho_g)g}\right]^{1/2} \left[\frac{\sigma}{(\rho_l - \rho_g)gD^2}\right]^{-1/4} = 9.7 \quad [2.22]$$

2.3.5 Flow pattern maps

Flow pattern maps are graphs to show the transitions between flow regimes. Normally the gas superficial velocity is plotted on the abscissa and the liquid superficial velocity on the ordinate. But, sometimes the quantities of the axes are a combination of gas and liquid superficial velocities together with the pipe diameter or the physical properties of the fluids. This is carried out to generalize the flow pattern map to different geometries and fluids.

Lines are drawn on the flow pattern maps to mark different flow regimes areas. Points inside a particular area often correspond to the flow conditions that produce the same flow regime. The lines defining the areas are the narrow regions that indicate the transitions between flow regimes. These lines, representing the transitions, can be drawn after observation of the flow. The transitions can also be defined using mathematical expressions that represent the flow conditions necessary to trigger the mechanisms that produce the change of flow regime. Some mathematical expressions suggested by different authors were presented in the previous section. They are plotted together in Figure 2.2 forming the flow pattern maps each corresponding to different researchers as per the legend.

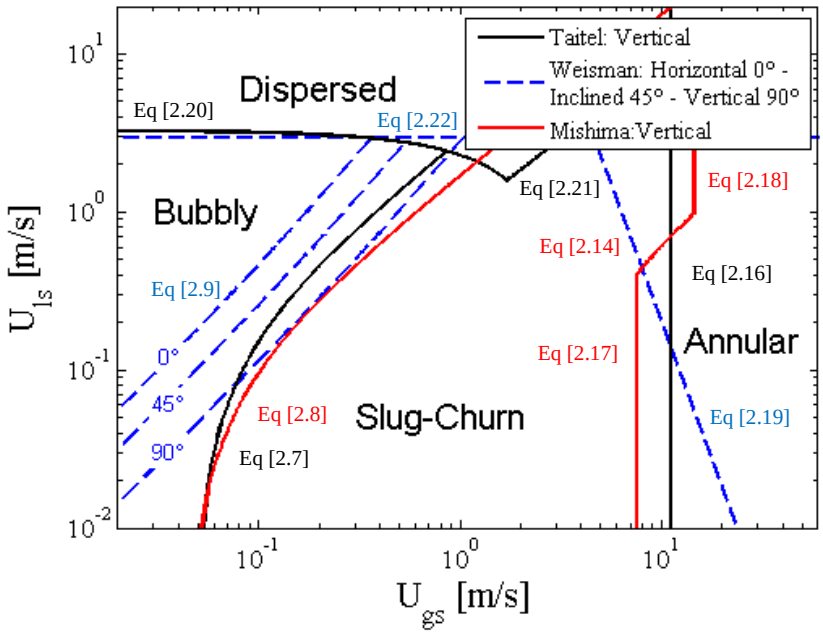


Figure 2.2 Taitel et al. (1980), Weisman and Kang (1981) and Mishima and Ishii (1984) flow pattern maps

To draw the flow pattern maps in Figure 2.2, a pipe diameter of 67 mm was selected and the fluids properties employed were those of silicone oil for the liquid phase and air at atmospheric pressure for the gas phase.

It can be seen that the flow pattern maps of the different authors (Taitel et al., 1980, Weisman and Kang, 1981, Mishima and Ishii, 1984), which are developed from different models and assumptions, show huge similarities. For example, in the case of the vertical flow, the regions of bubble, slug-churn and annular show a good agreement for the different authors' flow maps.

2.4 Intermittent flows

Intermittent flows occupy a significant part of two-phase flow patterns: cap bubble, slug and churn (Weisman and Kang, 1981). They present a pattern in which, when observed from a fixed point along the pipe, a gas dominated structure followed by a liquid dominated structure is seen to be repeated with a characteristic mean frequency.

Slug flow is the flow pattern most easily recognizable as an intermittent flow. It is found in all inclination angles of a pipe with two-phase flows. It mainly consists of big gas bubbles followed by liquid slugs with some particularities depending on the inclination angle, the pipe diameter, and the gas and liquid superficial velocities.

In vertical small pipe diameters, the slug flow is characterized by large bullet shaped bubbles occupying almost the totality of the pipe cross-section and having a length of several pipe diameters. These bubbles are called Taylor bubbles since they were studied and described by Davies and Taylor (1950). Following the Taylor bubble, there is a liquid slug consisting of small bubbles dispersed in a continuous liquid phase. In these two structures, one is dominated by gas (Taylor bubble) and the other is by liquid (liquid slug) follow one after the other causing the intermittency in the slug flow. By increasing the pipe diameter, the Taylor bubbles lose the smooth bullet shape. The turbulence created by the wake of the leading bubble does not dissipate before reaching the tip of the following bubble in large tubes causing distortion of the bubble. These disturbances

also affect the liquid-gas interface, in the case of big bubbles the surface tension is not strong enough to hold the round shape of the bubble. The liquid film surrounding the bubble becomes unstable forming waves that create some liquid entrainment into the bubble. Accordingly, the bubbles become irregular and asymmetric. Apart of that, many small bubbles get entrained from the Taylor bubble into the liquid slug due to the presence of waves on the film interface (Mattar and Gregory, 1974). These effects increase with the pipe diameter to the point where the flow presents similarities with the churn flow. In other words, the slugs become very aerated and the Taylor bubbles appear to be connected. Additionally, the liquid film surrounding the Taylor bubble comes to be wavy and irregular with liquid entrained in the bubble. However, irrespective of whether this flow pattern can be considered slug or churn, there are still two distinct gas/liquid dominated structures and the flow can be considered intermittent (Weisman and Kang, 1981).

In horizontal and inclined pipes the gas bubble is not centred in the pipe but rather displaced to the wall in opposite direction to gravity. Slug flow (sometimes referred to as plug flow) can be observed in any pipe diameter at certain gas and liquid superficial velocities. Churn flow does not appear in horizontal and inclined pipes unless the inclination is very close to the vertical position, (Weisman and Kang, 1981).

Another flow pattern that can behave as intermittent flow is cap bubble flow. Close to transition from bubble to slug flow some big bubbles are formed. These bubbles are not Taylor bubbles since they do not have a bullet shape or their length is not several times that of the pipe diameter. However, they can be several times bigger than the other smaller bubbles dispersed in the liquid. This allows them to be identified as dominant gas structures.

To summarise, it can be said that intermittent flows cover different flow regimes and can be encountered at any angle of inclination either in small or large diameter pipes.

2.4.1 Characterization of intermittent flow

The characteristics that define intermittent flows are the length, the velocity, the frequency and the void fraction of the gas and liquid structures. The length and the void fraction of the liquid structures are different to those of the gas structures. On the other hand, it is assumed, once the flow is developed, that the velocity and frequency of the gas and liquid structures are the same. In the next section, some models proposed by different investigators to predict the velocity and the frequency of the periodic structures in intermittent flows will be detailed.

2.4.1.1 Velocity of the periodic structures in intermittent flows

The velocity of the periodic structures can be deducted by resolving one of the two-phase flow models: the two-fluid model or the drift-flux model. The two-fluid model considers the two phases separately; hence the model resolves the conservation equation of mass, momentum and energy of each phase. The two-fluids model requires specifying terms for the interactions between the two phases adding considerable difficulties to the model (Ishii, 1975). On the other hand, the drift-flux model considers the flow as a mixture and the conservation equations are resolved for that mixture. The model hides some information compared with the two-fluids model, but its simplicity makes it very appropriate for engineering applications (Ishii and Hibiki, 2010).

In the drift-flux model, the velocity of the gas structures is the superposition of the velocity of the mixture at the centre of the pipe and the drift velocity of the gas. The drift velocity is defined as the velocity of the gas structures with respect to the velocity of the liquid at the centre of the pipe. Nicklin et al. (1962) applied the drift-flux model

to Taylor bubbles and they affirmed that the velocity of the bubble is the superposition of the drift velocity of the bubble in stagnant liquid V_d, and the mixture velocity U_{ms} (sum of the gas and liquid superficial velocities $U_{gs} + U_{ls}$), multiplied by a coefficient C_0.

$$V_b = C_0 U_{ms} + V_d \qquad [2.23]$$

The C_0 coefficient value is the maximum flow velocity (normally taken at the middle of the pipe) divided by the average velocity. It is 2 in laminar flow and decreases to lower values with increasing the Reynolds number. Different authors considered that C_0 is a constant value around 1.2 for turbulent flow. Others like Frechou (1986) expressed C_0 as a function of the Reynolds number. Bendiksen (1984) proposed an empirical correlation as a function of the angle of inclination of the pipe. Both correlations are shown in the expressions [2.24] and [2.25].

$$C_0(Re) = \frac{2.27}{1 + (Re/Re_c)^2} + \frac{1}{1 + (Re_c/Re)^2} \qquad [2.24]$$

$$C_0(\alpha) = C(0°) + [C(90°) - C(0°)] \sin^2 \alpha \qquad [2.25]$$

where Re_c is the Reynolds on the transition from laminar to turbulent (proposed to be 4000), $C(0°)$ =1 and $C(90°)$=1.2.

Dumitrescu (1943) and Davies and Taylor (1950) predicted that the drift velocity is equal to $Fr\sqrt{gD}$ where g is gravity acceleration and D the pipe diameter. The values of Froude Number Fr that Dumitrescu (1943) and Davies and Taylor (1950) proposed for vertical flows were 0.351 and 0.328 respectively. For horizontal flows, Benjamin (1968) applied the same criteria and evaluated Fr to be equal to 0.54. Considering that, vertical and horizontal drift velocity can be calculated as:

$$V_d^v = 1.2U_{ms} + 0.35\sqrt{gD} \quad [2.26]$$

$$V_d^h = 1.2U_{ms} + 0.54\sqrt{gD} \quad [2.27]$$

A maximum drift velocity was observed for inclined pipes primarily by Zukoski (1966) when the inclination angles α, falls in the range of $40° < \alpha < 60°$. He reported as well that the drift velocity has little dependence on the viscosity but high dependence on the surface tension parameter, $\Sigma = 4\sigma/\Delta p g D^2$. Taking Zukoski values for V_d^h and V_d^v into consideration, Bendiksen (1984) proposed the following correlation for the drift velocity in inclined pipes.

$$V_d = V_d^h \cos\alpha + V_d^v \sin\alpha \quad [2.28]$$

Hasan and Kabir (1988) gave a similar expression to calculate the drift velocity in inclined pipes as a function of the angle of inclination α. The main difference is that they considered the drift velocity in horizontal pipes to be equal to 0. The expression by Hasan and Kabir (1988) can be written as:

$$V_d = V_d^v \sqrt{\sin\alpha}\,(1 + \cos\alpha)^{1.2} \quad [2.29]$$

2.4.1.2 Frequency of the periodic structures in intermittent flows

Frequency in intermittent flows is defined as the number of slugs passing by a fixed point per unit of time. But sometimes there is no a clear method to identify and count the slugs. One approach is to count it manually from direct or indirect observation of the flow (Gregory and Scott, 1969, Van Hout et al., 2003). Another method is to distinguish the slugs from the gas bubbles applying a threshold in the void fraction time series (Fossa et al., 2003, Waltrich et al., 2013). And the last one is by considering the dominant frequency in the probability density function (PDF) of the void fraction time series (Hernandez-Perez 2008, Abdulkadir et al., 2016).

Frequency measurements have been correlated with the gas and liquid superficial velocities, the pipe diameter and physical properties of the fluids. Two families of correlations appear in the literature. One based on the equation of Gregory and Scott (1969) and the other is based on correlating the Strouhal number with the liquid volume fraction or the Lockhart-Martinelli parameter.

Gregory and Scott (1969) observed that, in horizontal pipes, the frequency of the gas structures is dependent on a modified form of the Froude number. They also added that the frequency reaches its minimum value when the slug velocity reaches 6 m/s. From these observations and the data of Hubbard (1965) they proposed the following correlation for the frequency in horizontal flows:

$$f^h = 0.0226\left[\frac{U_{ls}}{gD}\left(\frac{19.75}{U_{ms}} + U_{ms}\right)\right]^{1.2} \qquad [2.30]$$

Following the procedure of Gregory and Scott (1969), similar correlations were proposed based on new experimental data under different conditions (Greskovich and Shrier, 1972, Heywood and Richardson, 1979, Zabaras, 1999, Hernandez-Perez et al., 2010)

Zabaras (1999) correlation is applicable for slightly inclined pipes based on experiments from 0° to 11°. This correlation corrects Gregory and Scott equation [2.30] by multiplying it by an angle dependent term.

$$f = 0.0226\left[\frac{U_{ls}}{gD}\left(\frac{212.6}{U_{ms}} + U_{ms}\right)\right]^{1.2}(0.836 + 2.75\sin^{0.25}\alpha) \qquad [2.31]$$

Hernandez-Perez et al. (2010) adjusted their data in 32 and 67 mm pipes to Gregory and Scott (1969)'s correlation [2.30] modifying the empirical parameters and obtaining the following formula:

$$f^v = 0.8428\left[\frac{U_{ls}}{gD}\left(\frac{19.75}{U_{ms}} + U_{ms}\right)\right]^{0.25} \quad [2.32]$$

They also suggested that the frequency in inclined pipes is a combination of the vertical and horizontal frequencies:

$$f = f^h \cos\alpha + f^v \sin\alpha \quad [2.33]$$

where f^v is the frequency in horizontal pipes calculated using equation [2.32] and f^h is the frequency in vertical pipes calculated using Gregory and Scott's correlation [2.30]

The next family of equations correlates the frequency, expressed as the dimensionless Strouhal number St, with the Lockhart-Martinelli parameter χ or the liquid volume fraction X_l. These three numbers are expressed as:

$$St = \frac{f\ D}{U} \quad [2.34]$$

$$\chi = \sqrt{\frac{\left(\frac{dp}{dx}\right)_l}{\left(\frac{dp}{dx}\right)_g}} \quad [2.35]$$

$$X_l = \frac{U_{ls}}{U_{ls} + U_{gs}} \quad [2.36]$$

where U is the characteristic velocity of the flow and $\left(\frac{dp}{dx}\right)_l$ and $\left(\frac{dp}{dx}\right)_g$ are the pressure gradients generated if only the liquid flows in the pipe at the same flowrate, or if only the gas flows in the pipe at the same flowrate respectively.

Fossa et al. (2003) correlated the Strouhal number, considering gas superficial velocity as the flow velocity, with a function dependent on the liquid fraction as follows:

$$St = \frac{f\ D}{U_{gs}} = \frac{\mathrm{A}\ X_l}{1 + B\ X_l + C\ X_l^2} = \frac{0.044\ X_l}{1 - 1.71\ X_l + 0.7\ X_l^2} \quad [2.37]$$

They adjusted the coefficients A, B and C to their experimental data in horizontal pipes. They obtained an excellent fitting with their data and good agreement with literature data on horizontal flow.

Several researchers plotted the Strouhal number against Lockhart-Martinelli parameter in logarithmic scale (Hernandez-Perez 2008, Azzopardi et al., 2014, Abdulkadir et al., 2016). The points in the graphs collapsed into a straight line. From this observation, it was deduced that there is a power law relationship between the Strouhal number and the Lockhart-Martinelli parameter:

$$St = A\,\chi^{n} \qquad [2.38]$$

If both Strouhal number and the Lockhart-Martinelli parameter are to be obtained using equations [2.34] and [2.35], then the frequency can be directly calculated.

2.5 Current limitations in the understanding of intermittent flows

As mentioned earlier, gas-liquid intermitted flow occurs under different conditions including different gas and superficial velocities, diameter and inclination of the pipe, physical properties of the fluids (i.e. density, viscosity or surface tension), distance from the mixing point, and even the geometry of the mixer.

Many experimental analysis studies of intermittent flows in small pipe diameters have been produced, that includes flow in both horizontal (Hubbard and Dukler, 1966, Wallis, 1969) and vertical (Hewitt and Roberts, 1969, Costigan and Whalley, 1997) pipes. Contrarily, considerably less number of investigations have been carried out in inclined pipes covering all the range from horizontal to vertical (Spedding et al., 1982, Bendiksen, 1984). In addition, there is a general lack of data for two-phase flows in large diameter pipes, although, recently a few new experimental data has been published (Omebere-Iyari et al., 2008, Ali and Yeung, 2014).

Regarding consideration of the physical properties; it must be said that most of the experimental data presented in the literature were obtained using air and water at atmospheric pressure. Nevertheless, a few exceptions can be mentioned such as the work of Abdulahi (2014) who performed experiments using gas densities of 28 and 45 kg/m^3 and liquid viscosity of 35 cp in a 127 mm vertical pipe.

It has not come into existence yet a general expression or a model that determines the occurrence of intermittent behaviour as a function of all the variables named above. A model that has been tested successfully and validated successfully against experimental data. In other words, there are no set of equations that can predict the transition from any flow pattern to intermittent flow considering all the geometrical parameters of the pipe and the physical properties of the fluids. Although Weisman (1983) attempted to generalize a flow pattern map covering different fluids and pipe sizes, yet it has limited applicability because it presents a series of transitions depending on the fluid properties rather than a universal expression (Brennen, 2005).

Apart from its complexity, this problem has not been solved yet because the collection of data available in the literature does not cover an experimental matrix that is dense enough to permit a solution and validation. There are still many gaps corresponding to different experimental conditions that have not been studied in detail. These gaps are especially significant for large diameter pipes, inclined pipes, when liquids have a viscosity different than that of water, and when the gas has a density higher than that of air at atmospheric pressure.

In this work, gas-liquid two-phase flow was generated, characterised and analysed in vertical pipes of large diameters (67 and 127 mm). It also reports the findings of an experimental campaign in which the 67 mm diameter pipe was placed at different angles of inclination all the way from horizontal to vertical position. The liquid employed was

silicone oil with a viscosity of 5 cP (five times higher than that of water and more close to the viscosity of the petroleum oils). This data has attracted particular interest from the industry as they were used to validate numerical models (Issa and Galleni, 2015, Galleni and Issa, 2015) focussed on predicting intermittent flows for the hydrocarbons industry.

As mentioned previously, there are six characteristics that define the intermittent flows: the velocity of the periodicities, the frequencies of the periodicities, the length of the gas structures, the length of the liquid structures, the void fraction of the gas structures, and the void fraction of the liquid structures. Also, these characteristics depend on the gas and liquid superficial velocities and the geometrical and physical properties defined earlier. For this reason, many models and correlations have been published in the literature to characterise intermittent flows as a function of one or several of some variables such as the diameter of the pipe, inclination of the pipe, gas and liquid superficial velocity, Reynolds number, Weber number, the density of the fluids, etc.

Some expressions to predict the velocity and the frequency of the periodic structures in gas-liquid intermittent flows were reviewed in the previous sections. These expressions have been deducted either fully or partially by empirical methods. This means that they are based on experimental data that is limited by the specific conditions at which it was carried out. For example: experiments performed at a certain pipe diameter or only obtained at one position (vertical, horizontal or a fixed angle), using only water which has a fixed viscosity, operating in a gas and liquid flow range that does not cover the entire region of intermittent flow regimes, etc. For these reasons, these expressions must be tested against experimental data obtained at different conditions. For instance, almost all the studies about the velocity of the gas structures included a comparison against Zuber and Findlay (1965) model which was initially deduced from experiments in

vertical pipes using combinations of air-water, steam-water and air-glycerine. On the other hand, many of the frequency studies were compared with the predictions of Gregory and Scott (1969) correlation which was developed for horizontal flows using air and water. Often, these correlations or models get modified by adding terms or including more variables to adjust them with the new experimental data obtained at different conditions. For instance, Frechou (1986) expressed the distribution coefficient of the drift flux model as a function of the Reynolds number. Also, Zabaras (1999) who added an angle of inclination dependent term to the correlation of Gregory and Scott (1969) which enabled the prediction the frequency of gas structures in slightly deviated angles from the horizontal.

In this work, some experiments of gas-liquid intermittent flows were obtained in pipes of large diameter (67 and 127 mm) in the vertical position and in different inclinations in the case of the 67 mm diameter using air and silicone oil (which viscosity is 5cP). The results of the velocity and the frequency of the gas structures were compared with the relevant expressions detailed in the literature which were formulated from data obtained at different experimental conditions. Since there was not a good agreement in most of the cases; as demonstrated by Escrig et al. (2016) or as can be manifested by the discussions presented in Chapter 5, 6 and 8; it proved necessary to formulate new models and correlations that converge better with the experimental results produced in this work.

Finally, the geometry of the gas and liquid mixer is a geometrical parameter that affects the flow development in gas-liquid intermittent flows which has not been studied in detail. The gas is introduced into the liquid phase through the holes of the mixer. The number of holes as well as their area, orientation and position define the geometry of

the mixer. A study on the influence of the mixers on the characteristics of intermittent flows is detailed in Chapter 7.

CHAPTER 3.

EXPERIMENTAL ARRANGEMENT

This chapter describes the fluids used, the flow facilities on which the experiments were performed, the instrumentations installed on the rigs to control flows, pressure and temperature and the advanced measurement techniques used to quantify the gas- liquid two-phase flow.

3.1 Fluid properties

The fluids are identical for all the experiments carried out on the different facilities in order to enable comparison of the geometrical parameters only. Compressed air was used as the gas phase and in the case of the liquid phase silicone oil with a viscosity of 5 mPa·s was employed. Physical properties of both fluids at 20 °C and at atmospheric pressure are summarised in Table 3.1.

Table 3.1. Silicone oil and air physical properties at 20 °C and 1 bar

	Density [kg/m^3]	Viscosity [µPa·s]	Surface tension [N/m]	Conductivity [S/m]	Relative permittivity to air [-]
Oil	917	5000	0.02	3×10^{-15}	2.7
Air	1.204	17.4		1×10^{-13}	1

3.2 Rigs description

Two different flow facilities were used to study the intermittent flows in this work. Both of the apparatuses are gas-liquid loops. The flows of the two phases could be controlled and measured separately and then combined in a mixer at the inlet of the test pipe. The test section, mounted further downstream the mixing section, contains the sensors that

measure the flow characteristics. These sensors are specific for multiphase flows and their measurement principles are based on capacitance sensing. Further explanation will be provided towards the end of this chapter. The main difference between the two experimental rigs is the diameter of the test section: 67mm for the first rig and 127 mm for the second. Now and hereafter in this thesis, both rigs will be referred to by their pipe diameter.

3.2.1 67 mm diameter rig

This flow facility has been in one of the laboratories at the University of Nottingham since 2005. Many works were produced based on experimental results obtained from this rig using different fluids with specific properties, at different flows rates and applying each time more advanced measurement techniques (Hernandez-Perez 2008, Abdulkareem, 2011, Kanu, 2013).

The liquid phase (silicone oil) is stored in a 600 litres tank. It is driven by a centrifugal pump through piping connections to the vertical test section. The test section is often referred to as the riser. The liquid flow is controlled using a by-pass line (V1 in Figure 3.1) around the pump, and by two parallel and independent sets of valves (V2 and V3). The flowrate is measured by two variable area flowmeters capable of measuring the flow from 3 to 10 l/min and from 20 to 100 l/min respectively (uncertainties of the flowmeters are included in the Appendix). Two cooling systems are installed on the oil lines to maintain the oil temperature constant since it gets constantly heated by the energy introduced by the pump. One cooling system is a copper coil inside the tank and the other is a two meters long concentric cooling jacket around the pipe following the pump. Liquid flow lines are drawn in Figure 3.1 in blue and the cooling water system appears in black.

The air is supplied by the laboratory compressed air mains. It provides a maximum pressure of 6 bars but it gets reduced to 1.5 bars by a pressure reducing valve (V4) in order to maintain constant pressure and protect the facility from overpressure. Following the pressure reducing valve, there are three variable area flowmeters installed in parallel ranging from 1 to 15 l/min, 10 to 100 l/min and 100 to 1000 l/min. The flow into each line is controlled by the valves marked V5, V6 and V7 in Figure 3.1. The pressure in the line immediately following the flowmeters is measured by a pressure gauge in order to be able to normalise the flowmeters measurements to atmospheric pressure. Gas lines are represented in red in the flow diagram shown in Figure 3.1.

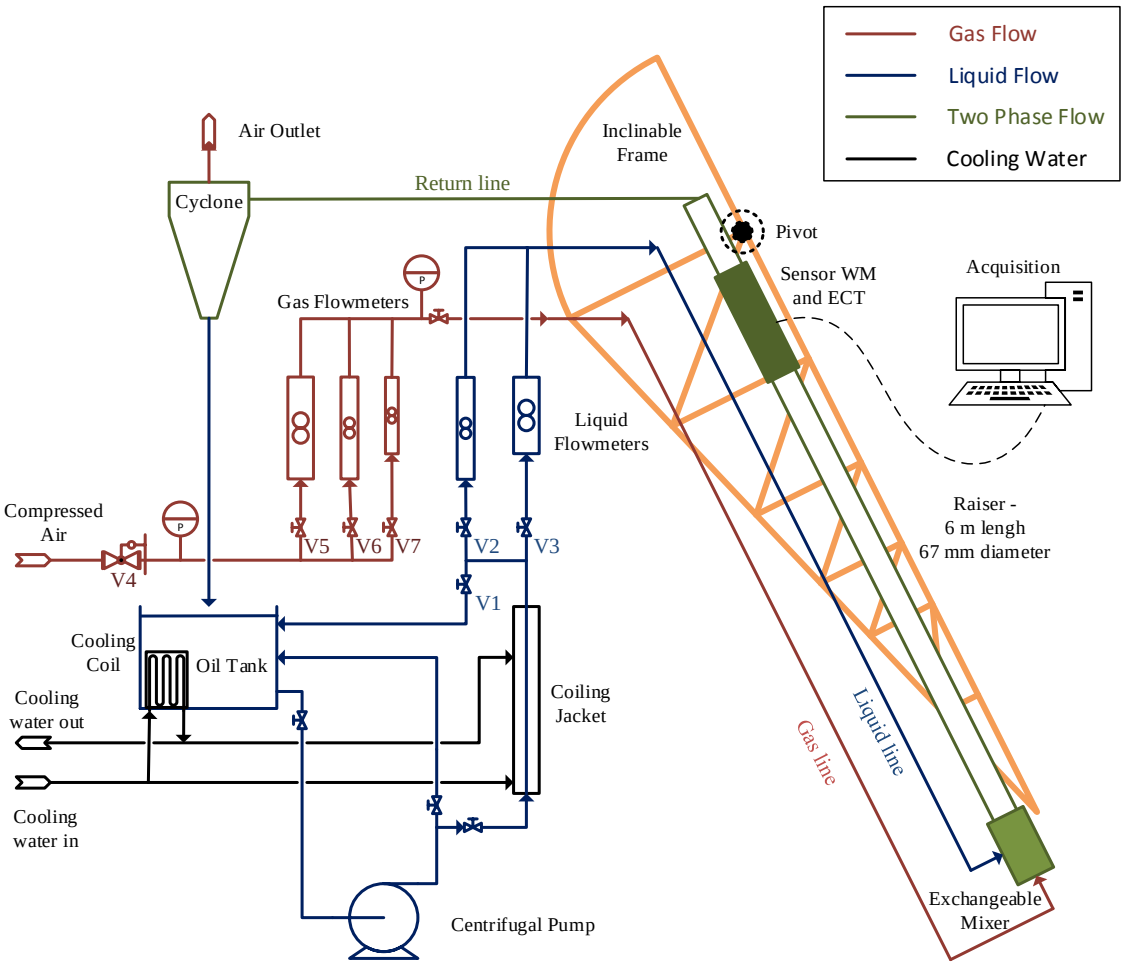


Figure 3.1. 67 mm rig flows diagram.

Gas and liquid flow pipes are fed into a mixer, which is placed at the base of the test section (or the riser) where both fluids are brought together to generate the two-phase

flow. This unit is interchangeable and different designs of mixers can be employed as will be exhaustively detailed in Chapter 7.

The riser is mounted on a steel frame that is supported by a pivot. Therefore, the riser can be turned from the vertical position to 15° above the horizontal in steps of 5°. The riser is a 6 metres long acrylic pipe with 67 millimetres inner diameter. It is composed of flanged segments of 1 and 2 meters in length bolted to each other. That makes it possible to position the measuring devices in between these segments at different axial locations along the length of the riser.

The liquid-gas mixture leaving the riser is fed to a cyclone where the phases are separated. The oil flows back to the tank and the air is vented to the atmosphere through a filter to prevent the release of entrained liquid drops with the air. The two-phase flow starts at the mixer and finishes in the cyclone, the lines it takes place within are represented in green in Figure 3.1

Two capacitance-based measuring devices are mounted on the test section. A twin plane Electrical Capacitance Tomography sensor (ECT) was positioned closer to the mixer compared to the other sensor. The first plane of the ECT was at 4.4 m distance from the mixer (66 pipe diameters length), the second plane was 89 mm downstream from the first. A Wire Mesh sensor (WMS) was located downstream the ECT, at 5 m axial distance from the mixer (75 pipe diameters length). The WMS was located downstream of the ECT since the wires of the WMS cross the pipe and disturb the flow whilst the ECT is not at all intrusive.

3.2.2 127 mm diameter rig

The 127 mm diameter rig has recently been rebuilt at University of Nottingham flow laboratories. It is a two-phase flow loop that can work as open or closed-loop

configuration. Apart from having a considerably larger test section diameter, the peculiarity of this rig arises in the fact that it can work at higher pressures when operated as a closed loop.

The liquid is stored in a 2 m^3 tank that also operates as a gas-liquid separator. From this tank, the liquid is driven by a centrifugal pump to the liquid line. The liquid line passes through a heat exchanger where the liquid is cooled down to eliminate the heating generated by the friction in the pump. The heat exchanger is a shell and tubes configuration; the oil goes in the shell side while the tubes are connected to the central cooling water line. This heat exchanger can dissipate up to 10 kW of heat. After the heat exchanger, the liquid line splits into two branches; one line delivers the liquid back to the tank as a by-pass (V1), while the other leads the liquid to the riser (V2). Around this junction, the two valves (V1 and V2) are adjusted to control the liquid flow. The line going to the riser contains a turbine gas flowmeter, a pressure gauge and a thermocouple. These readings are monitored and recorded in a computer. The liquid line delivers the liquid to the gas-liquid mixer at the bottom of the riser. In Figure 3.2 the liquid flow piping is represented by blue lines.

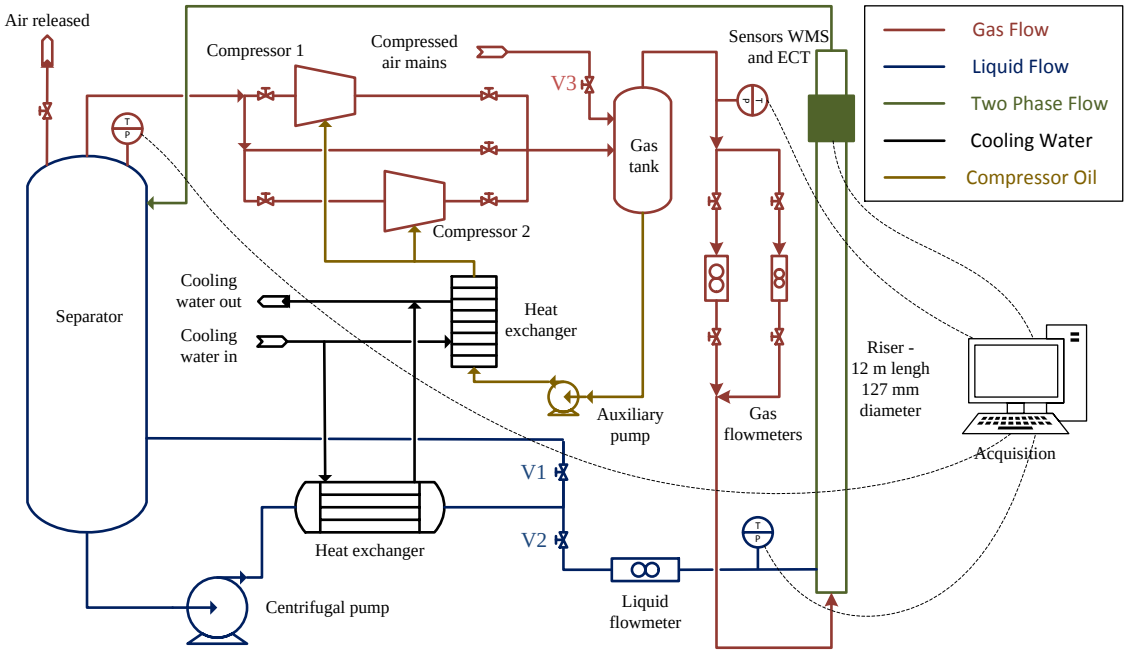


Figure 3.2. 127 mm rig flows diagram

When the rig is operated in open loop configuration, the only gas that can be used is air. It is supplied by the 6 bars compressed air mains and introduced into the gas tank. The gas flow is controlled using a valve (V3). In the closed loop configuration however, any gas can be used whereby it can be pressurised up to 6 bars. In this case, the gas is circulated by two liquid ring compressors positioned in parallel and the flow is controlled by frequency converters connected to the compressors' motors as well as by a by-pass valve. At the exit of the gas tank there are two gas flowmeters mounted in parallel, one measures the gas flow in the range from 5 to 2800 l/min and the second from 1000 to 12000 l/min. Beyond the flowmeters, the gas travels to the mixer at the bottom of the riser. The pressure and the temperature in the air line are monitored and recorded in a computer. In Figure 3.2, the gas flow piping is represented by red lines.

The mixer is composed by a T-junction to facilitate the introduction of the two fluids into the riser. One inch ID concentric tube is used to introduce the gas through the bottom and the liquid is introduced from the side arm of the Tee as seen in Figure 3.3.

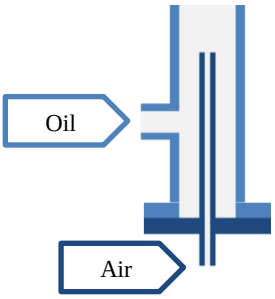


Figure 3.3. Mixer diagram

The riser is 127 mm inner diameter and 12 meters long. It is made of stainless steel to withstand high pressure, however it has two clear sections 150 mm long made of transparent acrylic glass to enable visual observation of the flow and allow optical measurement devices to be deployed. Downstream the second clear section in the riser at about one meter below the top of the riser, the wire mesh sensor is positioned. Once the two-phase flow reaches the top of the riser it is then directed back to the separator. The gas is released to the atmosphere in the separator when operating in open loop. In the case of closed loop the air is recirculated to the compressors. Sections where two-phase flow exists appear in green lines in the flow diagram presented in Figure 3.2.

The compressors, being of the liquid ring pump type, require liquid to compress the gas. This is supplied by some oil stored at the bottom part of the gas tank. It is driven by a small pump to the compressors where it is used to compress the gas. From there it flows together with the gas back into the tank where it separates by gravity. This oil is always in a close loop and it must not escape from the gas tank. A plate heat exchanger is installed to cool the oil by contacting with cooling water line to prevent the compressor and the gas from heating up. The compressors' oil line is drawn in yellow and the cooling water line is in black in Figure 3.2.

3.3 Measurements of the two-phase flow

The measurements of the multiphase flows were employed to obtain the gas-liquid distribution in different cross-sections of the pipe. The cross-sectional measurements obtained are for thin sections of the pipe perpendicular to the pipe's axis, it must be clarified that the data obtained by the measurement techniques is only from particular sections and does not cover the whole length of the pipe. The gas-liquid measurements in these cross-sectional distribution was acquired periodically at a high frequency (from 1000 to 4000 Hz) for a fixed period of time (1 minute).

The phase distribution measurements are processed in order to obtain valuable information, such as: void fraction time series, average void fraction, void fraction radial profiles, probability distribution function of the void fraction (PDF), image reconstruction of the flow, gas bubble identifications, bubble size distribution, gas structures velocity, gas structures frequency, etc.

All the aforementioned processed experimental variables are presented in Chapter 7 to analyse the influence of the gas injector on the gas-liquid intermittent flows. Although, the variables with particular significance in this work are the velocity and the frequency of the periodic structures in intermittent flows. The influence of the pipe diameter, the inclination of the pipe, and the gas and liquid superficial velocities on the velocity and the frequency of the gas structures are studied and presented in detail in Chapters 5, 6 and 8. In addition, a model to predict the velocity of the gas structures and a correlation to predict the frequency as a function of the diameter and inclination of the pipe and the gas and liquid superficial velocities are proposed.

The analytical methods employed to obtain all these relevant information from the raw data of the sensors are explained in detail in Chapter 4. On the other hand, the specific description and the uncertainties of the sensors are provided in the next section.

3.4 Measurement techniques

Two measurement techniques, namely the Wire Mesh Sensor (WMS) and Electrical Capacitance Tomography (ECT) were used in order to measure the temporal void fraction distribution in the cross section of the pipe. The results obtained from both sensors provide circular images representing a thin cross-sectional slice normal to the pipe axis. Each pixel of the image corresponds to a square area or cell in the pipe cross-section that can be filled by liquid, air or both in different proportions. The value of the pixel varies from 0, when fully occupied by liquid, represented in black; to 100, when filled with gas and represented in white as can be seen in Figure 3.4.

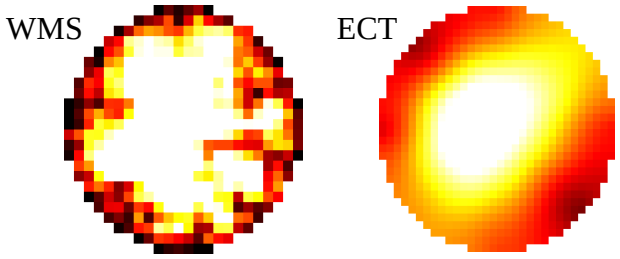


Figure 3.4. WMS and ECT results representation. Black is oil, white is air and yellow and orange tones are a mixture of both.

Both WMS and ECT measure the capacitance of the flow, the difference lies in the shape and position of the electrodes and how the capacitance measurements are related to the flow permittivity distribution. Once the permittivity distribution is known images such as the ones in Figure 3.4 can be obtained by applying permittivity reconstruction models.

In this section, it is explained how the electrodes are arranged and how the capacitance is measured by both the ECT and the WMS sensors. The way that the capacitance is related to the permittivity distribution and the permittivity to the void fraction will be described in the Chapter 4.

3.4.1 Wire Mesh Sensor

Wire Mesh Sensor was developed by Prasser et al. (1998) for air-water or steam-water flows based on conductivity measurements. Da Silva et al. (2007) modified the electronics to enable the measurements to be made using capacitance instead of conductance enabling measurement of non-conductive fluids such as oil. The sensors used by them were fabricated and tested at Helmholtz-Zentrum Dresden-Rossendorf (HZDR) research laboratory. The WMS used in the current work was supplied by the same research centre.

The WMS is composed of two planes of wires slightly separated which are parallel to the wires of the same plane and orthogonal to the ones in the other plane forming a grid. The thin wires of the two planes stretch across the pipe, making this method intrusive. The wires from one plane are switched on and off sequentially by a sinusoidal voltage supply. The wires from the other plane are connected to an AC current amplifiers that give a voltage as an output. Pairs of wires from different planes act as electrodes of a capacitor. Therefore, the intensity driven to the current amplifiers depends on the capacitance in between the wires. This capacitance is related to the proportion of oil and air filling the space between the wires. After calibration and applying permittivity models, the proportion of oil and air can be determined. Figure 3.5 shows a simplified scheme of the electronic connections for a square WMS with 4x4 grid, based on capacitance measurement.

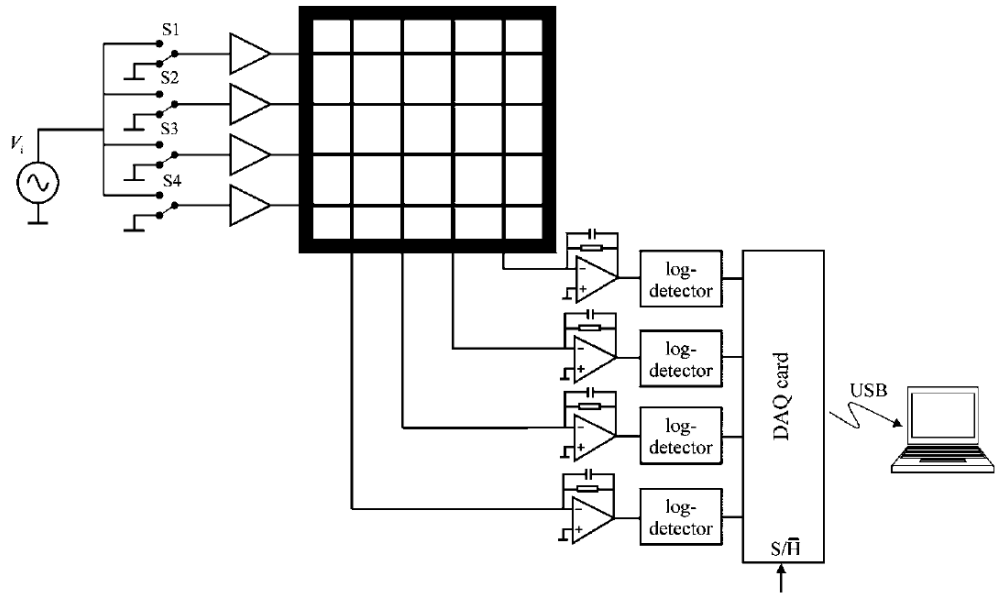


Figure 3.5. Simplified scheme of the wire mesh sensor (Da Silva et al., 2007)

In the 67 mm rig, a circular WMS with 24x24 equally spaced wires was employed. In the 127 mm rig, the sensor had 32x32 wires.

3.4.1.1 Uncertainty of the WMS

There are different sources of uncertainty in the Wire Mesh Sensor measurements. The most evident can be found in the intrinsic spatial and temporal resolution of the sensor. These are inherent in the pitch of the wires and the acquisition frequency of the sensor respectively. However, additionally, other sources of uncertainty appear at different stages of the measurement.

The first problem that poses uncertainty happens when a bubble touches the wires of the WMS whereby the velocity of the bubble is reduced because of the impact against the wires. The bubble will remain for a longer time contacting the wires consequently causing the sensor will register a higher void fraction than what it would have produced if the bubble had not been obstructed. However, this effect becomes negligible at high liquid superficial velocities (Prasser et al., 2005). The second source of uncertainty comes from the suitability of the permittivity model chosen to relate the permittivity

with the void fraction (different permittivity models are described in the Chapter 4). And finally, there is the quality of the signal which is affected by the electromagnetic noise.

It is difficult to quantify the uncertainty of the WMS since it depends on the particularities of each sensor, the isolation of the probes, and the conditions of the two-phase flow. However, it has been compared with other measuring techniques that are based on different principles and a good agreement was found. Prasser et al. (2005) compared the WMS with the ultrafast X-ray tomography and they revealed a difference of 1% in the void fraction average for bubble flow and a 4% difference for slug flow between the measurements obtained by both sensors. Sharaf et al. (2011) compared the void fraction average of the WMS with the gamma densitometry where they found a maximum difference of ±10%.

3.4.2 Electrical Capacitance Tomography

Electrical Capacitance Tomography is a non-intrusive method to visualise the content of a vessel or pipe by taking multiples capacitance measurements along the perimeter. An ECT sensor was installed in the 67 mm facility. The 127 mm rig described previously does not have an ECT sensor installed on. Therefore, the ECT measurements needed to calculate the gas structures velocity in the 127 mm pipe were performed in another rig with similar specifications. The alternative rig is made of plastic test sections that enables the ECT sensor to be easily installed. All the ECT probes employed in the present experiments were manufactured by Tomoflow Ltd.

The electrodes of the ECT are formed of rectangular copper foils attached to the outside wall of the pipe. The ECT used in both pipes (67 and 127 mm) has two planes of measuring electrodes. Each plane is composed of a ring of 8 electrodes positioned

around the pipe. Above and below (and between in the 67 mm rig) the measuring electrodes there are segmented guard electrodes. Additionally, a shield electrode connected to earth surrounds the entirety of the electrodes as can be seen in Figure 3.6. Apart from that, a grounded screen envelops all the electrodes to prevent external noise from distorting the signal. The length of the electrodes and the gaps in between them for the sensors in the 67 and 127 mm rigs are shown in Table 3.2 and

Table 3.3 respectively.

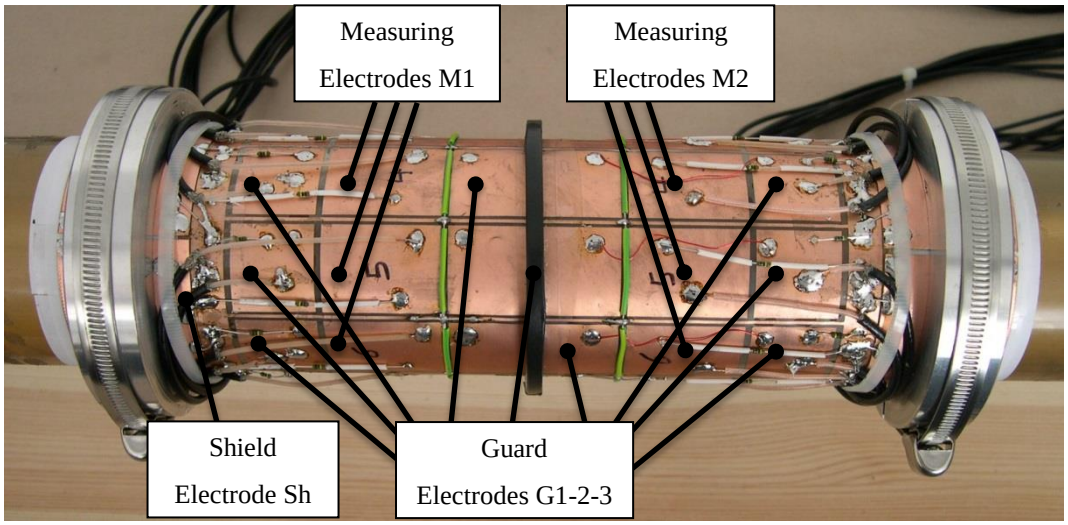


Figure 3.6. Electrodes arrangement in the ECT sensor.

Table 3.2. The length of the electrodes of the ECT in the 67 mm pipe and the gaps between them. Distances in the axial direction in millimetres.

Part	Sh	Gap	G1	Gap	M1	Gap	G2	Gap	M2	Gap	G3	Gap	Sh
Length [mm]	10	2	25	2	35	2	50	2	35	2	35	2	10

Table 3.3. The length of the electrodes of the ECT in the 127 mm pipe and the gaps between them. Distances in the axial direction in millimetres.

Part	Sh	Gap	G1	Gap	M1	Gap	M2	Gap	G3	Gap	Sh
Length [mm]	10	2	53	2	40	2	40	2	53	2	10

The measuring electrodes and guard electrodes are connected by shielded cables to the electronics box TFLR5000. The measuring electrodes in each plane are combined sequentially in order to measure the capacitance in between them. The total possible combination of measurements for a plane with 8 electrodes is 28. The capacitance values are very small, ranging between 1 fF to 1000 fF, are measured by charge-discharge circuits (Huang et al., 1988) contained in the TFLR5000 electronics box.

The ECT sensor can be triggered from the wire mesh sensor electronics box. A minimum delay of 0.3 seconds was observed.

3.4.2.1 Uncertainty of the ECT

The spatial resolution of the ECT depends on the number of electrodes and the number of capacitance measurements obtained by these electrodes. It also depends on the reconstruction algorithm employed and the number of iterations done to reconstruct the distribution of the two-phase (Yang and Peng, 2003).

Some tests of the different reconstruction algorithms to create virtual images were carried out and are reported in the next chapter. The limitations of these algorithms are evidently explained and discussed. However, the average void fraction of the cross-section of the reconstructed image and the virtual image are almost overlapping. It must be emphasised that, when working with real data instead of virtual images, electrical noise and non-linear relationships become significant making the reconstruction poorer.

Azzopardi et al. (2010) compared the ECT with the wire mesh sensor and they found that the overall void fraction measured by the ECT and the WMS showed a good agreement.

The ECT with two measuring planes is used as well to measure the velocity of the gas structures. The uncertainty of these measurements is detailed in the Appendix.

3.5 Testing of the experimental facilities

The measurement instrumentations employed in the acquisition of the data must be tested in order to ensure the validity of the results. These instruments include the flowmeters used to set up the flow conditions and the two-phase flow measurement techniques employed: Wire Mesh Sensor and Electrical Capacitance Tomography.

Furthermore, the repeatability of the experiments was assessed. The same experimental conditions were reproduced on different days whereby the results obtained on different days were compared.

3.5.1 Testing of the flowmeters

3.5.1.1 Gas flowmeters

Two different types of gas flowmeters were used; volumetric and thermal mass flowmeters. One mass flowmeter was used in the 127 mm diameter rig and it came with the calibration curve certified provided by the manufacturer. On the other hand, two volumetric flowmeters, which are flowmeters of the variable area type, were installed in the 67 mm diameter rig (Figure 3.7).

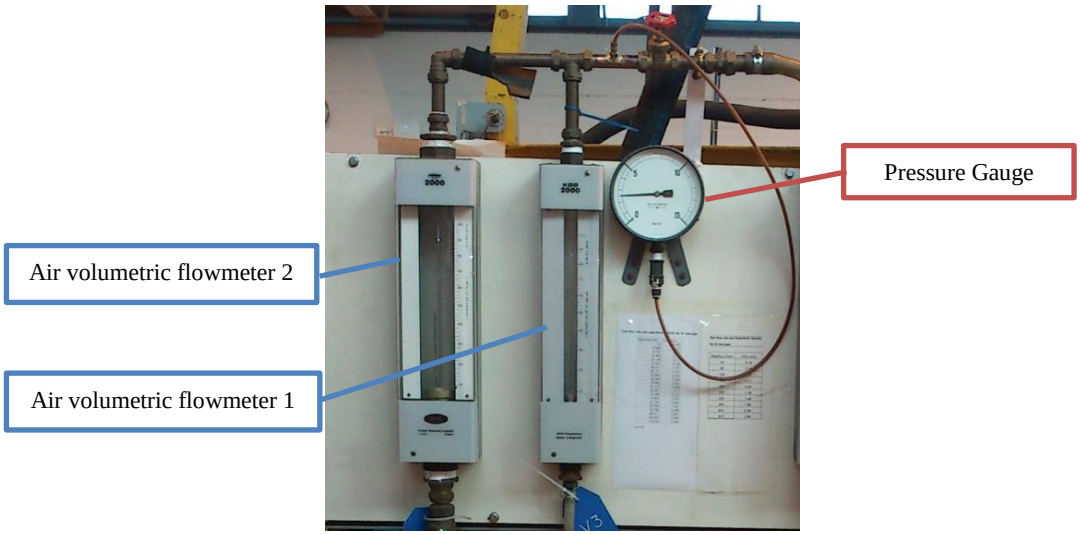


Figure 3.7. Air volumetric flowmeters and a pressure gauge in the 67 mm diameter rig.

These volumetric flowmeters were calibrated and certified by the manufacturer at the atmospheric pressure. Since they can operate at different pressures in the rig, the reading must be corrected by applying

$$Q_g = Q'_g \sqrt{\frac{P}{P_0}} \qquad [3.1]$$

where Q_g is the real volumetric flow, Q'_g is the flow read from the flowmeter, P is the pressure of the gas after the flowmeter and P_0 is the pressure at which the flowmeter was calibrated.

3.5.1.2 Liquid flowmeters

Also volumetric and mass flowmeters were used to measure the liquid flow. The mass flowmeters installed in the 127 mm diameter rig were calibrated and certified by the manufacturer. These calibrations are valid for any type of liquid used in the rig.

On the other hand, the volumetric flowmeters, which were of the variable area type, were used in the 67 mm diameter rig. These flowmeters needed to be calibrated separately for each liquid employed. Since the original calibration was done using water, a new calibration was needed for the silicone oil employed in the present experiments.

The calibration was accomplished following these steps: draining the oil off the rig, set up the liquid flow to a constant value, start filling the vertical test section of the rig with oil, take the reading of the flowmeter, and measure the time the liquid needs to advance to a known distance along the pipe. The distance considered was the axial distance in between the planes of the ECT. The time the liquid took to move from one plan to another was obtained by calculating the delay between the signals acquired by the two ECT planes. The flowmeters calibration curves were obtained by repeating this process

at different liquid flows. They are presented in Figure 3.8 where they display the relationship between the readings of the flowmeter and the liquid superficial velocity.

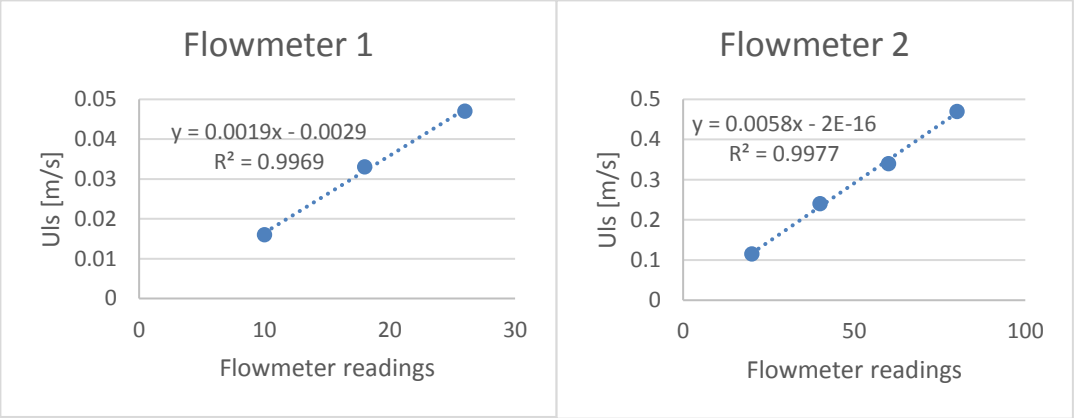


Figure 3.8. Calibration curves of the volumetric liquid flowmeters in the 67 mm diameter rig.

3.5.2 Testing of the sensors

The wire mesh and electrical capacitance tomography sensors were tested and commissioned by the manufacturers, it was assured that the sensors were measuring the right capacitance between all the electrodes. However, an additional test was performed in the lab to validate the void fraction measurements. To do that, the test section, where the ECT and WMS were installed, was fixed in a horizontal position in the 67 mm diameter rig. The section was filled with oil to different levels. Knowing the oil level and the diameter, the void fraction in the cross-section of the pipe could be calculated and compared with the void fraction measured by the sensors. Figure 3.9 shows these comparisons, in the first column a schematic image of the liquid level in the pipe is shown, in the second and third columns the reconstructions of the WMS and the ECT are displayed respectively. Additionally, the void fraction corresponding to each image is marked below them (further explanation of the WMS and ECT reconstruction is given in the next chapter). It can be seen that the divergence between calculated void fraction using the liquid level and the void fraction measured by the sensors is not higher than 3% in all the cases.

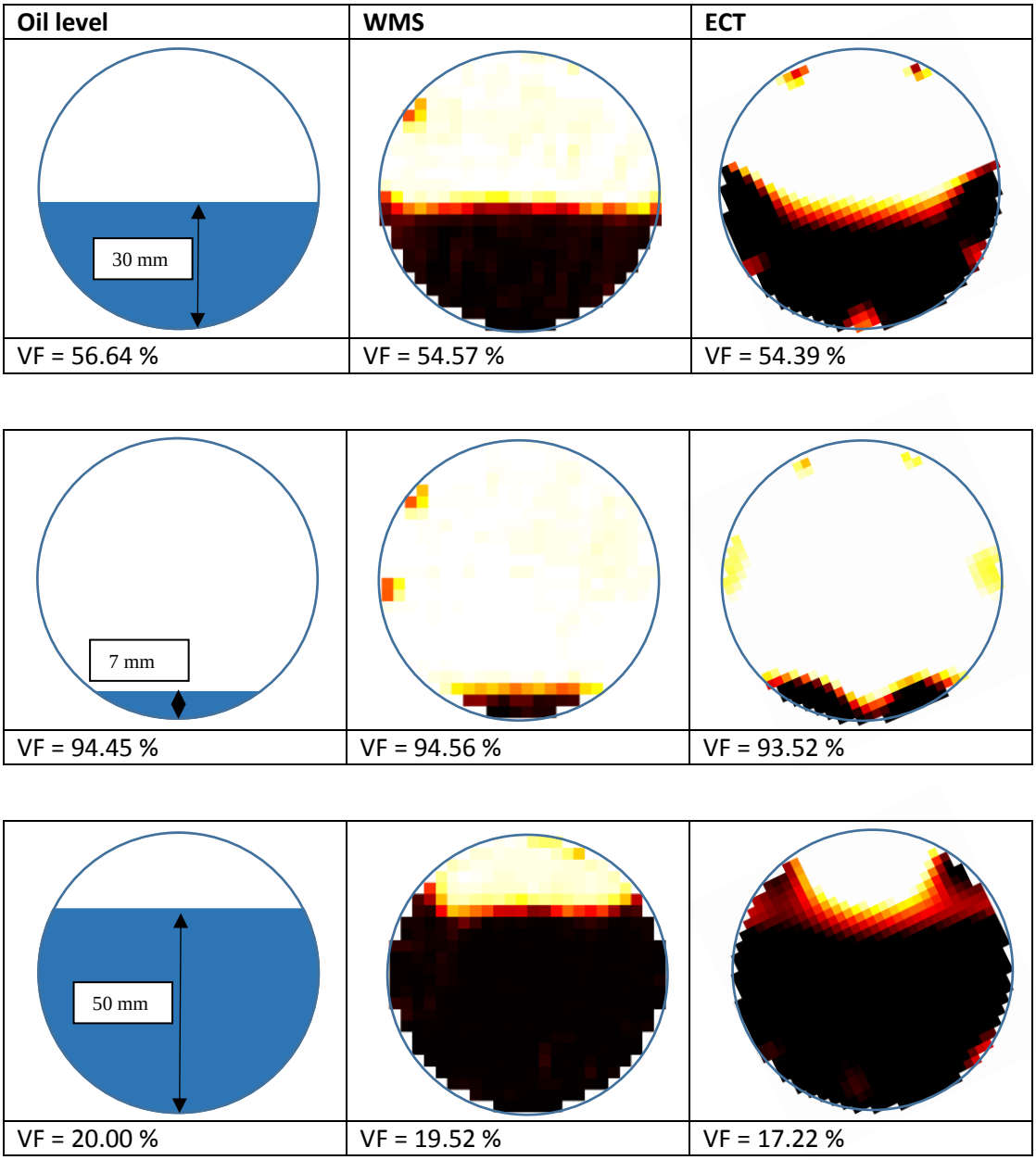


Figure 3.9. Different liquid levels and the image reconstructions with the WMS and the ECT in the 67 mm diameter rig. Below, void fraction (VF) of each image.

A similar test was also performed with the sensors in the 127 mm rig, however in this case it was not possible to mount the test section in the horizontal position. Therefore, the test could only be performed with the pipe empty and fully filled with oil. Figure 3.10 shows the comparison of different liquid levels with the reconstruction of the WMS

and the ECT. Expectedly, it can be seen that there is a good agreement between both void fractions since they do not differ by more than 1.1%.

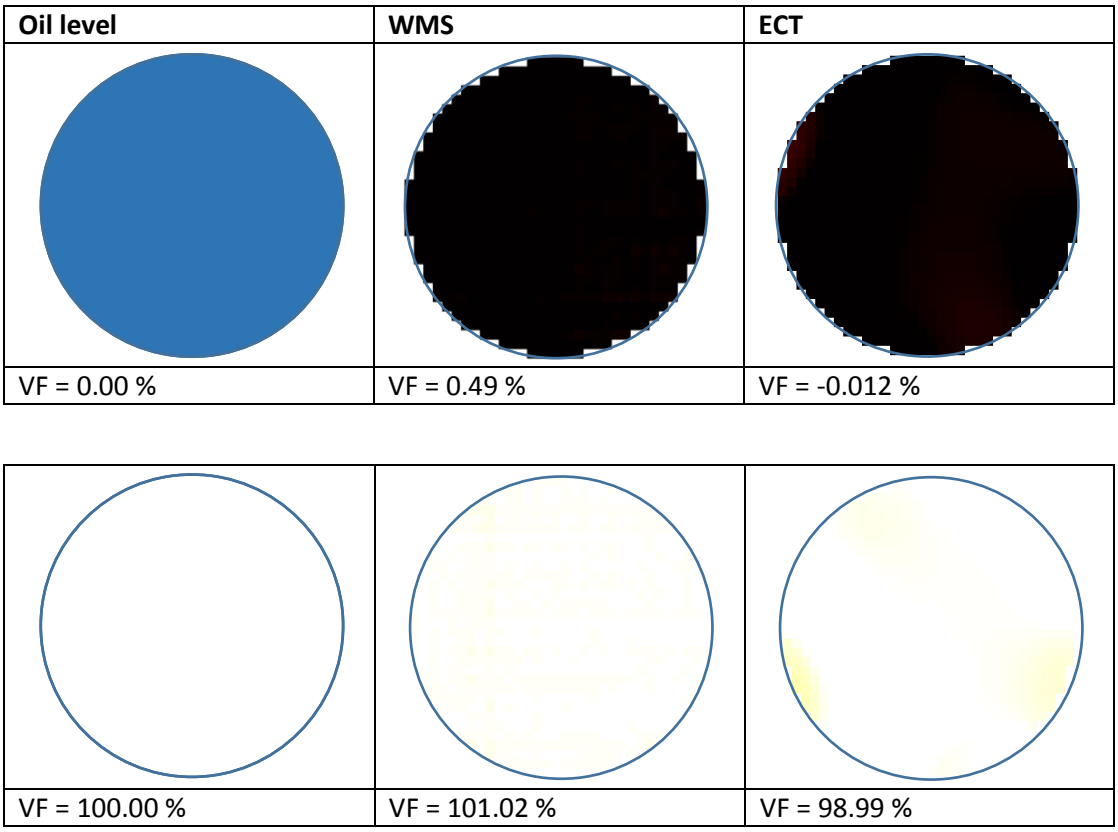


Figure 3.10. Different liquid levels and the image reconstructions with the WMS and the ECT in the 127 mm diameter rig. Below, void fraction (VF) of each image.

3.5.3 Testing the repeatability of the experiments

Several experiments at different gas and liquid superficial velocities were repeated on different days in both rigs. In the 67 mm diameter rig, the gas superficial velocity was varied from 0.5 to 2.3 m/s and the liquid superficial velocity from 0.1 to 0.5 m/s. The values of the average void fraction obtained by the WMS and the ECT on the first day were compared with those obtained on the second day at the same flow conditions. The results of the comparison are shown in Figure 3.11. The first graph compares the results of the WMS and the second graph shows that of the ECT. It can be seen that the results

on different days do not vary considerably whereby the maximum difference is only about 5%. Therefore, it can be said that the experiments are repeatable.

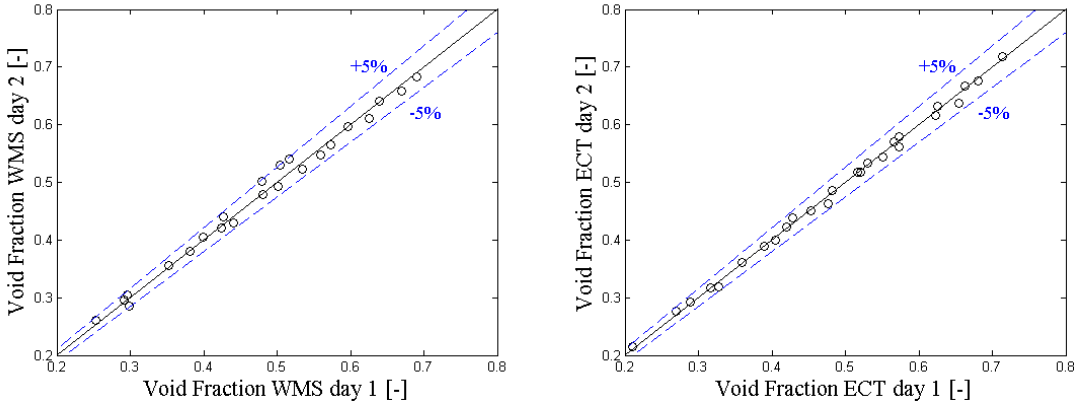


Figure 3.11. Comparison of the average void fraction obtained under the same conditions on different days in the 67 mm diameter rig using WMS and ECT.

A similar comparison was carried out in the 127 mm diameter rig. In this case, the superficial velocity of the gas was varied from 0.17 to 2.32 m/s and that of the liquid was varied from 0.1 to 0.35 m/s. The results of the comparison are presented in Figure 3.12. It can be seen that the repeatability is evident and the difference does not exceed

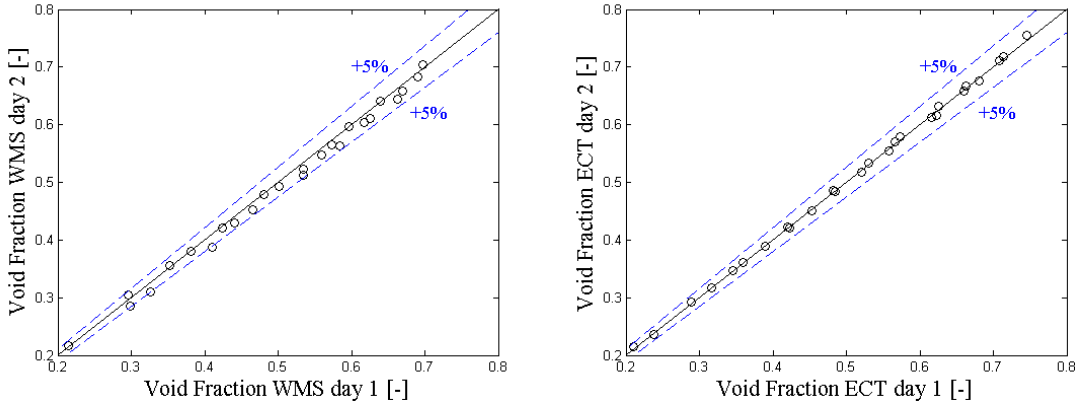


Figure 3.12. Comparison of the average void fraction obtained under the same conditions on different days in the 127 mm diameter rig using WMS and ECT.

CHAPTER 4.

DATA PROCESSING AND ANALYTICAL METHODS

This chapter explains the processes followed to produce the characteristics describing the intermittent two-phase flow from the raw data obtained using the WMS and the ECT sensors. These processes are applied to generate the data presented in the chapters that describe the behaviour of the flow under varying conditions. The processed results provide valuable information such as; reconstruction of the flow, the velocity of the periodic structures, and many others that permit the study of the two-phase flow.

The first part of the chapter explains how the normalised capacitance values are obtained from the raw voltage values acquired by the two sensors mentioned above. This step is essentially achieved through a calibration process.

The following section describes how the permittivity distribution in the thin cross-section of the pipe is determined after evaluating the capacitance measured using the sensors. This process presents an ill-posed problem (Hadamard, 1923), in this case it means that the solution is not unique. Therefore, some assumptions and simplifications must be applied to the electromagnetic equations in order to solve this problem. The resolution for the ECT is different than that for the WMS sensor. Therefore, they are explained separately. Nevertheless, the result in all the cases is a 3D matrix of permittivity distribution. Two dimensions of the three in the matrix are spatial. They define the plane of the cross-section considered. The third dimension is time.

There are a number of models that can be applied to determine how the permittivity distribution is related to the void fraction. The product of this process is a 3D matrix of

void faction with the same dimensions as the permittivity distribution matrix. This matrix can be used to reconstruct a 3-dimensional two-phase flow distribution.

The subsequent sections of the chapter explain how useful information about the flow is extracted from the 3D void fraction matrix generated by both sensors. The aforementioned information is later presented in the results chapters as: void fraction time series, void fraction probability functions, void fraction diametrical time series, radial profiles of void fraction distributions, bubble size distributions, etc. Further analysis permits as well the calculation of other fundamental characteristics of the intermittent flow, which includes: mean void fraction, velocity, length, and frequency of the liquid and gas structures, etc.

Figure 4.1 shows the steps of the data processing from the raw data stage to analyzable results. Calculations, models and algorithms used for all these data processing were implemented using Matlab.

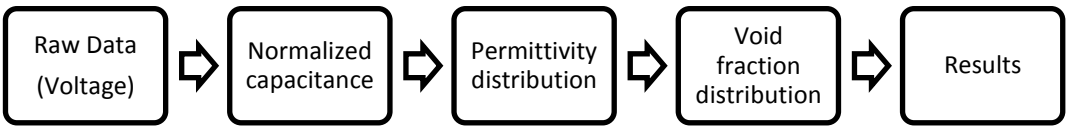


Figure 4.1. Data processing flow diagram.

4.1 Normalized capacitance

The output of both sensors (ECT and WMS) is a combination of voltage signals that are registered in a computer at a selected frequency of acquisition. These signals are the output of a circuit measuring the capacitance as explained in Chapter 3. The relationship of the voltage to the capacitance is known to be linear in the ECT circuit (Byars, 2001). In the WMS case, this relationship is exponential since the circuit is connected to a logarithmic detector (Da Silva et al., 2007). The capacitance values can be expressed then as:

$$C_x^{WMS} = A^{WMS}\, e^{V_x^{WMS}} + B^{WMS} \quad [4.1]$$

$$C_x^{ECT} = A^{ECT} \cdot V_x^{ECT} + B^{ECT} \quad [4.2]$$

where *C* is the capacitance at any specific acquisition *x* and *V* is the output voltage.

The coefficients A and B for both ECT and WMS sensors can be calculated through a rigorous calibration process. The calibration consists of obtaining the voltage values when the sensor is fully filled with oil (V_{oil}) and then the ones with air (V_{air}). However, it is not required to know the capacitance value in any specific unit (in the range of few pF) when the sensor is filled with oil or air for the calibration. That is because it can be considered as a normalized capacitance regarding it a 0 when the pipe is filled with air and 1 when it is flooded with oil. The normalisation can be expressed as:

$$C_x\,(V_x = V_{air}) = 0 \quad [4.3]$$

$$C_x\,(V_x = V_{oil}) = 1 \quad [4.4]$$

Substituting equations [4.3] and [4.4] into the ECT and the WM equations [4.1] and [4.2] respectively; the coefficients *A* and *B* for both sensors can be calculated separately. It must be noted that these coefficients are different for each pair of electrodes in each sensor.

4.2 Cross-sectional permittivity distribution

The local capacitance values measured are induced by the permittivity of the composition in-between the electrodes. These electrodes are either surrounding the pipe's perimeter in the case of the ECT sensor, or crossing a pipe cross-section in the case of the WMS. To calculate the expected capacitance once the permittivity distribution in between the electrodes is known is a direct problem with a unique solution. Conversely, the inverse problem, which is what is solved in this case; has many

solutions. It is an ill-posed problem, meaning that many permittivity distributions can lead to the same measured capacitance value (Yang and Peng, 2003). To find a single realistic solution to the ill-posed problem, some assumptions and simplifications must be implemented.

A first common assumption for both sensors is that the solution should be discrete. The cross section of the pipe is divided into square cells as shown in Figure 3.4. Inside each cell, the permittivity is considered constant. In other words, the solution is the permittivity value inside each cell and the number of values to be evaluated should be equal to the number of cells covering the cross-section of the pipe.

The second general assumption is that the maximum permittivity expected in a cell will be the oil permittivity. On the other hand, minimum permittivity will be equal to that of the air. Although sometimes, permittivity registers values slightly outside this range. In which case they must be truncated into these limits. Obviously, permittivity outside the operation range is unrealistic and possibly caused by external electromagnetic noise distortions. It also can happen that, in an iterative mathematical approach, the solution converge outside the limits, then the solution must be corrected (truncated) following each iteration.

Other approaches are different for each sensor, they are explained separately in the following sections.

4.2.1 WMS permittivity distribution

WMS sensor has two planes of wires stretching across the pipe forming a grid. In Figure 4.2 the wires are represented by the blue lines. The black circle is the pipe perimeter. In each point where two wires cross a square cell is drawn bounded by black dashed lines.

Cells that mostly fall inside the pipe are filled in green and cells mostly outside of the pipe are filled in white.

It is intended to only measure the permittivity of the cells inside the pipe. To do so; it is considered that the capacitance measured by the two crossing wires depends solely on the permittivity value of the material in between the wires. Whatever occupies the other cells does not affect the capacitance measured by the two wires. That is an assumption that simplifies the problem. Other cells actually have some influence on capacitance between the crossing wires. That effect is known as cross-talking but its influence on the results is minimum; therefore it is not considered in this application (Prasser et al., 1998).

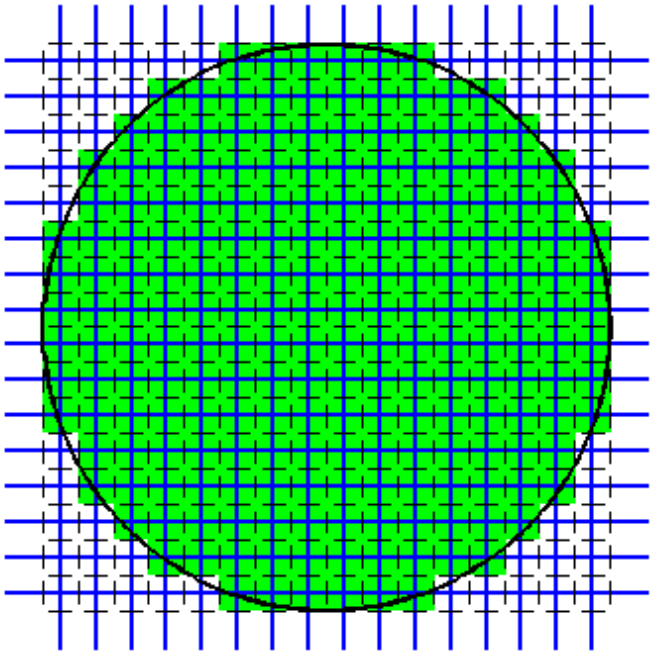


Figure 4.2. WMS 16x16 grid. Blue continuous lines are the wires, the black circle is the pipe perimeter, the dashed black lines enclose the cells, filled green cells are inside the pipe and white cells are out of the pipe

Capacitance and permittivity can be easily related once it is assumed that the capacitance between two crossing wires depends only on the homogeneous permittivity

inside the square cell. With these considerations, capacitance (C) and permittivity (ε) are linearly related as follows:

$$\varepsilon_x = a \cdot C_x + b \qquad [4.5]$$

Coefficients *a* and *b* can be calculated if the permittivity of the air and the oil, ε_{air} and ε_{oil}, are known. Therefore, equation [4.5] can be used to reconstruct the distribution of the permittivity in a cross-section of the pipe. The permittivity of air must be obtained when the normalized capacitance is 0. In the same way, the permittivity of the oil corresponds to a normalized capacitance equals to 1.

$$\varepsilon_{air} = \varepsilon_x\,(C_x = 0) \qquad [4.6]$$

$$\varepsilon_{oil} = \varepsilon_x\,(C_x = 1) \qquad [4.7]$$

The permittivity of the air relative to that of a vacuum is approximately 1. And the permittivity of the silicon oil relative to that of a vacuum is 2.7.

4.2.2 ECT permittivity distribution

As mentioned earlier, the solution for the permittivity distribution is a set of values whereby each of these values corresponds to the permittivity inside the cell. And each cell is a division of the pipe cross-section. The number and size of cells can be decided arbitrarily and it is independent of the number of electrodes and the pipe diameter. For round pipes and 8 electrodes normally a grid of 32 by 32 cells is generated. All the cells with more than 50% of its area located within the pipe cross-section are chosen. Figure 4.3 shows the cells that are considered in this case, they are a total of 812 cells inside the circle.

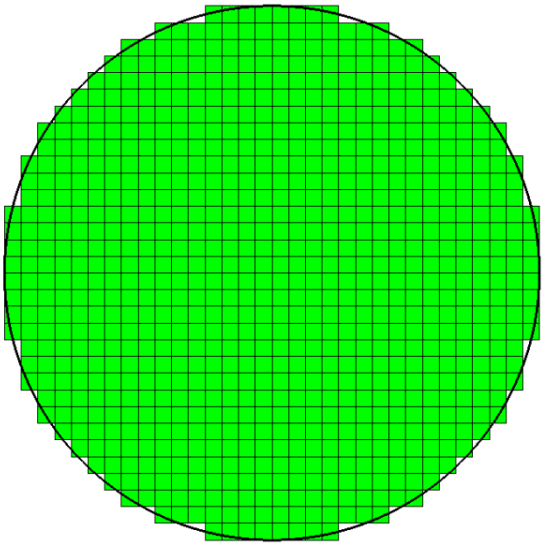


Figure 4.3. ECT permittivity cells in a 32x32 grid.

Electrical capacitance tomography algorithms need, as apriori information, to determine how much would the capacitance between the electrodes change by varying the permittivity in each of the cells individually. The simplified models assume that this variation is linear and independent of the permittivity values in the other cells (Yang and Peng, 2003). This information is collected in the well-known sensitivity matrices (Huang et al., 1988) which can be composed experimentally or computationally. The first method for the composition consists of introducing a square bar, whose cross-section has the same size as the cell area, with a known permittivity, in the position of the first cell. Then measure the capacitance variation between the electrodes. After that, the process is repeated for all other cells positions. The second method is achieved by solving computationally the Helmholtz equation of electromagnetism using finite elements method. This second approach is chosen for the analysis of this work. The solution of the electromagnetic equation for the ECT sensor was provided by the manufacturer (Tomoflow Ltd).

The capacitance variation between all the electrodes can be calculated using the permittivity matrix when the permittivity in all the cells is known. This is expressed in equation [4.9].

$$\underset{M\times 1}{\Delta C} = \underset{M\times N_c}{J} \times \underset{N_c\times 1}{\Delta\varepsilon} \qquad [4.8]$$

where ΔC is the capacitance variation, J the sensitivity matrix, $\Delta\varepsilon$ the permittivity variation, M the number of capacitance measurements (28 with 8 electrodes) and N_c the number of cells (812 in this case).

Equation [4.8] is normalised to:

$$\lambda = S\, g \qquad [4.9]$$

where λ is the normalized capacitance in between the calibration values (0 is the capacitance measured for air and 1 the capacitance for oil). S is the normalized sensitivity matrix that produces normalized capacitance between 1 and 0. g is the normalized permittivity with limits defined by the permittivity of air and oil.

The inverse problem is ill-posed (Hadamard, 1923) since the inverse of *S* does not exist. Alternatively, a pseudo-inverse matrix can be computed. There are different ways to find a pseudo-inverse matrix. These include the singular value decomposition (Yan et al., 2004) and the Moore-Penrose method (Moore, 1920, Penrose, 1955). Another popular approach is to obtain the inverse problem matrix, which is achieved by regularisations methods. This include algorithms like the Linear Back Projection (LBP) and the Tickhonov regularisation (Yang and Peng, 2003). The permittivity using this method is calculated as:

$$\hat{g} = S^{-1}\ \lambda \qquad [4.10]$$

where, $\hat{g}$ is the calculated normalised permittivity and S^{-1} the matrix used to solve the inverse problem.

However, the $\hat{g}$ solution given by equation [4.10] does not satisfy the equation [4.9]. It does not fulfil the forward problem. To accomplish both the forward and the inverse problem an iteration process is exercised. The iterative steps correspond to the following equations: [4.11], [4.12], [4.13], and [4.14].

$$\lambda_2 = S\,\hat{g}_1 \qquad [4.11]$$

$$\Delta\lambda = \lambda_1 - \lambda_2 \qquad [4.12]$$

$$\Delta g = S^{-1}\Delta\lambda \qquad [4.13]$$

$$\hat{g}_2 = \hat{g}_1 + K\Delta g \qquad [4.14]$$

The iteration is repeated until Δg is smaller than a chosen value. K is a gain value; applied to speed up the convergence or to find and stable solution (K=1 normally performs well).

Figure 4.4 compares different reconstruction methods. There are five virtual permittivity distributions representing different liquid and gas developments. Capacitance values for these distributions were calculated by applying the direct problem relationship (Equation [4.9]). Subsequently, the permittivity distributions could be reconstructed by applying different algorithms including: Linear Back Projection, Singular Value Decomposition (SVD), and Tikhonov Regularization. The corresponding void fraction value for each image is noted underneath the images in the figure.

SVD and Tikhonov algorithms give better reconstruction results. Furthermore, Tikhonov method can filter the noise that appear during the capacitance acquisition.

This can be achieved by applying a coefficient; a high value reduces the noise but if it is too high it could mask the results.

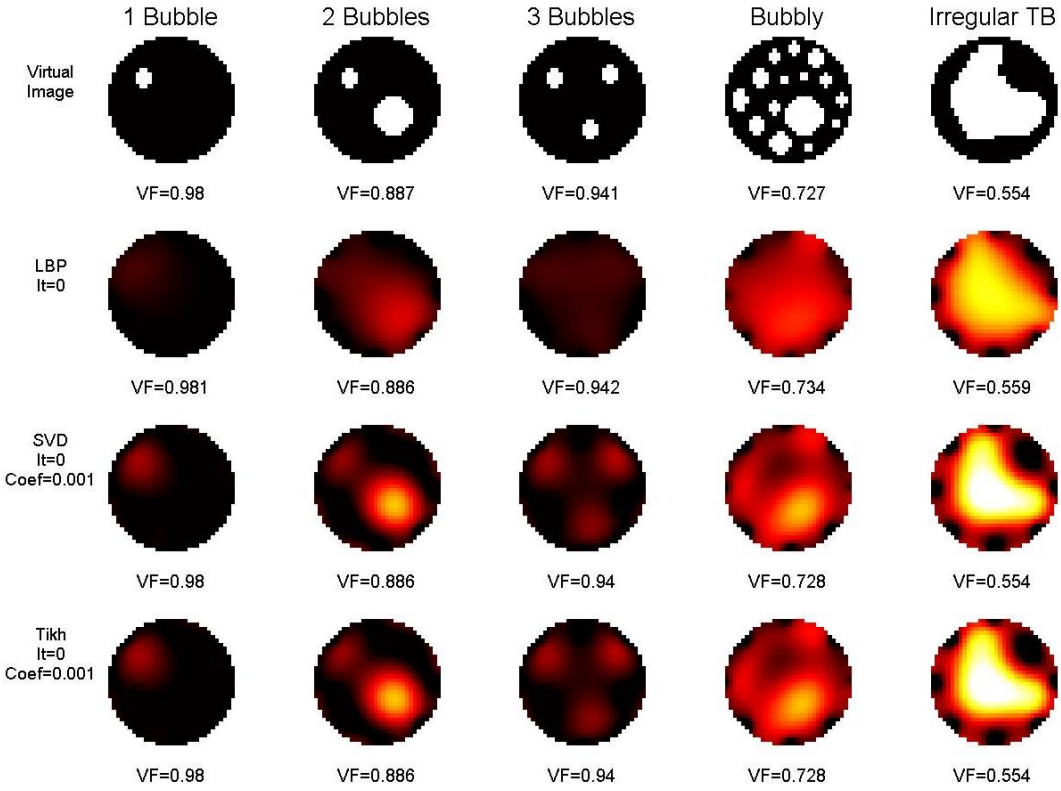


Figure 4.4. Reconstruction of virtual images with different algorithms: LBP, SVD and Tikh.

The reconstruction result is not mathematically exact, therefore not perfect employing any of the methods. It cannot capture small details, i.e: it is not possible to identity all the bubbles presented in the bubbly flow image. Also, the reconstruction next the wall seems to be unrealistic; i.e. the irregular Taylor bubble reconstruction shows air branches connecting the bubble to the wall. On the other hand, the algorithms can predict very well the overall void fraction in the pipe cross-section. It can be seen that the void fraction values (shown below each image) are very close to the void fraction of the virtual images for all the cases.

Figure 4.5 shows solutions obtained by different number of iterations applying Tikhonov algorithm. It can be easily seen that the quality of the reconstruction improves with the number of iterations. However, it requires more computational time.

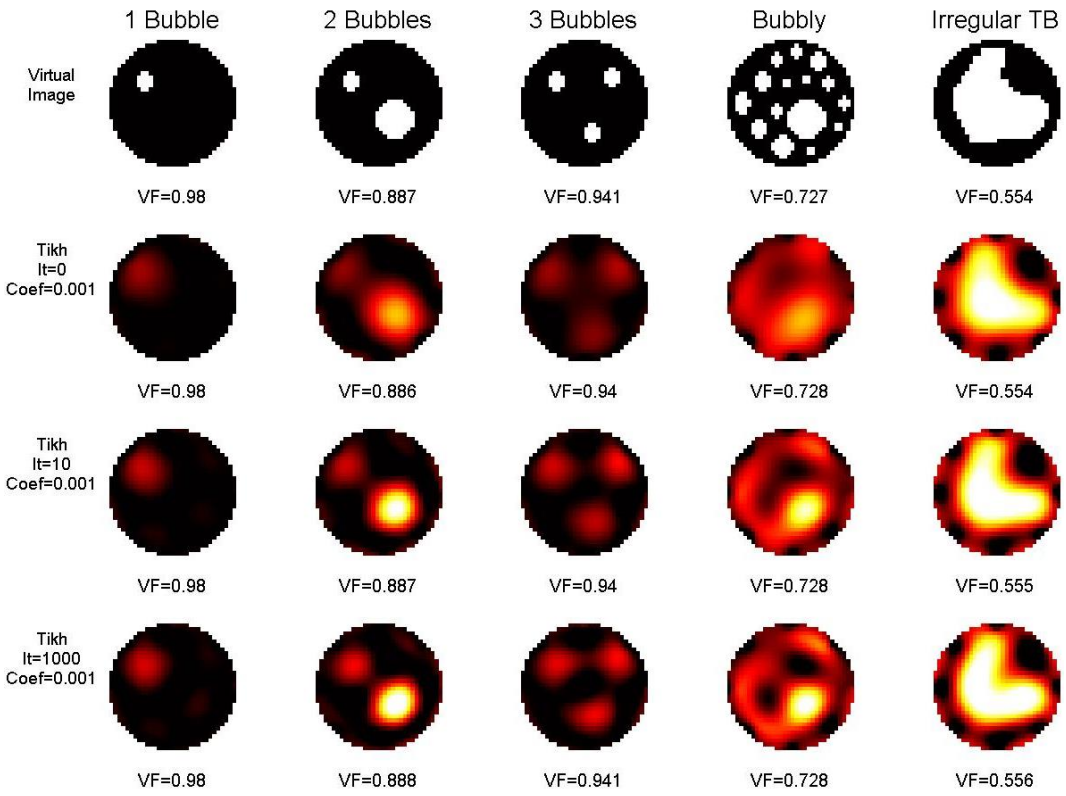


Figure 4.5. Reconstruction of virtual images with different number of iterations using Tikhonov regularisation.

Tikhonov algorithm with a coefficient equal to 0.01 and 50 iterations is chosen for reconstruction of the permittivity distribution in this thesis. It gives an acceptable reconstruction that does not seem to improve with increasing the number of iterations.

4.3 Void fraction cross-sectional distribution

Techniques based on measurement of the permittivity to calculate the void fraction pose a problem whereby the correlation between the permittivity and the void fraction is not always evident (Da Silva et al., 2011). Both ECT and WMS produce an image of a cross-section of the pipe divided into square cells. One value of permittivity is assigned

for the medium occupying each cell. Depending on how the two phases are distributed inside the cell the permittivity of that cell changes. In other words, different void fraction in a cell can produce the same permittivity.

The limits of this discrepancy are set by Wiener (Wiener, 1910) bounds which can be defined as the maximum and the minimum permittivity that a cell with a specific void fraction can give. The maximum is registered assuming that the two phases are stratified and located in parallel to the electric field lines. The minimum happens when the two phases are perpendicular to the electric field lines. These assumptions are illustrated in Figure 4.6. The first image on the left is a schematic of the real phase distribution inside one of the cells, the foils of the capacitor are represented by the rectangles in brown. The second image (middle) shows the air and the liquid in parallel to the electric field (maximum permittivity), and in the last one (right) shows the phases in series (minimum permittivity).



Figure 4.6. Real, parallel and series phase distribution in a cell.

Mathematically, the void fraction in the parallel model is calculated as an electric circuit with two capacitors in parallel,

$$\alpha = \frac{\varepsilon_l - \varepsilon_x}{\varepsilon_l - \varepsilon_g} \qquad [4.15]$$

where α is the void fraction and ε_l, ε_g, ε_x are the permittivities of the liquid, gas and mixture inside the cell.

In a similar way, the serial model is a circuit with the capacitors in series represented by the relationship below.

$$\alpha = \frac{\varepsilon_l - \varepsilon_x}{\varepsilon_l - \varepsilon_g} \cdot \frac{\varepsilon_g}{\varepsilon_x} \qquad [4.16]$$

Figure 4.7 shows the relation between the relative permittivity and the void fraction for the parallel and serial models considering silicon oil as the liquid phase whose relative permittivity is 2.7 and air as the gas phase. Air has a permittivity close to the vacuum, thus its relative permittivity is considered equal to 1.

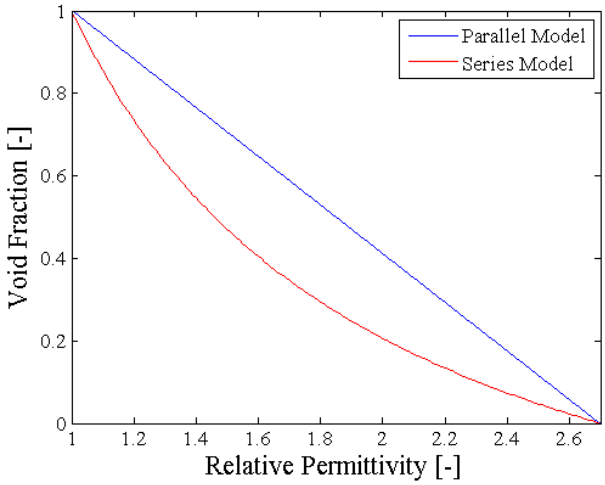


Figure 4.7. Real void fraction against relative permittivity for parallel and serial models.

From Figure 4.7, it can be seen that there is no divergence between the two models at the limits. Therefore, there is only one possible void fraction when the permittivity is maximum or minimum. In other words when the cell is completely filled by oil or by air both models produce the same result. However, when the permittivity is between the two limits,(Da Silva et al., 2011) the difference can be considerable. Therefore, the void fraction must be adjusted to one model or the other considering the expected flow distribution.

In the case of the WMS where the electrodes are wires perpendicular to the flow, the parallel model is considered more suitable because the gas-liquid interface is perpendicular to the wires in most of the cases (i.e. big bubbles or stratified flow). For the ECT sensor, the electrodes are positioned parallel to the flow and the electric field

lines depend on the position of the pair of electrodes that are measuring. For these reasons, there is no preference between the permittivity models for the ECT sensors.

Considering that the experiments are expected to produce slug, churn, and cap bubble flows, whereby the gas-liquid interface is mostly perpendicular to the electric field lines; in the case of the WMS the parallel model is chosen for the analysis of the data. Since no preference is clear for the ECT sensor; the same parallel model is chosen.

Other permittivity models in between Wiener bonds have been proposed (Peña et al., 2013, Da Silva et al., 2011). These include models for very specific conditions, for example: fluids with very different permittivity (water and air) or for the case of finely dispersed bubbly flow, which is not expected in the present work.

4.4 Diametrical time traces

A cross-sectional void fraction distribution frame is obtained in each acquisition. A diametrical time trace (DTT) is obtained by taking the values of void fraction along one diameter of cells for each frame and stack them in the order of their acquisition time. Figure 4.8 shows WMS and ECT DTTs for 400 acquisitions. As aforementioned, the WMS images have 24 cells whilst the ECT has 32 cells per diameter. Cells in black are filled with oil and cells in white are filled with air, the yellow-orange tones are a mixture of the two phases.

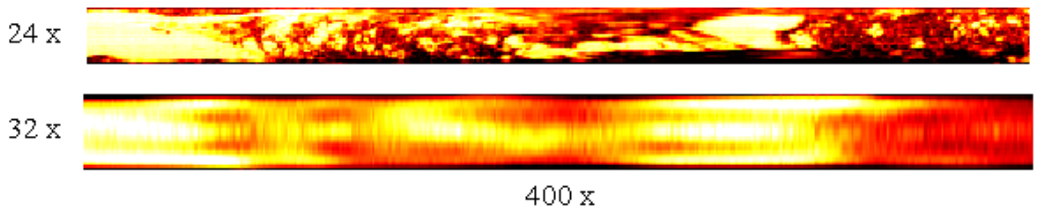


Figure 4.8. Diametrical time traces (400 acquisitions). The first image is WMS (24 cells in the diameter). The second image is from the ECT sensor (32 cells in the diameter).

DTT can give an idea of how the phases are distributed along the pipe. However, it must be clear that the y-axis represents time and not distance. Therefore, it is not possible to know how long the gas structures are just from the DTT. Nevertheless, if the gas structure velocity is known, the y-axis can be converted from time unit to equivalent length by multiplying by a coefficient. This coefficient (C_L) is expressed in equation [4.17]. This process will either expand or contract the DTT images depending on if the coefficient is greater or smaller than 1.

$$C_L = \frac{D \cdot U_s \cdot f}{N_c} \qquad [4.17]$$

where D is the pipe diameter, U_s is the gas structure velocity, f is the acquisition frequency and N_c is the number of cell in the diameter.

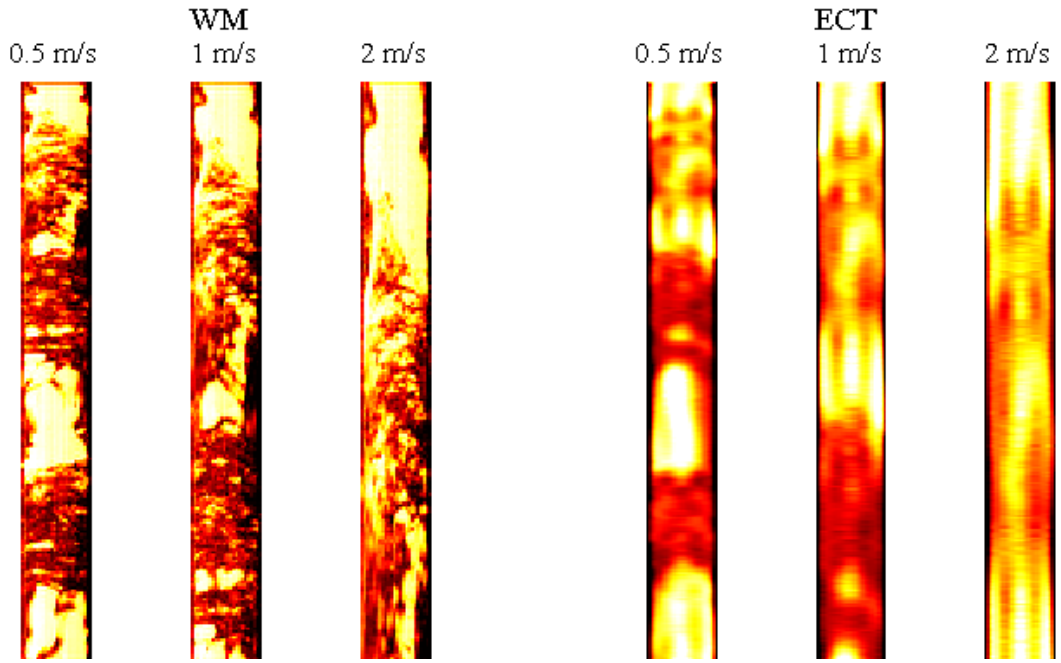


Figure 4.9. DTT modified to equivalent length for WM and ECT and Us equals to 0.5, 1 and 2 m/s.

Figure 4.9 shows the DTT modified by applying C_L calculated at different U_s. It can be seen that from the same DTT that gas structures look longer when U_s is higher.

4.5 Cross-sectional void fraction time series

Cross-sectionally averaged void fraction time series are normally referred to as void fraction time series. The cross-sectional void fraction is the void fraction surface integral traversing a cross section. It is calculated as the weighted average of the void fraction in the cross-section cells. It is expressed as x_t in equation [4.18], the subscript t is added to indicate that it is different for each frame obtained at time *t*.

$$x_t = \sum_{i=1}^{N_c} a_i \cdot \varepsilon_{i,t} \qquad [4.18]$$

where $\varepsilon_{i,t}$ is the void fraction in the cell *i* at the acquisition time *t*, N_c is the number of cells and a_i is the weight coefficient. This coefficient is the area of the cell divided by the area of the whole cross-section for WMS (Prasser et al., 2002). For the ECT, it is constant for all the cells whereby it is equal to $1/N_c$.

Figure 4.10 shows the void fraction time series and one DTT produced by the WMS. It can be seen that the high void fraction regions in the time series correspond to the presence of gas structures in the DTT. Similarly, low void fraction areas to liquid slugs.

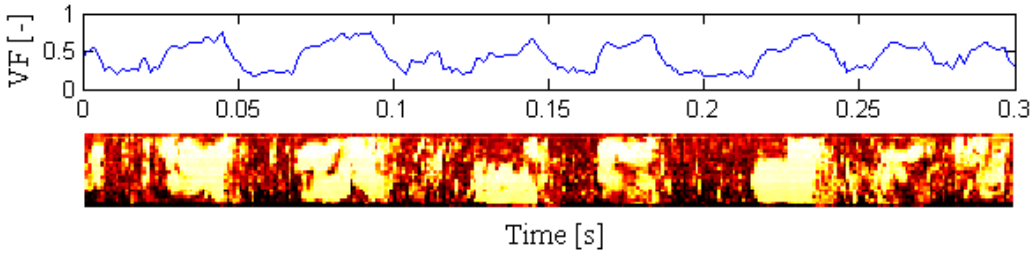


Figure 4.10. Void fraction time series and DTT for the same cross-section obtained over 0.3 seconds.

4.5.1 Statistical moments

Statistical treatment of the void fraction time series can be performed in order to obtain more representative single values. The most representative value is the mean, as it gives information about the overall void fraction, it can be calculated as

$$\bar{x} = \frac{1}{N} \sum_{t=1}^{N} x_t \qquad [4.19]$$

where *N* is the number of acquisitions.

In addition, the standard deviation is useful as well. It gives information about the dispersion of the data. Which can be an indicative of the flow intermittency. It is calculated as

$$\sigma = \sqrt{\frac{1}{N} \sum_{t=1}^{N} (x_t - \bar{x})^2} \qquad [4.20]$$

4.5.2 Probability density function

The Probability Density Functions (PDF) of the void fraction time series show the probability at which each void fraction value is expected to occur under specific flow conditions. They are useful to compare different void fraction time series and also to identify the flow regime (Costigan and Whalley, 1997).

Figure 4.11 shows three void fraction time series and their corresponding PDF. Looking at the PDF and recalling the Costigan and Walley criteria; the flow regime could be established as bubbly, slug and churn flow respectively.

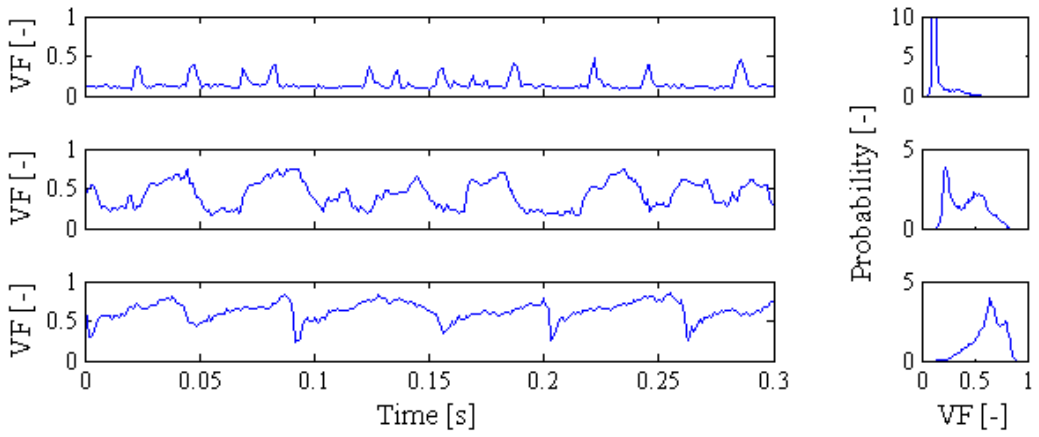


Figure 4.11. Three different void fraction time series and their corresponding PDF. They are identified as bubble, slug and churn flow.

4.6 Void fraction average radial distribution

Void fraction radial profiles can be calculated by dividing the cross-section into *m* concentric rings around the pipe centre. Then, average the void fraction inside each ring both spatially and temporally (Prasser et al., 2002). Mathematically it is expressed as

$$\overline{x_m} = \frac{1}{N} \sum_{t=1}^{N} \sum_{i=1}^{N_c} b_{i,m} \cdot \alpha_{i,t} \qquad [4.21]$$

where, $\overline{x_m}$ is the void fraction average in a *m* radial position, $b_{i,m}$ is a weight coefficient that is the cell area inside the ring divided by the ring area (Prasser et al., 2002).

This analysis can be carried out for both ECT and WMS data. Nonetheless, only the WMS data is analysed in this way; since the ECT spatial resolution is not good enough to give accurate void fraction radial profiles. Figure 4.12 shows three void fraction radial profiles corresponding to bubbly, slug, and churn flow. The position 0 on the x-axis is the centre of the pipe while 1 is the wall. The radius has been divided into 20 points (rings).

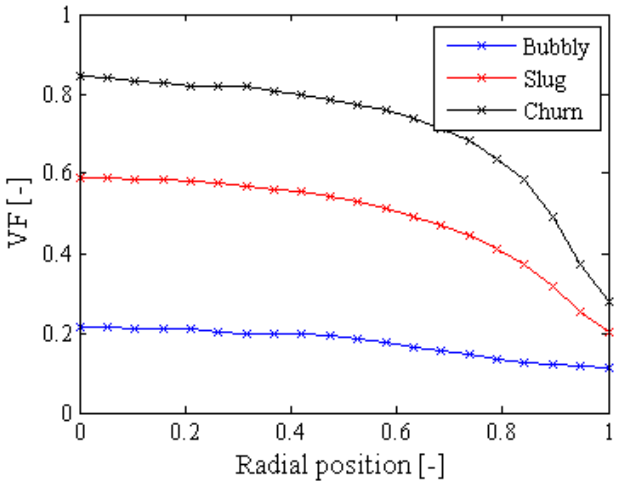


Figure 4.12. Void fraction radial profiles for three different flow regimes. 0 is the centre of the pipe and 1 is the wall.

4.7 Velocities of the gas structures

Taylor bubbles, big cap bubbles or any other gas structure in intermittent flows raises at a velocity U_b. The velocity of these structures can be measured using two ECT planes separated by a known distance. Figure 4.13 (a) represents the void fraction time series acquired by the two planes of a twin ECT sensor, the signals look similar but the ECT 1 is delayed by Δt seconds. In Figure 4.13 (b) ECT 1 signal is delayed by a time τ to obtain the best signal overlapping.

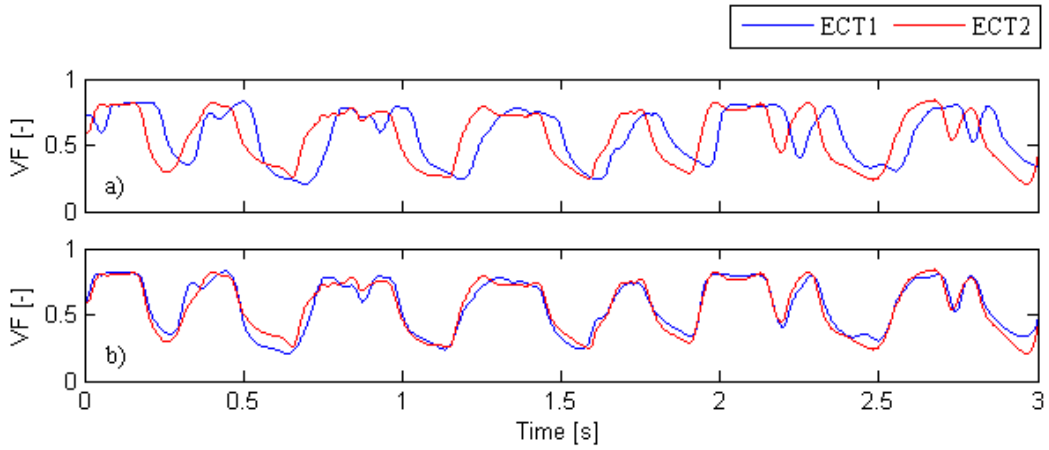


Figure 4.13. (a) Simultaneous ECT void fraction time series in two twin planes. (b) The second series are delayed to find the maximum cross-correlation.

The delay τ that achieves the overlap of the two signals is calculated as the delay that maximizes the cross-correlation between both ECT signals. The cross-correlation as a function of τ is calculated as:

$$R_{xy}(\tau) = \frac{E[(x_i - \bar{x})(y_{i+\tau} - \bar{y})]}{\sigma_x^2 \cdot \sigma_y^2} \quad [4.22]$$

where x_i and y_i are the void fraction time series from the two ECT planes and E is the expected value operator.

Once the τ which maximize R_{xy} is known, the structure velocity U_b can be calculated as:

$$U_b = \frac{d_p}{\tau \ (\max R_{xy})} \quad [4.23]$$

where d_p is the distance between the two planes of the ECT.

4.8 Identification of the gas structures

The gas structures can be identified by analysing the void fraction time series. The methods used revolve around determining when the structures start and finish crossing the measuring plane.

The simplest way is achieved by choosing a threshold of void fraction value. Afterwards, a gas structure is considered to start passing when the void fraction time series crosses the predefined threshold. It finishes passing when the void fraction falls below of the threshold again. This method has the inconvenience of that the threshold needs to be selected manually; resulting in the gas structures being cut unrealistically when their void fraction is close to the threshold.

Hazuku et al. (2008) proposed a method that solved these two problems. This is accomplished by applying two thresholds. The lower threshold is the mean of the void

fraction time series and the upper threshold is the mean of the values that are higher than the lower threshold (mean). Consequently, a gas structure is identified whenever the time series values rise above the upper threshold. However, the time of the structure is bounded by two points of the same peak crossing the lower threshold. Figure 4.13 shows the structures detected by these two methods for the same time series. The first graph by applying one threshold (set to 0.5) and second graph shows the structures detected with two thresholds applying Hazuku's method. The time series are accompanied by diametrical time trace at the bottom. The gas structures areas are indicated by a black shading of the void fraction time series. It can be seen that the first method cut some of the structures. On the contrary, this problem is resolved when applying the second method.

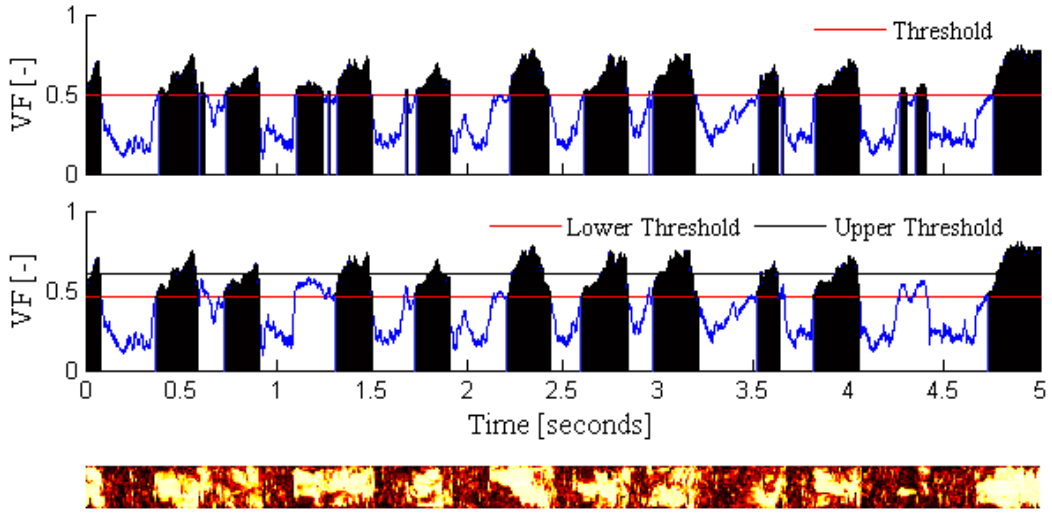


Figure 4.14. Gas structures identification using one and two thresholds compared with the DTT.

4.9 Frequency of the gas structures

Gas structure frequency is one of the main characteristics of the intermittent flows. It is defined as the number of gas structures passing through a fixed point of the pipe for a certain period of time. There are two ways to evaluate the gas structure frequency. One approach is achieved by calculating the mean frequency by counting the gas structures

and dividing it by the counting time. The other method is by computing the power spectral density (PSD) function of the void fraction time series and selecting the dominant frequency.

The gas structures can be counted visually or from the void fraction time series as explained in the previous section. Visual observation is supported by a physical evidence, but it depends on the perception of the observer. On the other hand, void fraction time series analysis is a repeatable methodology but it can miss or divide unrealistically some gas structures. To minimise this last problem, the median frequency can be considered instead of the mean frequency. Median frequency is calculated as the inverse of the median gas structure period:

$$f_b = \frac{1}{Me(T_n)} \qquad [4.24]$$

where, T_n is the period starting when the gas structure *n* is detected on the measuring plane and finishing when the following gas structure (*n+1*) is detected on the same plane.

The PSD function gives information about how the energy is distributed in the frequencies composing the signal. A discrete solution can be calculated as the squared module of the Discrete Fourier Transform of the void fraction time series as in

$$S_{xx}(f) = |DFT(x_i)|^2 \qquad [4.25]$$

The solution to equation [4.25] presents an uncertainty of 100 % because the DFT is an estimate of the Fourier Transform (Welch, 1967). However, this uncertainty can be reduced by applying averaging and overlapping methods. The problem of the uncertainty is that it can complicate the choice of the dominant frequency when there are several frequency peaks in the PSD. Furthermore, the dominant frequency of the void fraction time series might not correspond to the gas structure frequency. For this

reasons, the use of the PSD is only recommended when there is a single and clear dominant frequency in the signal.

Figure 4.15 (left) presents three samples of 0.2 seconds (taken from 1 minute void fraction time series) corresponding to different gas and liquid superficial velocities. In the middle, the PSD corresponding to the time series of the whole minute is plotted. On the right, the PSD produced by applying the Welch's method to smoothen the PSD and reduce the uncertainty can be seen. The averaging used in the Welch's method is for 8 samples, N=8. That reduces the uncertainty from 100% to 35% (uncertainty equals to $1/\sqrt{N}$ (Welch, 1967)). The overlapping applied is 50%. On the rightmost, the frequency values obtained by the method of peaks counting in the void fraction time series are displayed.

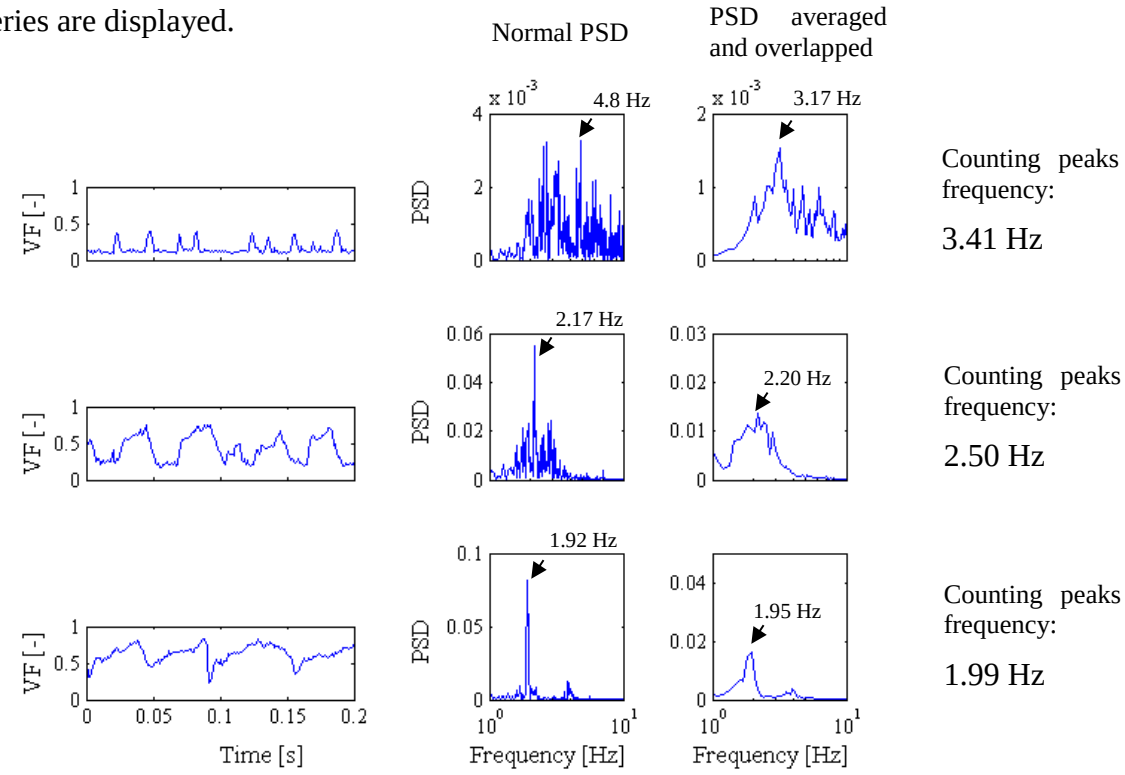


Figure 4.15. Three different samples of void fraction time series and their corresponding PSD, the PSD by applying averaging and overlapping, and the frequency obtained by counting peaks.

In Figure 4.15 above, the PSD (middle) of the void fraction time series on the top presents multiple dominant peaks. Therefore the frequency of the gas structures cannot be determined from this graph. Contrarily, looking at the PSD in which averaging and

overlapping methods are applied, it can be seen that it becomes clear that there is only a single dominant peak. However, the peak is quite narrow and the uncertainty is still 35%. Therefore, the dominant frequency still falls inside a wide interval. A similar problem appears in the void fraction time series presented in the middle row and its corresponding PSDs, the frequency of the gas structures cannot be satisfactorily determined from these graphs. On the other hand, in the third example on the bottom row, the dominant frequency appears to be very clear whereas the frequency of the gas structures can be obtained from the dominant frequency of the PSD without averaging. In the first and second example, the dominant frequency must by validated by the method of counting the peaks in the void fraction time series.

4.10 Bubbles detection and bubble size distribution

Individual bubbles can be identified from the WMS data. It is attained by a bubble core detection and filling algorithm developed by (Prasser et al., 2001). This algorithm scans over the 3D void fraction matrix and assigns an identification number to all the cells with a minimum amount of gas. The cells with the same number are part of the same bubble. The minimum bubble size that can be detected is limited by the wires spacing, which is 2.8 mm in the 67 mm diameter pipe and 3.9 mm in 127 mm diameter pipe, and the acquisition frequency, which is 1000 Hz at gas superficial velocities lower than 1 m/s and 4000 Hz at superficial velocities greater than 1 m/s.

This bubble detection is illustrated in Figure 4.16. In the figure, there are four DTT obtained at different gas and liquid flow conditions. Next to each DTT, there is a representation of the bubbles identified. Each bubble is painted in a different colour: pixels with the same colour are part of the same bubble. It can be seen as well that inside the same bubble the colour has tones from light to dark. The light colour is a high void

fraction and a dark colour means that the void fraction is low. When the colour is almost black, it means that the pixel is occupied mostly by liquid.

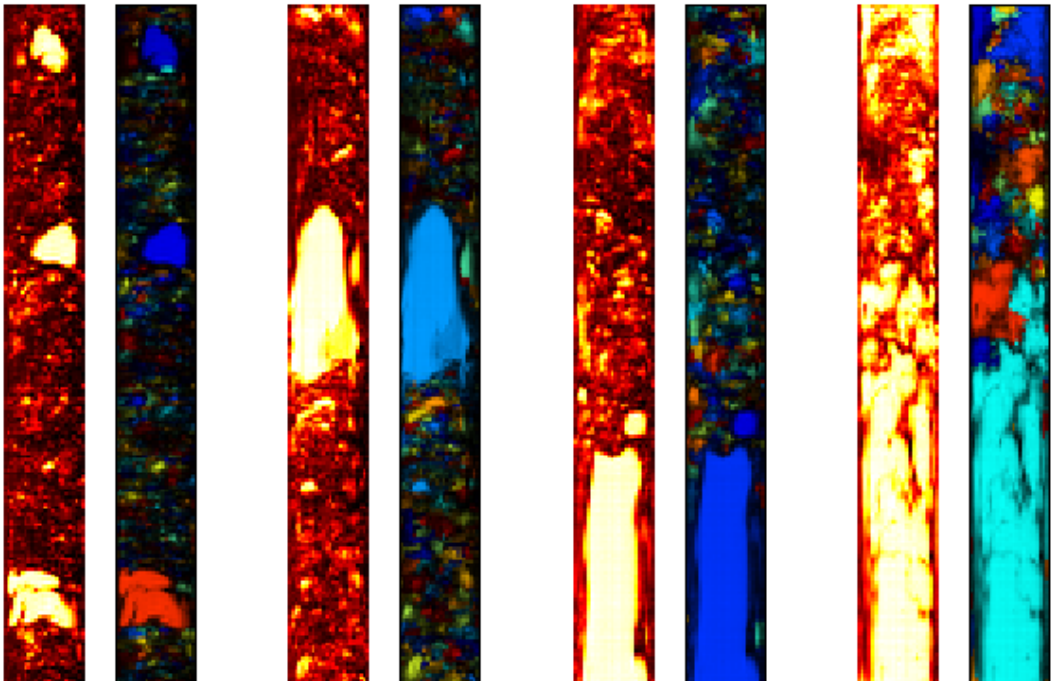


Figure 4.16. Four different samples showing identified bubbles represented in different colours.

Once all the cells corresponding to each bubble are identified, many information can be extracted: bubble starting point, bubble finishing point, bubble maximum equivalent diameter in the cross-sectional plane, etc.

The bubble maximum equivalent diameter in the cross-sectional plane $D_{XY,b}$ is the diameter of a circle that has the same area as the maximum area found in the XY plane of the bubble. It permits to know how much of the pipe cross-section is occupied by the bubble. Also, if the bubbles are considered spherical, the $D_{XY,b}$ diameter can be used as the diameter of the spherical bubble and the volume of the bubble can be calculated from it.

Additionally, if the velocity of the bubble is known, the bubble volume, bubble length and bubble equivalent diameter can be calculated as (Prasser et al., 2001):

$$V_b = p^2 \frac{U_b}{f} \sum_{n=1}^{N} \varepsilon_n \;\; ; n \in \text{bubble} \qquad [4.26]$$

$$L_b = U_b \cdot \left(z_{b,max} - z_{b,min}\right) \qquad [4.27]$$

$$D_{e,b} = \sqrt[3]{\frac{6\,V_b}{\pi}} \qquad [4.28]$$

where p is the wire spacing, f the acquisition frequency, U_b the bubble velocity, ε_n the void fraction in the pixel n that is part of the bubble b and N is the total number of pixels composing the bubble, $z_{b,max}$ is the time where the last pixel containing in the bubble b is located and $z_{b,min}$ is the time where the first pixel containing the bubble b is found.

With this information, it is possible to plot the number of bubbles of each size passing per unit of time. The size can be measured considering $D_{XY,b}$ or $D_{e,b}$. Figure 4.17 and Figure 4.18 show these distributions for different flow conditions using $D_{XY,b}$ and $D_{e,b}$.

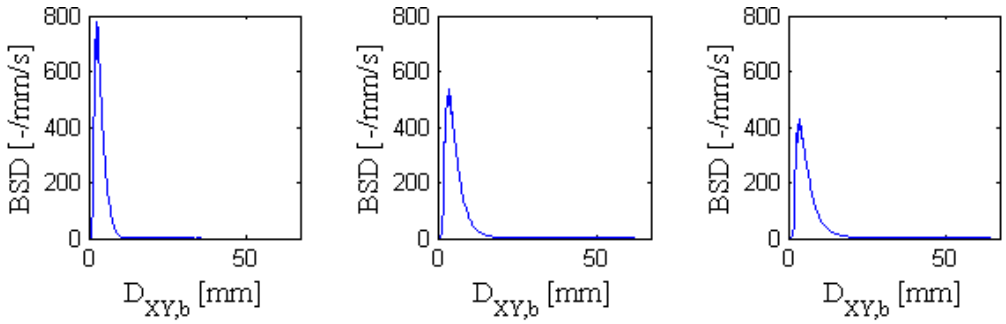


Figure 4.17. Number of bubbles of each size distribution considering $D_{XY,b}$

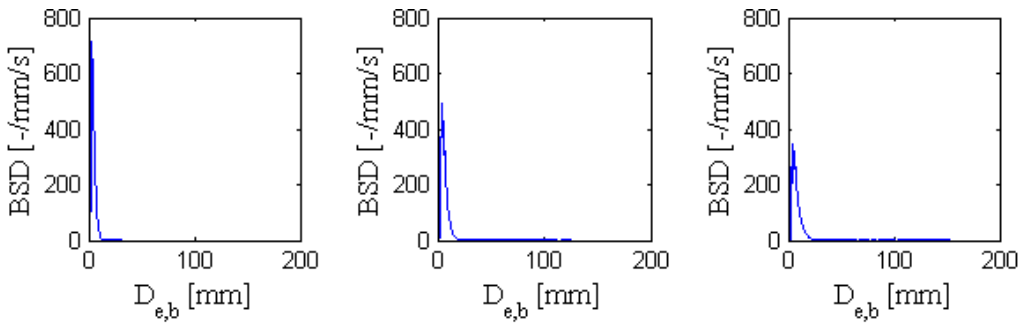


Figure 4.18. Number of bubbles of each size distribution considering $D_{e,b}$.

When $D_{XY,b}$is considered, the bubble diameter cannot be higher than the pipe diameter. It can be seen in Figure 4.17 that $D_{XY,b}$ it is always lower than 67 mm (diameter of the pipe). On the other hand, the diameter $D_{e,b}$ (in Figure 4.18) can be higher than the pipe diameter because the bubble does not need to be spherical and the bubble length can be larger than the diameter of the pipe. It can be seen in both figures that numerous bubbles having a diameter of only a few millimetres, whilst the big bubbles are very scarce compared to the small ones. Because of that, it is not possible to appreciate the big bubbles' distribution when they are plotted together with the small bubbles. Not even when using the logarithmic scale on the y-axis (as shown in Figure 4.9) adds any valuable information.

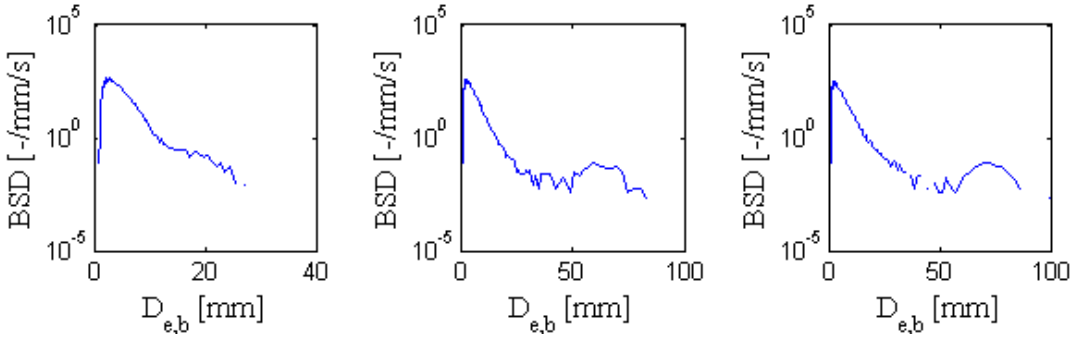


Figure 4.19. Number of bubbles of each size distribution in logarithmic scale considering $D_{e,b}$.

Clearer information can be obtained by plotting the contribution of bubbles of different sizes to the overall void fraction. The small bubbles have less gas volume whereas their number is substantial. On the other hand, the number of big bubbles is smaller whilst each bubble contains more air, posing higher contribution to void fraction. These distributions can be observed in Figure 4.20 and in Figure 4.21 considering the bubble size as $D_{XY,b}$ and $D_{e,b}$.

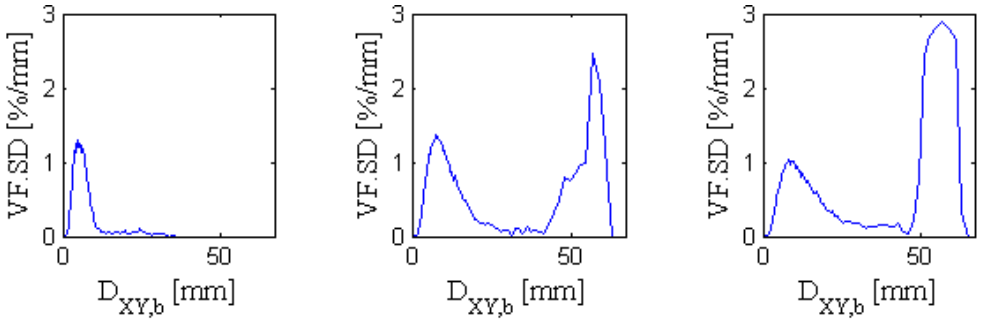


Figure 4.20. Void fraction of each bubble size distribution considering $D_{XY,b}$

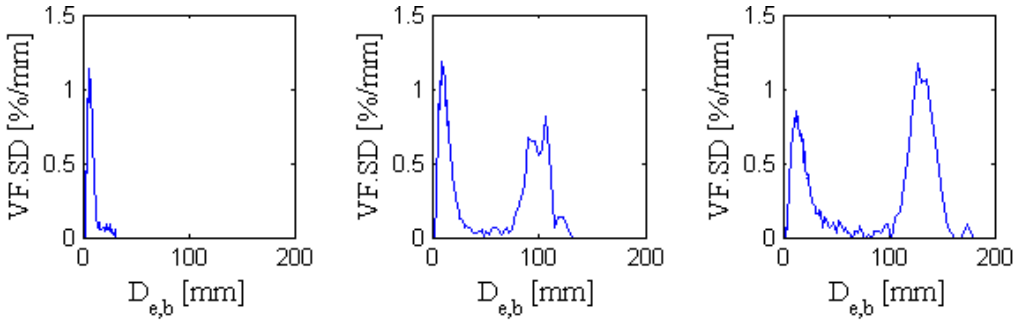


Figure 4.21. Void fraction of each bubble size distribution considering $D_{e,b}$.

4.11 Conclusions

WMS and ECT sensor output voltage signals that are registered in a computer at the selected acquisition frequency for a selected period of time. These voltage signals must be processed to extract relevant useful information about the two-phase flow behaviour that can be analysed.

The voltage values produced by both sensors are related to the capacitance between the electrodes of the sensors. These relationship are governed by the calibration of the sensors.

The calculation of the permittivity distribution in a cross-section of the pipe from the capacitance values measured between all the electrodes of the sensors presents an ill-posed problem. To find a solution to this problem some assumptions and mathematical approaches must be implemented such as discretization of the solution, parallel model of the permittivity, and Tikhonov regularisation in the case of the ECT.

The permittivity of a finite two-phase volume depends on the gas-liquid content, the permittivity of both components, and the spatial distribution of the phases inside the volume. When the volume is completely filled with liquid or gas it is a direct problem. But when it is occupied by both phases, a distribution model must be considered (series, parallel, etc.)

Both WMS and ECT sensor give at the end a 3D reconstruction of the two-phase flow. Two dimensions (*X* and *Y*) are the spatial coordinates of the planes where the sensors are installed. The third dimension (*Z*) is the time. Qualitative images and quantitative properties of the two-phase flow are extracted from these reconstructions, including: mean void fraction, gas structures velocity, frequency, and length etc.

CHAPTER 5.

THE INFLUENCE OF THE DIAMETER OF THE PIPE

5.1 Introduction

The gas and liquid dominated structures of the intermittent flow are very clear in vertical pipes of small diameter. Taylor bubbles followed by liquid slugs can be recognised directly through a transparent pipe. With increasing the pipe diameter, the intermittency is often not visible for the observer looking at a transparent pipe wall. What it is seen is an oscillating foamy film that masks the flow at the centre of the pipe. However, applying tomographic techniques enable the observation of flow behaviour in the entire cross-section whereby the intermittency of the flow can be visualised and thereafter analysed.

In this chapter, the influence of the diameter of the pipe on vertical intermittent flows is presented. Two-phase flow in two vertical pipes with 67 and 127 millimetres diameter was generated under different gas and liquid superficial velocities. The flow development is investigated from the reconstruction of the tomographic data acquired using the ECT and WMS. The tomographic reconstruction was carried out in order to identify and analyse the intermittency of the flow.

The velocity of the periodic structures was computed by cross-correlating the void fraction time series signals of the ECT sensor. Additionally, the gas structures were identified and their frequency evaluated by the methods described in Chapter 4. The results of the velocity and the frequency for 67 and 127 pipes diameter are presented and compared in this chapter. An equation to calculate the gas structure velocity as a function of the pipe diameter based on the drift-flux approach is formulated.

Furthermore, another correlation to calculate the frequency of the periodic structures is proposed. Both equations to predict the velocity and the frequency show an excellent agreement with the experimental data generated for both diameters of interest in this work.

5.2 Experimental arrangement

The experiments were performed in the 67 and 127 millimetres diameter rigs described earlier in Chapter 3. The fluids employed were silicone oil and air, their properties are detailed in Table 3.1. The same combination of gas and liquid superficial velocities were carried out in both facilities. The nominal values for the experimental matrix are presented in Table 5.1 whilst the real experimental values with their errors are detailed in Appendix B.

Table 5.1. Gas and liquid superficial velocities used in the experiments.

Liquid superficial velocities, U_{ls} [m/s]								
0.115	0.23	0.35	0.47					
Gas superficial velocities, U_{gs} [m/s]								
0.17	0.35	0.52	0.70	0.93	1.16	1.39	1.74	2.32

The experimental matrix consists of 9 different gas superficial velocities, each carried out at 4 liquid superficial velocities. That makes a total of 36 runs in each rig. The experimental matrix is plotted on Taitel et al. (1980) flow pattern map displayed in Figure 5.1. According to this map, it is expected to observe slug-churn flow for all the combinations of flow conditions investigated here. The only point out of the slug-churn area can be seen in the figure at high liquid superficial velocity and the lowest gas superficial velocity. In this run the expected flow regime is bubbly flow. However, this point is close to the transition boundary to slug flow; therefore, it is probably cap bubbly flow which is considered an intermittent flow regime.

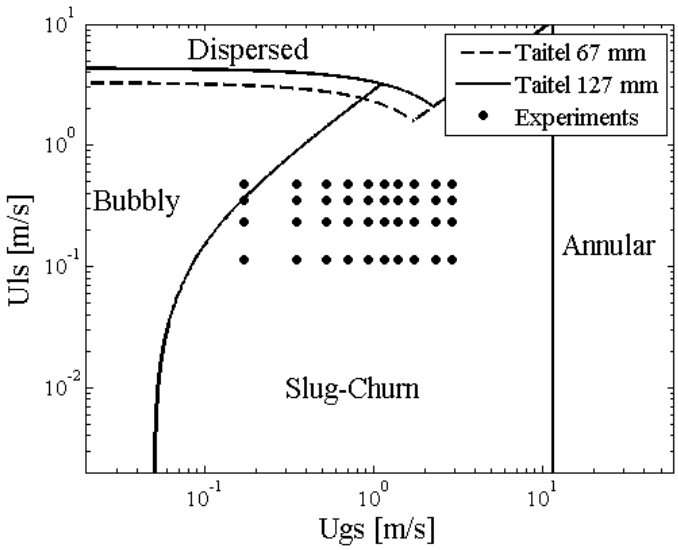


Figure 5.1. Experimental matrix plotted on Taitel et al. (1980) flow pattern map.

Data acquisition in both rigs for all flow conditions was carried out at a frequency of 1000 Hz over a period of one minute with both the ECT and WMS sensors. At gas superficial velocities greater than 1 m/s the acquisition frequency of the ECT was increased to 4000 Hz to enable the cross-correlation of the signals from both measuring planes of the ECT sensor.

5.3 Results

The results presented in this section were obtained after processing data from the ECT and the WMS. Methods used to analyse data were explained earlier on in Chapter 4.

5.3.1 Flow image reconstruction

Flow images were reconstructed using the diametrical time traces of the WMS and corrected using the velocity measured with the ECT as explained in Chapter 4.

Figure 5.2 depicts the flow reconstruction in both pipe diameters under the same flow conditions. Four examples are shown for different gas superficial velocities (U_{gs} =0.17, 0.7, 1.39 and 2.32 m/s) and a constant liquid superficial velocity (U_{ls} =0.35 m/s).

The intermittency is recognisable in all the images. However, in the 67 mm pipe the gas and liquid structures are better defined compare to their counterparts in the bigger pipe. The shape of the structures appears to differ as well whereas in the smaller diameter the gas structures are more regular, better defined, and separated by consistent liquid slugs.

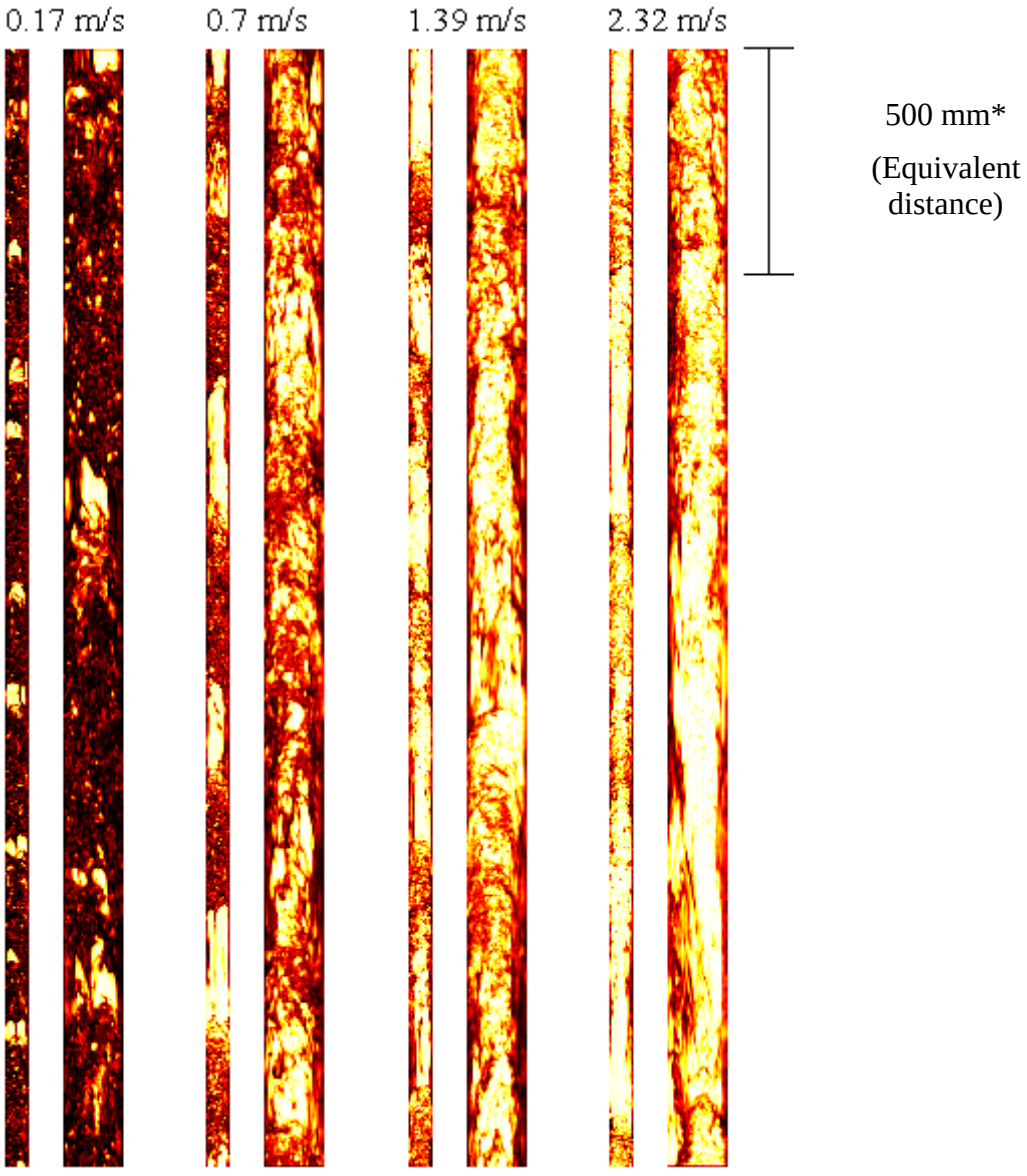


Figure 5.2. Flow reconstruction in 67 and 127 mm pipes and four different U_{gs}, U_{ls} = 0.35 m/s.

On the other hand, in larger diameter pipe, it becomes harder to appreciate the difference between the gas and liquid dominated structures. The gas structures are pockets of gas with very irregular interface around the gas core and with a considerable content of

liquid dispersed within them. Conversely, the liquid slugs are very aerated and inconsistent.

Figure 5.3 and Figure 5.4 illustrate reconstructions of the flow carried out in the same way as in Figure 5.2 but the axial scale has been multiplied by a factor that is 10 times the radial scale. In this way, more intermittent structures of the flow can be visualised. The liquid superficial velocity in Figure 5.3 is 0.115 m/s, and in Figure 5.4 is 0.47 m/s which is about four times higher. The intermittency appears much more appreciable in all the images except at the highest gas superficial velocity and lowest liquid superficial velocity in the 127 mm pipe.

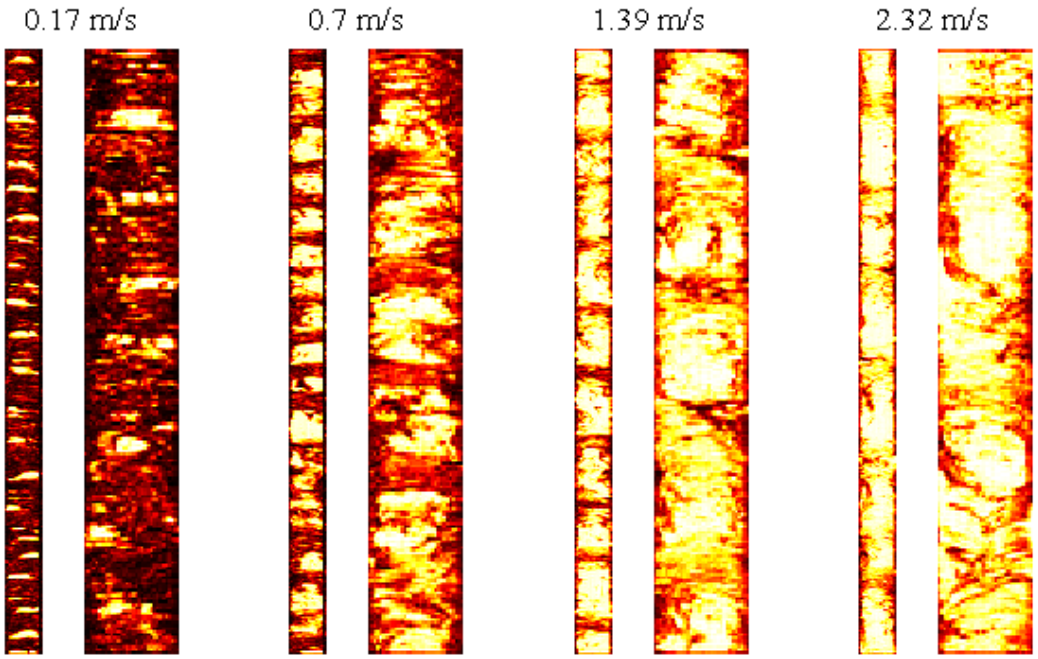


Figure 5.3. Flow reconstruction in 67 and 127 mm pipes and four different U_{gs}.
U_{ls} = 0.115 m/s. Axial scale = Radial scale x10.

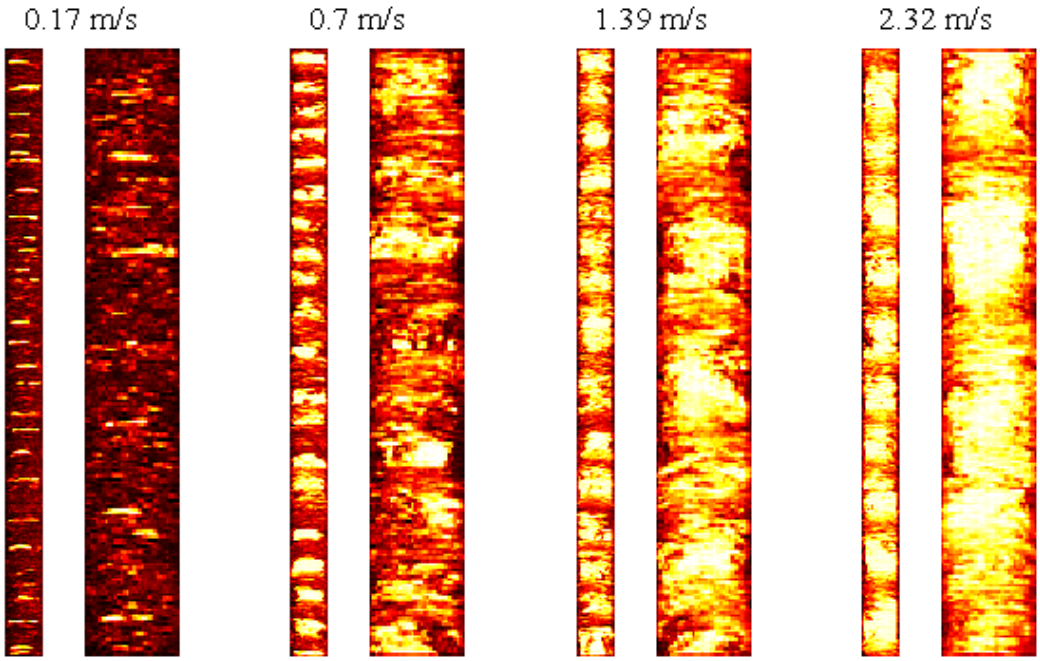


Figure 5.4. Flow reconstruction in 67 and 127 mm pipes and four different U_{gs}.
U_{ls} = 0.47 m/s. Axial scale = Radial scale x10.

It can also be seen that the length of both the gas and liquid structures increases considerably with increasing the diameter of the pipe. Moreover, the length can be observed to increase with increasing gas superficial velocity whilst it decreases with increasing liquid superficial velocity.

5.3.2 Velocity of the gas structures

The velocity of the gas structures was calculated by cross-correlating the void fraction time series signals from both planes of the ECT as explained in Chapter 4.

Figure 5.5 shows the values of the velocity of the gas structures for all the points in the experimental matrix. There are two graphs, one presents the values obtained from the 67 mm pipe, and the other shows the values from the 127 mm pipe. In each graph, the velocity of the gas structures (as identified using the method given in Chapter 4) is plotted against the gas superficial velocity (U_{gs}), the profiles are colour coded to the corresponding liquid superficial velocity (U_{ls}) displayed in the legend.

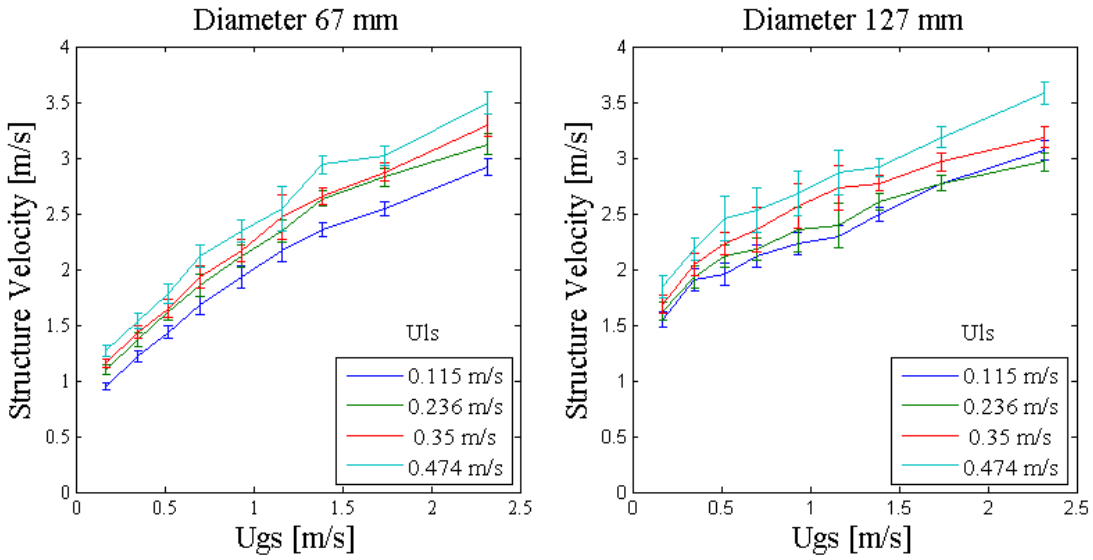


Figure 5.5. Velocity of the gas structures at different U_{gs} and U_{ls} and in the 67 and 127 mm diameter pipes.

It can be seen that the gas structure velocity increases with both the gas superficial velocity and the liquid superficial velocity regardless of the pipe diameter. That comes in agreement with the drift-flux model of Nicklin et al. (1962) that states that the structures velocity increases with the mixture velocity (gas superficial velocity plus liquid superficial velocity). Furthermore, it can be realised as well that at low U_{gs} the structure velocities are higher in the larger diameter pipe until they reach similar values when U_{gs} reaches high values. This comes in concordance with the work of Davies and Taylor (1950) which showed that the velocity of the Taylor bubble increases with the increase the diameter of the pipe. The error bars are also represented in the figure, they were calculated using the equation [5.1] which is explained in the Appendix.

$$\Delta U_b = \frac{1}{t}\Delta d + \frac{2d}{t^2}\Delta t \qquad [5.1]$$

Where ΔU_b is the error of the gas structure velocity, d is the distance between the planes of the ECT, Δd is the uncertainty of this distance (1 mm), t average time that gas

structures need to pass from one plane to the other of the ECT sensor, and Δt is the inverse of the data acquisition frequency.

The average error is 0.08 m/s for the 67 mm diameter pipe and 0.12 for the 127 mm diameter pipe. The exact value for each case is detailed in Appendix B.1.

5.3.3 Frequency of the gas structures

The frequency of the gas structures was measured using the methods described in Chapter 4. The frequencies were first calculated using the power spectral density (PSD) function in which an averaging of 8 samples was applied with an overlapping of 50%. That calculated frequencies carry an uncertainty of 18% from the PSD and a frequency resolution of 0.12 Hz. Looking at the PSD, if there is a clear dominant frequency peak, the corresponding frequency will be chosen as the frequency of the gas structures. However, if there is more than one dominant frequency from the PSD, the frequency value will be cross-checked with the frequency obtained by counting peaks in the void fraction time series. The peaks counting method was applied using the two thresholds method of (Hazuku et al., 2008). The aforementioned method has been applied to the 67 mm diameter rig and the experiments with gas superficial velocity higher than 0.7 m/s in the 127 mm diameter rig. In all the other cases, i.e. experiments with lower gas superficial velocity than 0.7 m/s in the 127 mm diameter, the peaks were counted manually from the void fraction time series and the diametrical time traces. That was executed in this manner because the mean void fraction was not constant preventing the thresholds not be determined. The results of the frequency for all the experiments are presented in Figure 5.6. The error bars are also featured in the figure which have a value equals to the frequency resolution of the PSD in which an averaging method of 8 samples is applied. That is calculated as:

$$\Delta f = \frac{F}{M} = \frac{1000\ Hz}{2^{13}} = 0.122\ Hz \qquad [5.2]$$

where ∂f is the frequency resolution of the PSD, F is the acquisition frequency an M is the size of each sample.

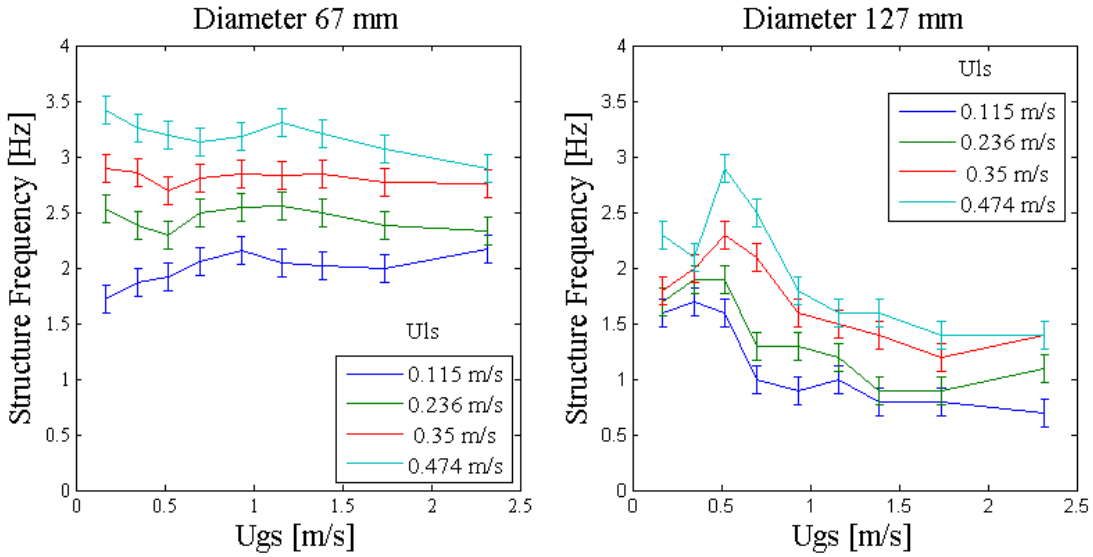


Figure 5.6. Gas structures frequency at different U_{gs} and U_{ls} in the 67 and 127 mm diameter pipes.

It can be seen that the frequency always increases with the increase of liquid superficial velocity. It can also be observed that it is always higher in the 67 mm pipe diameter compared to that in the 127 mm diameter at equal liquid and gas superficial velocities. With the increase of the gas superficial velocity, the frequency appears to be insensitive to increase in gas velocity anymore in the 67 mm diameter pipe. On the other hand, it decreases in the 127 mm diameter pipe until it nearly plateaus when the gas superficial velocity reaches around 0.7 m/s.

With increasing liquid superficial velocity the frequency is observed to become higher. This can be attributed to the increase in the velocity of gas structures with liquid velocity increase as manifested earlier in this chapter. Therefore, resulting in more gas structures passing through the pipe thus the frequency increases. On the other hand, with increasing gas superficial velocity or the pipe diameter, the gas structures become

bigger (both in diameter and length) as depicted in Figure 5.3 and Figure 5.4. This leads to bigger but lower number of gas structures passing through the pipe and therefore the frequency of the gas structures decreases.

5.4 Discussion

5.4.1 Velocity of the gas structures

The results of the velocity of the gas structures under all the experimental conditions considered are plotted in Figure 5.5. These results are adjusted to a Nicklin form (equation [2.23]) by least squares method. The values of the distribution coefficient C_o and the drift velocity, V_d, that best fit the results for each pipe diameter are shown in Table 3.1. The Froude number (Fr) considering the drift velocity and the determination coefficient R^2 are also presented.

Table 5.2. C_o, V_d, Fr and R^2 obtained for the 67 and 127 mm pipe results.

Diameter	C_o	V_d [m/s]	$Fr = V_d/\sqrt{Dg}$	R^2
67	0.983	0.833	0.810	0.962
127	0.678	1.551	1.115	0.921

The fitting is good in the case of the 67 mm diameter ($R^2 = 0.962$) but poorer in the 127 mm diameter pipe ($R^2 = 0.921$). Furthermore, the C_o coefficient and the Froude number are different in either diameter of the pipe. These results are also shown graphically in Figure 5.7 where the velocity of the gas structures is plotted against the mixture velocity. It can be seen that the results can be collapsed to a straight line presenting an equation in the form of model of Nicklin et al. (1962). However, the fitting is not good and can be further improved.

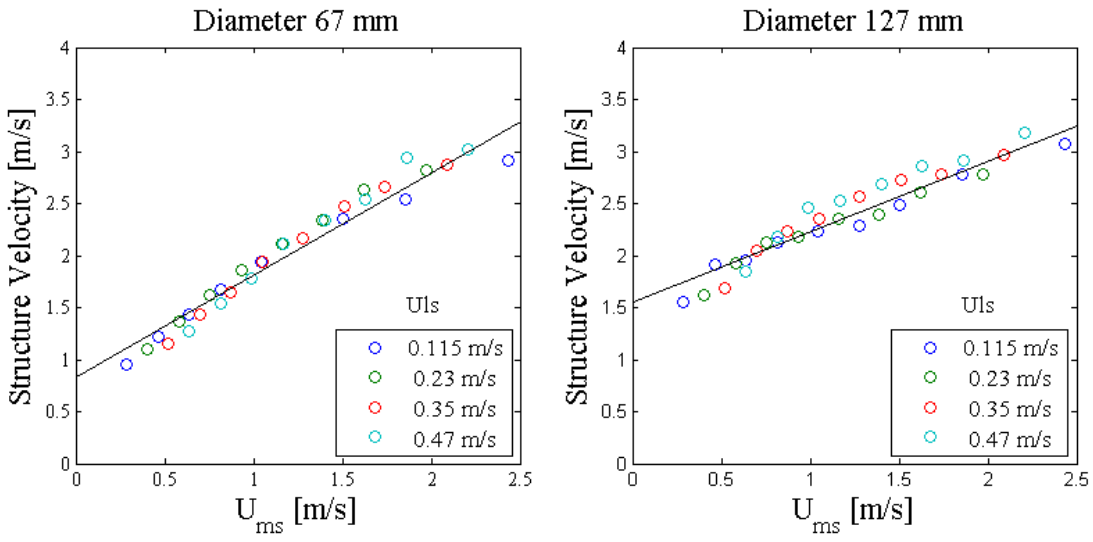


Figure 5.7. Gas structure velocities in the 67 and 127 mm diameter pipes plotted against the mixture velocity and the fitting curves of the form of Nicklin et al. (1962).

Data from both the 67 and the 127 mm diameter pipes can be fitted to a single equation, whereby the drift velocity can be calculated as a function of the diameter of the pipe in the way suggested by Dumitrescu (1943) and Davies and Taylor (1950) (equation [2.26]). The coefficient C_0 and the Fr that give the best fitting with the experimental results are detailed in Table 5.3.

Table 5.3. C_o, Fr and R^2 considering both diameters.

Diameter	C_0	$Fr = V_d/\sqrt{Dg}$	R^2
67 and 127	0.861	1.201	0.931

The resultant equation is:

$$V_b = 0.86\, U_{ms} + 1.2\sqrt{Dg} \qquad [5.3]$$

The fitting of this equation with the experimental data is acceptable ($R^2 = 0.931$). The experimental values are plotted against the predicted values using the equation [5.3] in Figure 5.8. It can be seen that the divergence is never higher than 20% for any of the flow conditions for both pipe diameters.

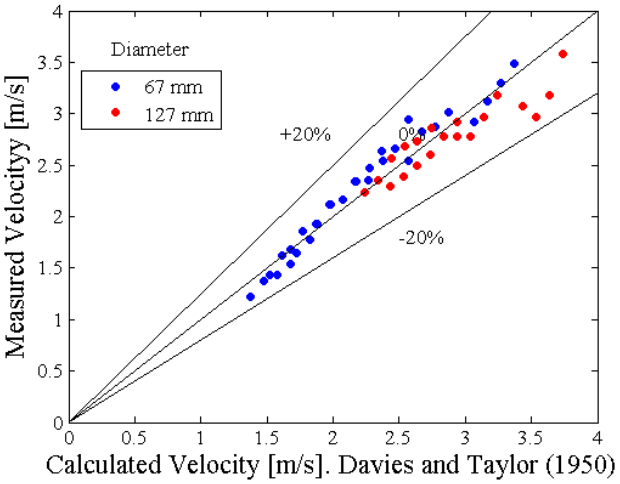


Figure 5.8. Comparison of the gas velocity obtained experimentally against the values calculated using an equation of the form of Nicklin et al. (1962) and the drift velocity of Davies and Taylor (1950).

The fitting can be improved if the distribution coefficient C_0 is not considered constant but rather dependent on the Reynolds number of the liquid moving at the mixture velocity U_{ms}. C_0, the distribution coefficient is the ratio between the flow velocity at the centre of the pipe to the mean velocity across the entirety of the pipe cross-section. This value is equal to 2 for laminar flow and decreases with increasing Reynold number toward values close to 1. That happens because the velocity profile is a parabolic function in laminar flow and it flattens with increasing Reynolds numbers (Zuber and Findlay, 1965). To show this effect, the distribution coefficient C_0 can be written as an expression of the form:

$$C_0 = C\, Re_l^{-n} \qquad [5.4]$$

Fitting parameters considering Davies and Taylor (1950) equation [2.26] and the formula in [5.4] for the distribution coefficient C_0 are shown in Table 5.4. The adjustment is better but the improvement is not remarkable (R^2 changes from 0.931 to 0.943).

Table 5.4. Parameter of C_o and Froude number.

Diameter	C	n	$Fr = V_d/\sqrt{Dg}$	R^2
67 and 127	2.786	-0.109	1.121	0.943

It must be noted that in this approach the diameter of the pipe has a dual counteracting effects on the velocity of the gas structure. Firstly, it has an influence on the Reynolds number; meaning that larger diameter yields a lower C_0 at the same U_{ls}. Secondly, it is related to the Froude number; whereas if the diameter is larger the drift velocity becomes higher.

Davies and Taylor proposed equation [2.26] based on theoretical developments as well as experiments. Their experiment consisted of a vertical pipe filled with water with a tap at the bottom. They opened the tap releasing some water and at the same time introducing some air into the pipe that produces a Taylor bubble. Then they measured the velocity of that bubble. There are three main differences between the experiments of Davies and the experiments presented here. Firstly, in the present experiments, the air is introduced without releasing any water. Secondly, the mean velocity of a train of bubbles is measured instead of the velocity of a single bubble measured by Davies and Taylor (1950). Finally, Davies and Taylor (1950) used water in their experiments as opposed to silicone oil in the present experiments.

Considering the differences between the experiments of Davies and Taylor as well as that C_0 coefficient is a function of the Reynolds number, the dependence of the drift velocity on the square root of the pipe diameter must be reviewed.

The forces acting on a Taylor bubble or any gas structure are the buoyancy and the friction with the liquid phase. The force balance can be written as:

$$\forall_b g\,(\rho_l - \rho_g) = C_d\, A_p V_d^2 \qquad [5.5]$$

where $\forall_b$ is the volume of the Taylor bubbles, C_d is the drag coefficient, $A_p$is projected area, g is the acceleration of the gravity, ρ_l and $\rho_g$are de densities of the liquid and gas phase.

Rearranging equation [5.5], the drift velocity can be expressed as:

$$V_d = \sqrt{\frac{\forall_b g\,(\rho_l - \rho_g)}{C_d\,A_p}} \qquad [5.6]$$

The volume of the Taylor bubble $\forall_b$ and the projected area A_p increase with increasing the pipe diameter as elucidated earlier in Figures 5.2, 5.3 and 5.4. The drag coefficient C_d depends on the Reynolds number which represents the resistance against the bubble movement through the liquid. Lower resistance gives lower drag coefficient. This resistance is related to the amount of gas in the liquid slug. It has been manifested earlier in Figures 5.2, 5.3 and 5.4 that the amount of gas increases with increasing pipe diameter. As mentioned earlier, it occurs because the liquid slugs in large pipes are not consistent and the interface is very unstable whereby the air can penetrate easily into the slugs. Thus, it is expected that the drift velocity increases with increasing the diameter of the pipe and a relationship of the form of the expression [5.7] is expected.

$$V_d = V_o \left(\frac{D}{D_o}\right)^m \qquad [5.7]$$

The diameter of the pipe D is divided by a reference diameter D_0 to dimensionless the distance. Since the units are in the international system (SI), to simplify the equation $D_o = 1$ meter will be used. On the other hand, V_o is the reference drift velocity, or in other words, the drift velocity in a pipe of a diameter equal to D_o.

The experimental results of the velocity of the gas structures for both pipe diameters were fitted to an equation of the form of Nicklin (equation [2.26]). The C_0 coefficient

is expressed as a function of the Reynolds number and the drift velocity as a function of the diameter of the pipe as shown in equations [5.4] and [5.7]. The parameters used in the fitting are shown in Table 5.5. The reference drift velocity V_0 (drift velocity in a pipe of a diameter equal to D_0) is unknown but can be calculated as a fitting parameter of the data.

Table 5.5. Fitting parameter C, n, V_0 and m and the determination coefficient R^2.

Diameter	C	n	V_0 [m s^{-1}]	m	R^2
67 and 127	13.63	-0.250	8.82	1	0.960

The coefficient of determination is good (R^2 = 0.96). The correlation proposed to calculate the velocity of the gas structures as a function of the diameter of the pipe is presented in equation [5.8]. In this equation, the terms m, D_0 and V_0 are combined together as a constant $a = V_0/D_0^m = 8.82$ that has a dimension of s^{-1}. On the other hand, the distribution coefficient C_0 is calculated using equation [5.9].

$$V_b = C_0 U_{ms} + 8.82D \quad [5.8]$$

$$C_0 = 13.63\, Re_l^{-0.25} \quad [5.9]$$

Figure 5.9 compares experimental gas structure velocities with those calculated using the correlation [5.8] for both pipe diameters at all the gas and liquid superficial velocities considered in this research. It can be seen that the agreement is very good and the difference does not normally exceed 10 %.

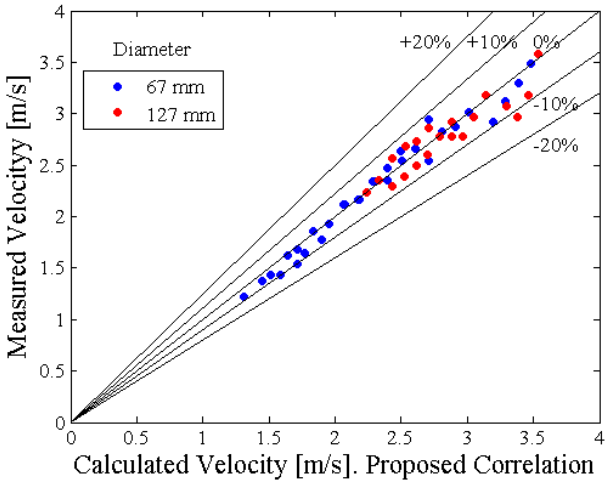


Figure 5.9. Comparison of the experimental values of the gas structure velocities with the calculated results using the proposed correlation [5.8].

In Figure 5.10 the experimental results are plotted together with the correlation function profiles [5.8] against the gas superficial velocity at different liquid superficial velocities. It can be seen that the experimental velocity of the gas structures is higher in the 127 mm diameter than in the 67 mm diameter at low gas superficial velocities. But this difference reduces with increasing the gas superficial velocity.

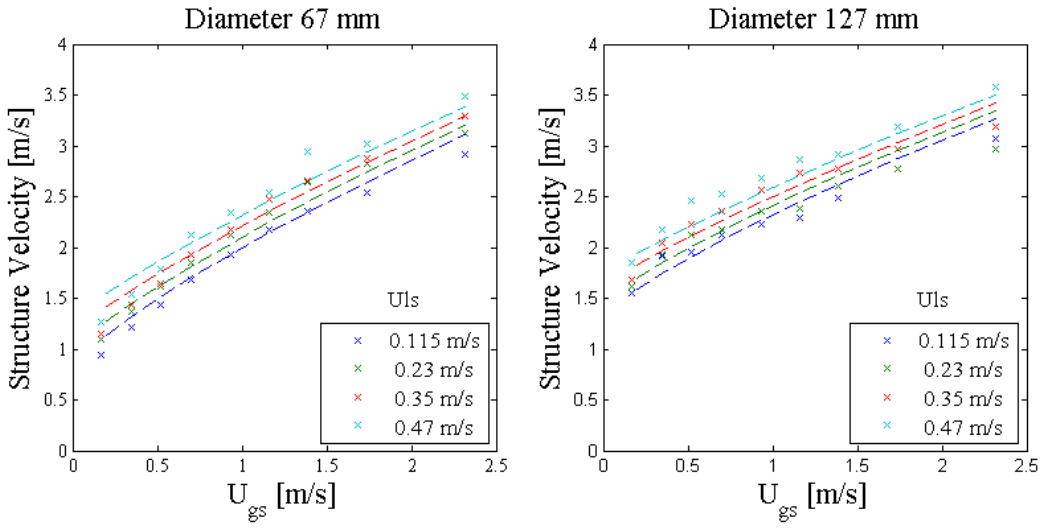


Figure 5.10. Comparison of the experimental values of the gas structures velocities with the correlation function [5.8] at different U_{gs} and U_{ls} in both pipe diameters.

5.4.2 Gas structures frequency

The results of the frequency presented in section 5.3.2 are further discussed and analysed in this section. They are compared with popular correlations published in the literature. Since no good agreement with the present data is obtained, because the models are mainly developed for horizontal flows and small pipe diameters; a new correlation that fits better with the present experimental data is proposed.

The results of the frequency, expressed as a Strouhal number based on the gas superficial velocity, is plotted against the liquid volumetric fraction (equation [2.36]) in Figure 5.11. Fossa et al. (2003) correlated these two parameters using equation [2.37]. They employed their own frequency data as well as data from other works for horizontal flows whereas they obtained a good agreement. The same equation proposed by Fossa et al., but with the parameters A, B and C adjusted to the present data in vertical flow, is applied. The fitting parameters and the fitting coefficient are shown in Table 5.6

Table 5.6. Fitting parameter A, B and C obtained adjusting the present data to the equation of Fossa et al. (2003) and the determination coefficient R^2.

Diameter	A	B	C	R^2
67 and 127	0.612	-1.042	0.169	0.920

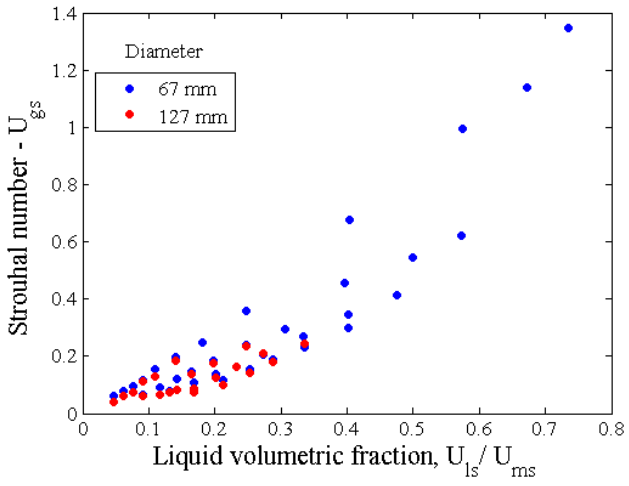


Figure 5.11. Strouhal number based on U_{gs} plotted against the liquid volumetric fraction for all the U_{ls} and U_{gs} executed in the experiments of this chapter and for both pipe diameters.

The second group of correlations are formed between the Strouhal number and the Lockhart-Martinelli parameter. The Lockart-Martinelli parameter is a dimensionless number used to calculate the heat transfer in two-phase flows. It is calculated from the relationship presented in equation [2.35] but can be simplified to:

$$\chi = \frac{U_{ls}}{U_{gs}}\sqrt{\frac{\rho_l}{\rho_g}} \qquad [5.10]$$

Figure 5.12 compares the Lockhart-Martinelli parameter calculated using Darcy-Weisbach equation and the Colebrook-White friction factor (f) for turbulent flow and $f = 64/Re$ for laminar flow against the simplified Lockhart-Martinelli parameter (equation [5.10]). It can be seen that the values obtained using both equations do not show significant differences, the difference is only considerable at high Lockhart-Martinelli parameter values when the friction factor of the two phases becomes very different (that is meanly at high U_{ls} and low U_{gs}) in the 67 mm diameter pipe. This disparity occurs because the simplified Lockhart-Martinelli parameter does not consider whether the flow is turbulent or laminar whilst the original formula for Lockhart-Martinelli parameter does.

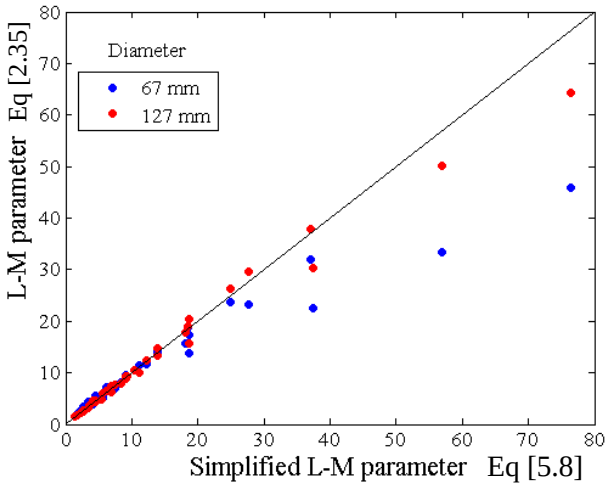


Figure 5.12. Lockhart-Martinelli parameter calculated using expression [2.35] compared with the simplified version calculated with equation [5.10] at different U_{gs} and U_{ls} and different diameters.

The Strouhal number is a dimensionless number describing the oscillations in a flow. It is calculated using equation [2.34]. The equation considers the velocity of the flow that induces the oscillations. In the case of multiphase flows, there are several flow velocities that can potentially cause of these oscillations; the gas superficial velocity, liquid superficial velocity, mixture velocity, and structure velocity.

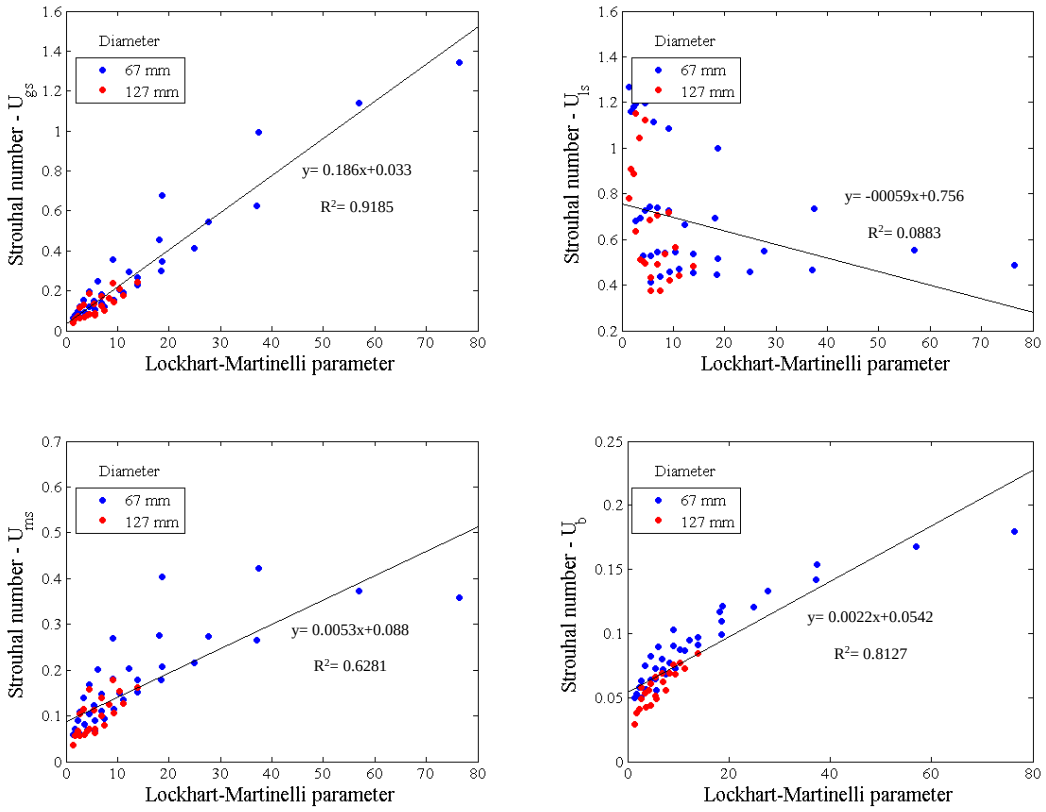


Figure 5.13. Strouhal number calculated using U_{gs}, U_{ls}, U_{ms} and U_b plotted against Lockhart-Martinelli parameter and its regression line and the determination coefficient (R^2) of each fit.

In Figure 5.13, the four different Strouhal numbers calculated using the aforementioned four different flow velocities are plotted against Lockhart-Martinelli parameter each in a separate sub-figure. The figure also includes the regression line and the determination coefficient for each fit. The Strouhal number that best correlates with the Lockhart-Martinelli parameter is the one calculated using the gas superficial velocity because it has the R^2 closer to 1. Additionally, its regression line passes closer to the origin. From this observation, it can be deduced that the phase responsible of the oscillations is the

gas flow and the velocity to be used for the calculation should therefore be the gas superficial velocity.

The Strouhal number calculated using the gas superficial velocity can be related to the simplified Lockhart-Martinelli parameter in the fashion shown in equation [5.11]. The parameter A that fits better with the experimental results and also the determination coefficient R^2 appear in Table 5.7. The agreement is low ($R^2 = 0.909$).

$$St = \mathrm{A}\,\frac{U_{ls}}{U_{gs}}\sqrt{\frac{\rho_l}{\rho_g}} \qquad [5.11]$$

Table 5.7. *A* parameter that gives the best fitting to equation [5.11] and the resultant determination coefficient.

Diameter	A	R^2
67 and 127	0.0198	0.909

Looking at this poor agreement, the significance of the Lockhart-Martinelli parameter in vertical pipes should be revisited. This parameter represents the ratio of the frictional pressure drop that would result in the liquid and the gas if both phases flowed separately as a single phase in the pipe and is expressed in equation [2.35]. At low liquid superficial velocities and high gas superficial velocities, the frequency of the gas structures would tend to equal zero as per equation [5.11]. That could be true for horizontal pipes where the liquid in the pipe is drained out of the pipe by the gas flow, whereby the liquid is only transported by entrainment in the gas. But in vertical pipes, some of the liquid cannot be drained by the gas because the action of the gravity keeps the liquid at the bottom of the pipe, even when the liquid superficial velocity is zero. To represent this effect in vertical pipes a fictional velocity B is added to the liquid superficial velocity in equation [5.11]. The velocity B must be dependent on the inclination angle of the

pipe. It should also equal zero in horizontal pipes, however the inclination angle effect will be deliberated in the next chapter. The resultant equation is:

$$St = \mathrm{A}\,\frac{(U_{ls} + B)}{U_{gs}}\sqrt{\frac{\rho_l}{\rho_g}} \qquad [5.12]$$

The coefficients A and B of the equation [5.12] that fit better with the experimental results for both diameters appear in Table 5.8. The agreement using these coefficients is excellent (R^2 = 0.990). The Strouhal number based on the gas superficial velocity is plotted against the modified Lockhart-Martinelli parameter in Figure 5.12. It can be seen that they correlate very well resulting in a straight line.

Table 5.8. A and B parameters in equation [5.12] that give better fitting with the data and the determination coefficient R^2.

Diameter	A	B [m/s]	R^2
67 and 127	7.431 E-3	0.534	0.990

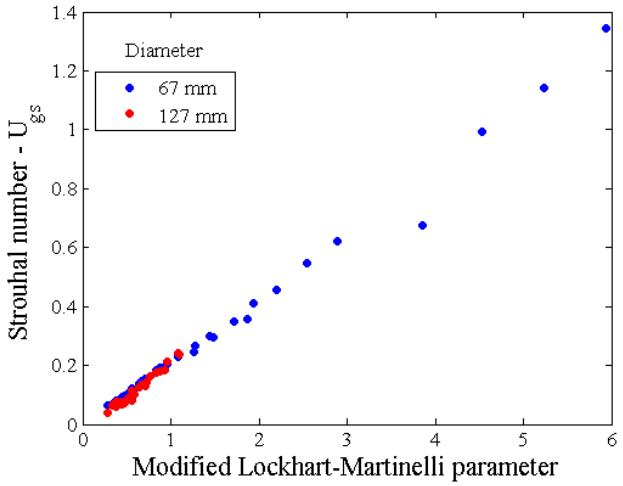


Figure 5.14. Strouhal number based in U_{gs} plotted against the modified Lockhart-Martinelli parameter (equation [5.11]) for 67 and 127 mm diameter pipe and different gas and liquid superficial velocities.

Rearranging equation [5.12], the frequency of the periodic structures can be finally expressed as:

$$f = 7.431 \cdot 10^{-3} \frac{(U_{ls} + 0.534)}{\mathrm{D}} \sqrt{\frac{\rho_l}{\rho_g}} \qquad [5.13]$$

The first graph of Figure 5.15 (left) shows the frequency results in the 67 mm diameter pipe for all the gas and liquid superficial velocities tested as well as the predicted frequency using the correlation above. The second graph (right) shows the experimental values for frequency for the 127 mm diameter pipe whereby no significant variation is observed with gas superficial velocity which, as mentioned earlier, occurs at gas superficial velocity greater than 0.7 m/s. The predicted frequency values using the proposed correlation [5.13] are given in dashed lines.

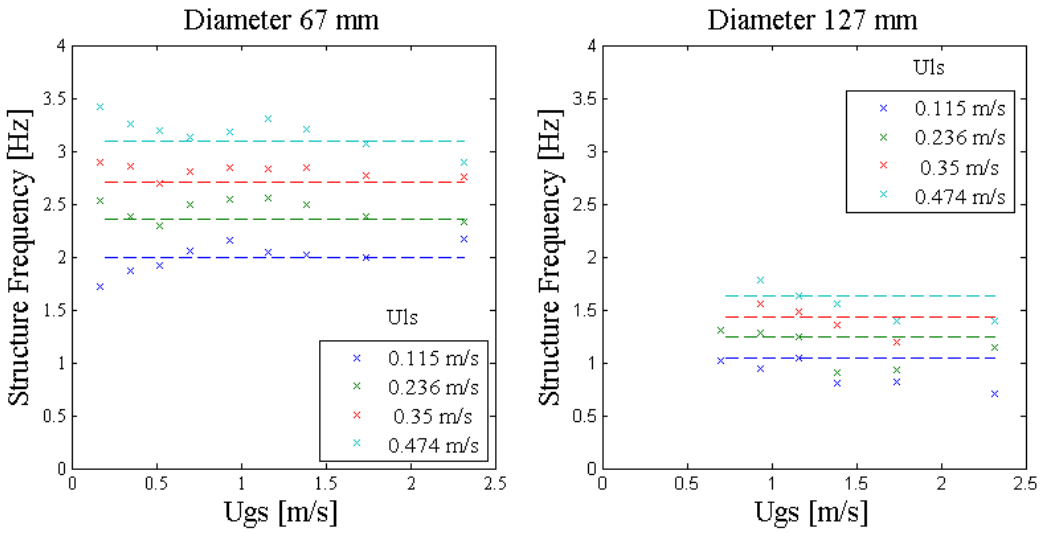


Figure 5.15. Comparison of the experimental frequency values with the new correlation [5.13] for different U_{ls} and for both pipe diameters.

It can be seen in Figure 5.15 that the discontinuous lines, calculated using the new correlation, are horizontal since the correlation is independent of the gas superficial velocity. That agrees very well with the frequency obtained experimentally in the 67 mm diameter pipe. However, the experimental frequency in the 127 mm pipe seems to decrease slightly with increasing gas superficial velocity. This effect is not reflected by the correlation proposed because it is independent of the gas superficial velocity. Nonetheless, since this decrement is very small, the divergence from the correlation is

not significant. This statement is supported by the fact that the determination coefficient of the fit R^2 is 0.99, as explained earlier.

5.5 Conclusions

Intermittent flow was investigated in a 67 and a 127 mm diameter vertical pipes, in the range of gas superficial velocity from 0.17 and 2.32 m/s and the liquid superficial velocity from 0.115 and 0.47 m/s. At low gas velocities the observed flow regime was cap bubble flow and with increasing gas superficial velocity it transitions first to slug flow and followed by churn flow. The intermittent flow, defined as a liquid dominated structure followed by a gas dominated structure repeating at a certain mean frequency, was encountered under all the combinations of velocities studied.

The gas and liquid structures of the intermittent flow are better defined in a small diameter pipes. Whereas, the gas structures appear as elongated bubbles whose length is several times the pipe diameter and the liquid structures appear as liquid slugs that contain a continuous liquid phase with dispersed gas bubbles in them. Contrarily, in large diameter pipes, the gas structures emerge as part of the gas core with some liquid dispersed in them surrounded by an oscillating, foamy and irregular liquid film. The liquid structures (slugs) on the other hand appear very airy and short in between the gas structures.

The velocity of the gas structures was observed to increase with increasing both the gas and the liquid superficial velocity. It increases as well with increasing the diameter of the pipe; this divergence is significant at low U_{gs} (< 1.4 m/s), but they almost equate at higher U_{gs} (> 1.4 m/s).

The experimental data showed a good agreement with the drift-flux model of Nicklin et al. (1962), considering the distribution coefficient C_0 constant and the drift velocity

as a function of the Froude number as suggested by Dumitrescu (1943) and Davies and Taylor (1950). However, better agreement was found considering C_0 as a negative power law of liquid Reynolds number and the drift velocity to be directly proportional to the diameter of the pipe. With these considerations, a new correlation is proposed to calculate the velocity of the gas structures as a function of the gas and liquid superficial velocities as well as the diameter of the pipe.

The frequency of the gas structures was found to increase with increasing liquid superficial velocity. In the 67 mm pipe the frequency did not seem to exhibit any significant trend with the gas superficial velocity whereas in the 127 mm pipe the frequency appeared to decrease with increasing gas superficial velocity and stabilises when the gas velocity increases above 0.7 m/s. On the other hand, the frequency was observed to be higher in the 67 mm compared to the 127 mm pipe diameter for all the gas and liquid velocities studied.

The frequency obtained from both pipes of different diameters showed poor agreement with the correlation in the form of the equation proposed by Fossa et al. (2003). The agreement did not improve when the frequency, expressed as a Strouhal number based on the gas superficial velocity, is correlated with the Lockhart-Martinelli parameter as suggested by Azzopardi (1997). To find a better agreement, the Lockhart-Martinelli parameter was modified by adding a fictitious velocity to the liquid superficial velocity to represent the influence of the liquid column in the vertical gas-liquid two-phase flows. With this supposition, a new correlation to calculate the frequency of the gas structures as a function of the liquid superficial velocity and the diameter of the pipe is proposed. The resultant equation is independent of the gas superficial velocity.

CHAPTER 6.

THE INFLUENCE OF THE ANGLE OF INCLINATION

6.1 Introduction

Gas-liquid two-phase flow in undulating pipe arrangements exhibits varying flow behaviours including severe slugging depending on the volumetric flow rates. This is attributed to the influence of gravity forcing the gas to separate and rise above the liquid. Furthermore, the flow behaviour varies dramatically with the pipe orientation. For example, constant flow rates may produce stratified flow in a horizontal pipe while producing slug flow if the pipe is tilted to the upward direction. The slug frequency may be dependent on the inclination angle. Pipelines could take various layout orientations, especially if it follows the topology of a geographic region. Knowledge of the flow behaviour in such arrangements would undoubtedly lead to a safer and a more robust design. Therefore it is imperative to analyse the influence of the pipe inclination on flow regimes.

The influence of the inclination angle of a pipe on gas-liquid intermittent flows is presented in this chapter. The diametrical distributions of the phases obtained from the wire mesh were examined for the different angles of inclinations ranging from the horizontal to the vertical position to establish if the flow is intermittent or otherwise. This characterisation is aided by visual observation of the flow recorded while running the experiments.

The velocities of the periodic structures were obtained by cross-correlating the void fraction time series of the ECT. The structures were identified from WMS data and their frequency calculated as explained earlier in Chapter 4. Both velocity and frequency

were obtained for the different angles of inclinations at varying combinations of gas and liquid superficial velocities. Thereafter, new correlations to predict velocity and frequency of the periodic structures are posed. The performance of these correlations was assessed against the experimental data whereby a good agreement was produced at all inclination angles.

6.2 Experimental arrangement

The experiments were performed in the 67 mm diameter rig described in Chapter 3. The fluids employed were air and silicone oil whose physical properties were shown earlier in Section 3.1. The test section was positioned at different inclination angles between the vertical (90°) and the horizontal (0°) direction in steps of 15° leading to a total of 7 orientations. A fixed set of gas and liquid flow rates, as presented in Table 6.1, was repeated for each orientation. The flow rate combinations form an experimental matrix of 6 gas superficial velocities and 10 liquid superficial velocities. The exact values are expressed in Table 6.1 and they are plotted on Figure 6.1 in relation to the transition lines of Taitel et al. (1980) and Weisman and Kang (1981) flow pattern maps.

Table 6.1. Gas and liquid superficial velocities employed.

Liquid superficial velocities, U_{ls} [m/s]									
0.023	0.047	0.115	0.23	0.35	0.47				
Gas superficial velocities, U_{gs} [m/s]									
0.17	0.35	0.52	0.70	0.93	1.16	1.39	1.74	2.32	2.9

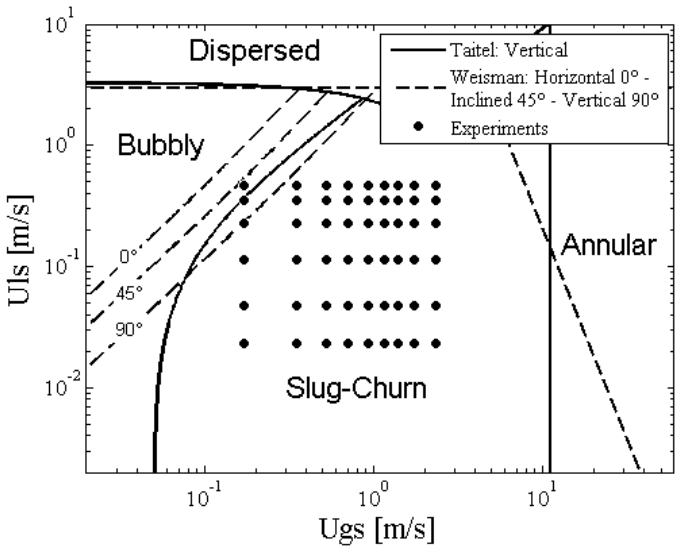


Figure 6.1. The experimental matrix plotted on both Taitel et al. (1980) and Weisman and Kang (1981) flow pattern maps.

Figure 6.1 suggests that the flow regimes expected are slug and churn in most of the cases with bubbly flow around the transition to slug flow in few of them. The bubbly flow occurs at high liquid superficial velocity (U_{ls}) and low gas superficial velocities (U_{gs}) as can be seen in Figure 6.1. The transition to slug flow depends on the inclination angle according to Weisman and Kang (1981) flow pattern map (dashed lines).

A total of 420 experimental runs were carried out. The void fraction information was acquired at a 1000 Hz frequency for a period of one minute from both the ECT and the WMS. At gas superficial velocities higher than 1 m/s, the acquisition frequency of the ECT was increased to 4000 Hz to allow for cross-correlate the signals from the ECT measuring planes.

6.3 Results

Results presented in this section were obtained after processing of the ECT and the WMS data following the processes explained in Chapter 4.

6.3.1 Image reconstruction of the flow

Phase distribution images were reconstructed from the diametrical time series of void fraction data acquired by the WMS. The reconstruction methodology was fully explained in Section 4.4.

Figure 6.2 shows the flow reconstruction for various inclination angles for a fixed liquid and gas superficial velocities (U_{ls} = 0.35 and U_{gs} = 0.52). For the ease of presentation, the images are displayed in horizontal orientation with the respective inclination angles noted against them. The gas-liquid mixture flows from right to left. It can be seen from the figure that the gas bubbles divert from the centre of the pipe towards the upper wall with the decrease of the inclination angle from vertical to horizontal. The size of the bubbles seems to decrease as well and the number of big bubbles decreases with decreasing the angle.

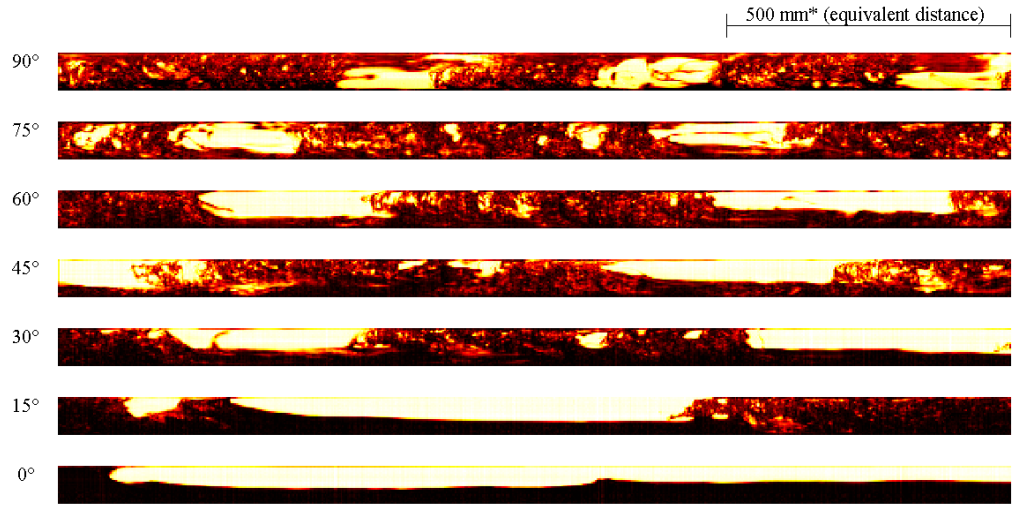


Figure 6.2. Flow reconstruction at different inclination angles of the pipe. The gas and liquid superficial velocities are fixed at U_{ls} = 0.35 m s-1 and U_{gs} = 0.52 m s-1.

In order to assess the intermittency of the flows encountered, image reconstruction using WMS diametrical time series data are examined. Upper and lower bounds of the flow for each phase (the four corners of the experimental matrix) are selected for this purpose and presented in Figures 6.3, 6.4, 6.5 and 6.6. In each figure, four columns appear

corresponding to 90° (vertical), 60°, 30° and 0° (horizontal) positions. The axial scale is modified by a factor of 10 compared to the radial scale. This is executed to visualise more flow variations and to observe more intermittencies of the gas and liquid structures along the pipe.

At the highest U_{ls} and lowest U_{gs} as depicted in Figure 6.3, cap bubble flow is observed in the vertical and inclined angles. However, as the pipe approaches the horizontal position, larger bubbles form plug flow whereby bubbles move at the same velocity as the liquid. That observation comes in perfect agreement with Weisman and Kang (1981) flow pattern map seen in Figure 6.1. Cap bubbles in bubbly flow are big enough to be recognised as dominant gas structures as their length and frequency can be measured. In this case, cap bubble flow can be considered the intermittent as well.

Considering the case at highest U_{ls} and the lowest U_{gs} presented in Figure 6.4, transition from slug to churn is observed at the 90° and 60° positions. This is characterised by very irregular bubbles followed by short and airy liquid slugs. At the 30° and 0° orientations the gas bubbles appear better defined, whilst the slugs are observed to contain more liquid. Gas and liquid structures can be identified at all the angles at these flowrates.

At the lowest U_{ls} and U_{gs} as depicted in Figure 6.5, slug flow is observed in all the angles considered. At vertical position, the large gas bubbles seem more irregular in shape, while the density of dispersed bubbles in the slugs appears high. As the pipe assumes the horizontal position, the gas bubbles elongate while moving attached to the upper side of the pipe. However, the liquid slugs are still maintained. Intermittency is clearly visible for all the angles at these conditions.

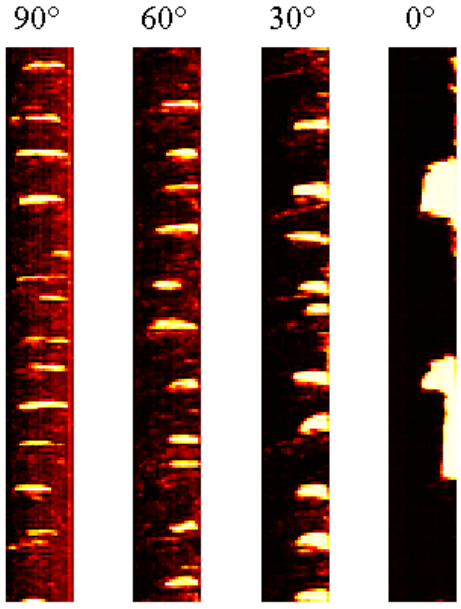


Figure 6.3. Flow reconstruction at U_{gs}=0.17 m/s and U_{ls}=0.47 m/s at different angles. Axial scale = Radial scale x10.

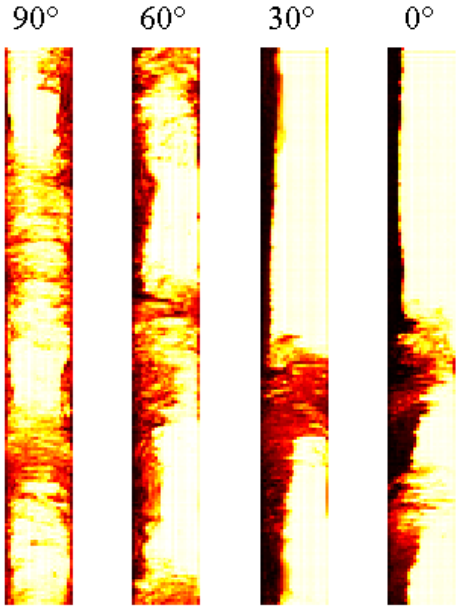


Figure 6.4. Flow reconstruction at U_{gs}=2.9 m/s and U_{ls}=0.47 m/s at different angles. Axial scale = Radial scale x10.

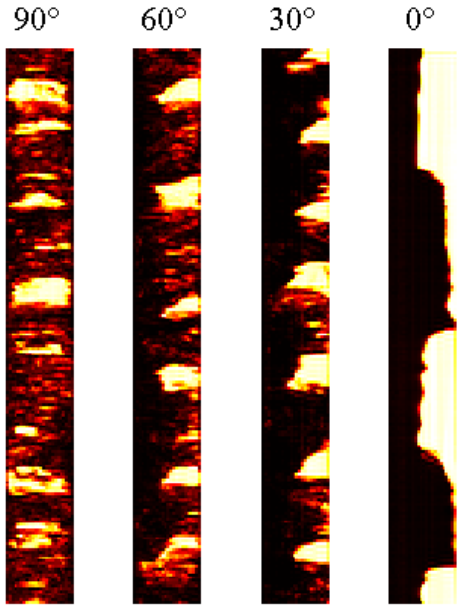


Figure 6.5. Flow reconstruction at U_{gs}=0.17 m/s and U_{ls}=0.023 m/s at different angles. Axial scale = Radial scale x10.

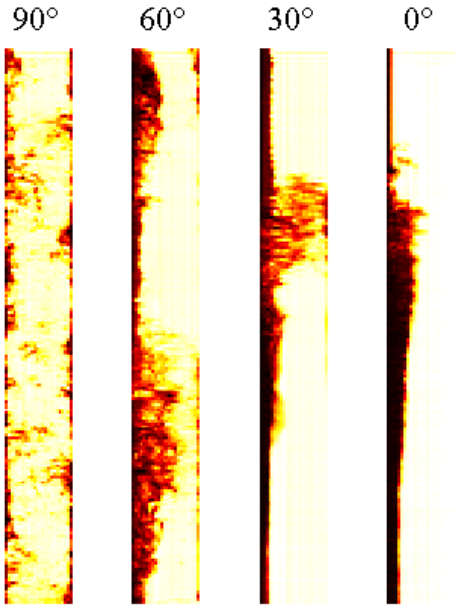


Figure 6.6 Flow reconstruction at U_{gs}=2.9 m/s and U_{ls}=0.023 m/s at different angles. Axial scale = Radial scale x10.

Finally, at lowest U_{ls} and highest U_{gs}, Figure 6.6 shows that the intermittencies become harder to recognise. At the vertical position churn flow is observed. Whilst there zones dominated by gas and others by liquid appear in the pipe, yet no periodical structure can

be identified. At 60° and 30° inclination positions slug flow is reflected, whereby the gas and liquid structures can be distinguished. In the horizontal position, the two-phase flow appear to be separated.

6.3.2 Gas structure velocities

The velocity of the gas structures is calculated by cross-correlating the signals produced by the dual planes of the ECT sensor as explained in Section 4.7.

The values of the structure velocities for all the runs are represented in six graphs in Figure 6.7 each representing velocities at a constant liquid superficial velocity as noted in the figures. The gas structure velocity is plotted against the inclination angle (7 different angles from horizontal to vertical). In each sub-figure several graphs are plotted, each is colour coded to the corresponding gas superficial velocity as per the legend. For the points corresponding to gas superficial velocity equal or lower than 1.74 m/s, these lines are reasonably smooth whereas they could be easily adjusted to a second-degree polynomial. At higher gas superficial velocity, the distribution of the structure velocities varies in such a way that approximating using a polynomial is deemed inappropriate. This discrepancy is due to the limitation imposed by the acquisition frequency making the cross-correlation of ECT signals less accurate. Another source affecting the accuracy is the rotameter reading where the fluctuations make the reading challenging. The rotameter fluctuations are linked to the high and rapid fluctuations of the pressure that occurs in the test section at high gas superficial velocities.

The uncertainties of the gas structures velocities are also represented in Figure 6.7. They were calculated following the same method applied in the previous chapter, using

equation [5.1]. The mean uncertainty is 0.09 m/s and the maximum is 0.2 m/s. All the numerical values are detailed in the Appendix.

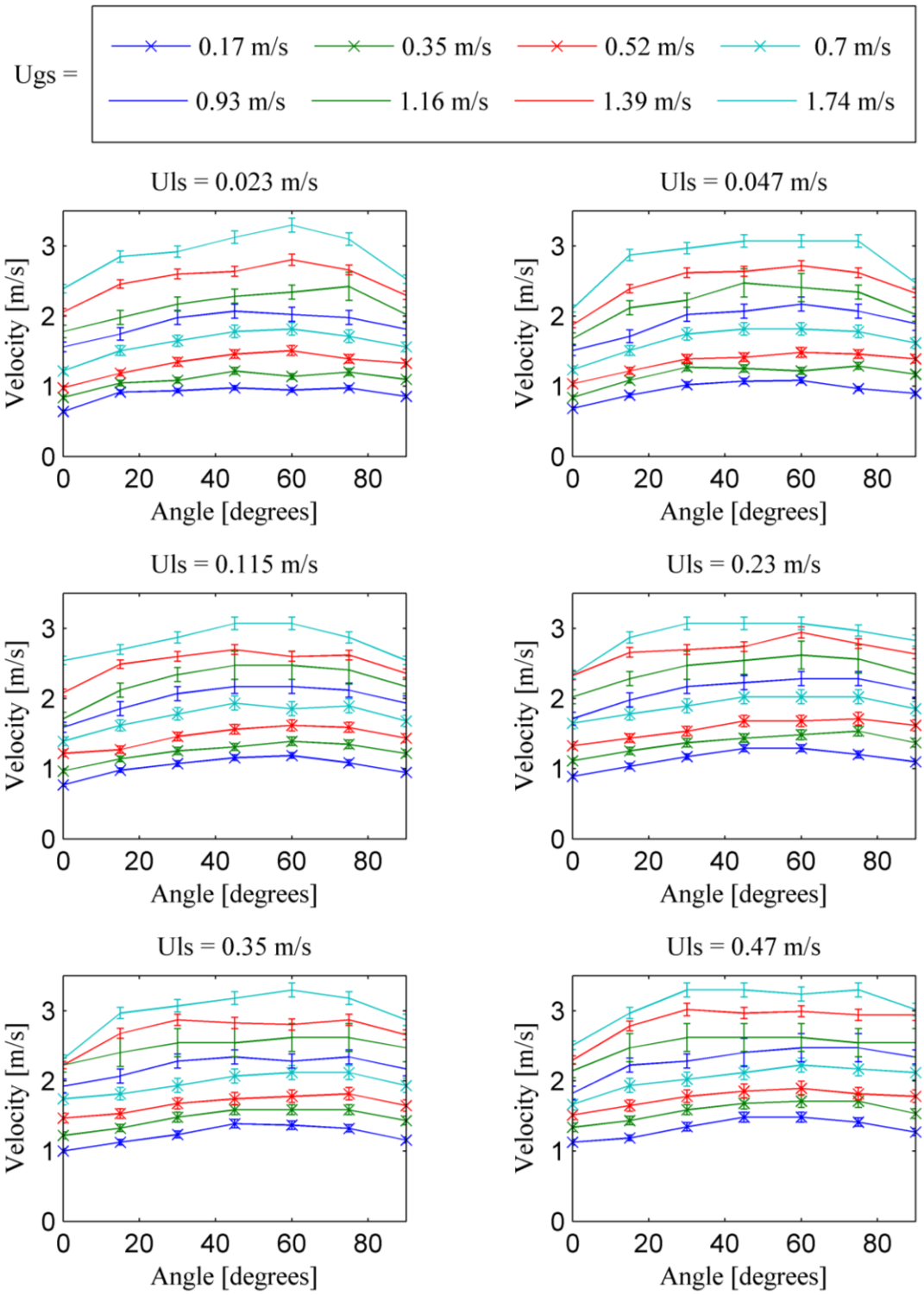


Figure 6.7. Gas structures velocity plotted against angle of inclination. Each graph corresponds to a constant U_{ls}, each line is colour coded to the corresponding U_{gs} as denoted in the legend.

It can be seen that the gas structure velocity always increases with both gas and liquid superficial velocity. That comes in concordance with the equation of Nicklin equation (Eq. [2.23]). The second observation to be noted is that the velocity first increases and then decreases with the angle for all gas and liquid superficial velocities combinations. The maximum appears to always occur at approximately 50° as Zukoski (1966) had previously reported. This behaviour can be referred to the two opposing forces acting on the gas structures: buoyancy and friction. Buoyancy increases proportionally to $\sin \alpha$, where α is the inclination angle. The sinus of α equals zero at the horizontal position ($\alpha = 0$), since the gravity and the movement of the gas in perpendicular. On the other hand, friction depends on the drift velocity as well as the gas-liquid interfacial area. The friction acting on the gas structures contributes to the total pressure drop in the pipe, which in turn proved to increasing with increasing the inclination angle in most of the cases (Nicholson et al., 1978). The equilibrium of these two forces produces a maximum velocity somewhere in between the vertical and the horizontal position.

6.3.3 Gas structure frequencies

Gas structure frequency is the other characteristic that defines intermittent two-phase flows. This frequency is calculated considering the dominant frequency of the cross-sectional averaged void fraction time series obtained from the WMS. The dominant frequency is the one corresponding to the highest energy in the power spectrum density function (PSD). When the dominant frequency is not clear on the PSD because there are many peaks in the PSD function, it is selected by contrasting against the frequency obtained by counting the peaks in the void fraction timer series. Both methods were explained in detail in Section 4.9. The error bars shown correspond to the uncertainty of the PSD when it is averaged by 8 samples. It is evaluates as 0.35 Hz ($1/\sqrt{8}$).

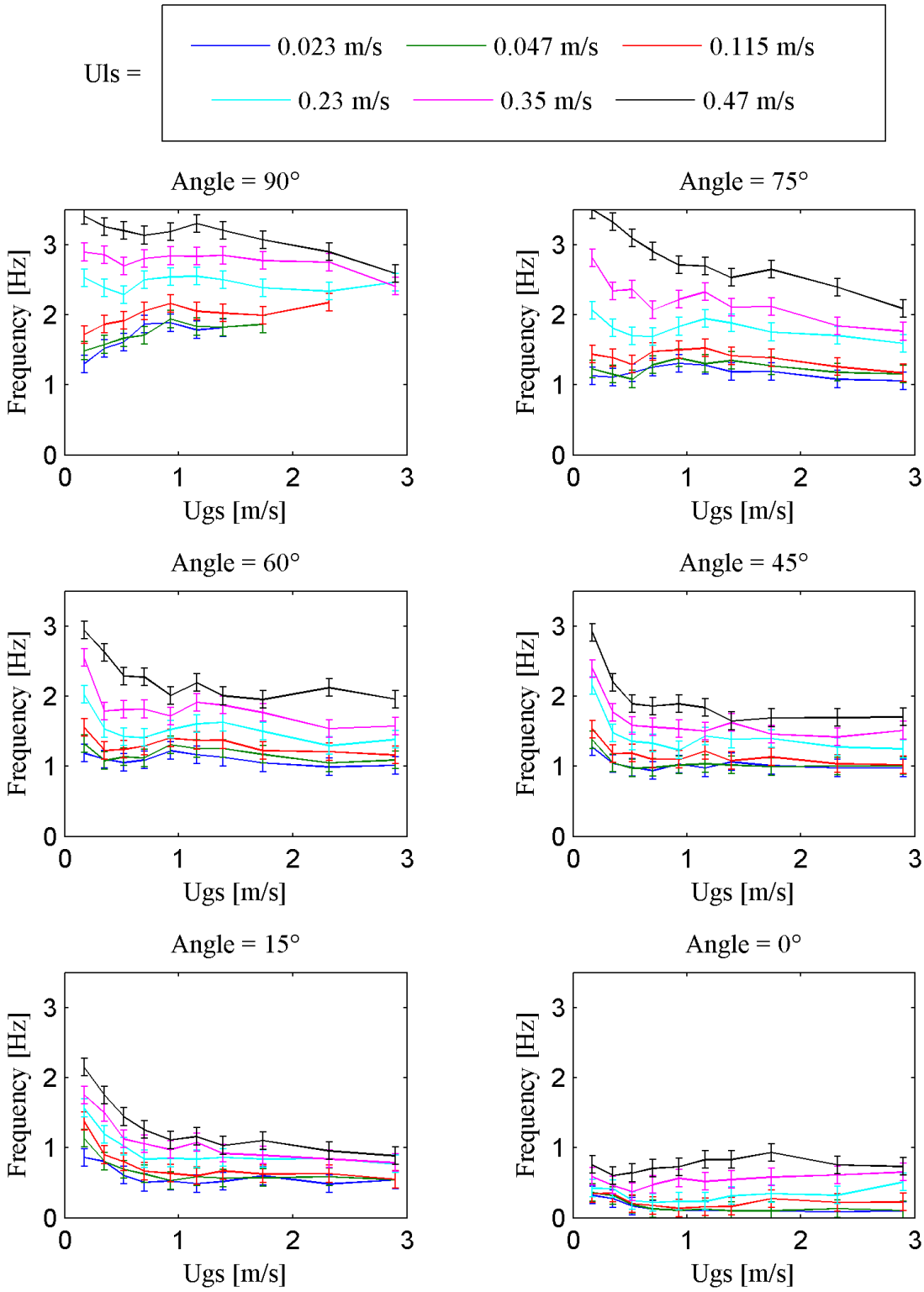


Figure 6.8. Gas structures frequency plotted against gas superficial velocity U_{gs}. Each graph corresponds to one inclination angle, each colour line represents a different U_{ls}.

Frequency values are presented in Figure 6.8 in 6 graphs corresponding to 6 different angles of inclination (60° results are not plotted in Figure 6.8). In each graph, it can be

seen how the frequency varies with the gas and the liquid superficial velocities. It can be plainly observed that that frequency increases by increasing the angle of inclination. At the horizontal position, as manifested earlier, the gas structures are very long resulting in less number of bubbles passing through for a fixed period of time. Naturally, increasing the inclination angle results in an increases number of smaller/shorter gas structures. This was noted earlier from the observation of the image reconstruction as well as the eye observation while carrying the experiments. The second observation is that the frequency always increases with the liquid superficial velocity, U_{ls}, regardless of the inclination angle and the gas superficial velocity, U_{gs}. Finally, it is observed that the frequency trend while varying the U_{gs} is different with different inclination angles and U_{ls}. At vertical position (90°), the frequency seems to decrease with increasing U_{gs} at high U_{ls} while it increases at low U_{ls}. For the inclined positions, the frequency seems to decrease with U_{gs} for all the U_{ls} whilst it stabilises to a constant frequency once U_{gs} is higher than 0.7 m/s. In the horizontal position (0°), the frequency does not seem to exhibit big variations with increasing the gas superficial velocity.

6.4 Discussions

6.4.1 Velocity of the gas structures

The velocity of the gas structures was shown earlier in Figure 6.7. The velocity values for each angle can be satisfactorily adjusted to an equation of the form suggested by Nicklin (Eq. [2.23]). The distribution coefficients C_o, the drift velocity V_d and the coefficient of determination R^2 are presented in Table 3.1 for all the angles. The corresponding Froude numbers are shown as well.

Table 6.2. C_o, V_d that fits better to the experimental results at different inclination angles and their corresponding Froude number, Fr, and the determination coefficient, R^2.

Angle, α	C_o	V_d	$Fr = V_d/\sqrt{Dg}$	R^2
0	0.983	0.539	0.665	0.961
15	1.190	0.585	0.722	0.982
30	1.218	0.707	0.872	0.983
45	1.198	0.811	1.001	0.978
60	1.222	0.812	1.003	0.970
75	1.196	0.802	0.990	0.976
90	1.092	0.728	0.898	0.976

The coefficients given in Table 6.2 are generated from successful curve fitting of the data for all the angles; R^2 is always higher than 0.961. The C_o coefficient is not constant for all the angles; it varies from 0.983 to 1.218 while the drift velocity, V_d, changes too. It should be noted that the drift velocity at 0° inclination, V_d^h, is higher than 0 ($V_d^h > 0$). Historically, there has been a considerable discussion concerning the value of the drift velocity in the past about whether it could be different from 0 in horizontal pipes. First, Hubbard (1965) and then Gregory and Scott (1969) adjusted their drift velocity measurements in horizontal pipes to obtain a straight line whose origin was at 0 ($V_d^h = 0$). Later, several other authors suggested that the accuracy of the curve fitting could be improved if a nonzero value for the drift velocity in horizontal pipes $\left(V_d^h > 0\right)$ is considered (Singh and Griffith, 1970, Mattar and Gregory, 1974, Nicholson et al., 1978). This approach can be clearly seen befitting to the present data shown in Table 3.1. However, the aforementioned authors could not give a physical explanation to justify the existence of this drift velocity in horizontal pipes. Typically, a bubble introduced into a horizontal pipe filled with a liquid would decelerate due to fluid friction and would rise to the upper surface of the pipe before becoming stationary. There would not be any resultant force to drive its movement along the axial direction.

Therefore, it is plausible to deduce that there is no axial resultant force acting on the bubble in a horizontal pipe that would induce a drift velocity. Weber (1981) investigating horizontal tubes suggested that a horizontal tube would drain generating gas bubbles flowing into it if the tube diameter is large enough to give an Eötvös number above a critical value. The drift velocity of the bubbles in a draining horizontal pipe was found to be the same as the value that had already been theoretically calculated by Benjamin (1968) for draining of horizontal pipes. This drift velocity is given by $V_d^h = 0.53\sqrt{Dg}$ (Weber, 1981). They proposed that the energy driving the bubble is generated by the height of the liquid being drained across the diameter of the pipe. This last expression has been used in correlations and models for horizontal and inclined flows (Malnes, 1983, Bendiksen, 1984, Alves et al., 1993). However, it is not clear if the drift velocity in a horizontal pipe is equal to the gas bubble propagating inside a draining pipe. Liquid in a draining pipe has a negative superficial velocity, equal in magnitude but in opposite direction to the gas superficial velocity. It can be said that the mixture superficial velocity is zero, but neither the liquid nor the gas superficial velocities, therefore; the velocity measured in a draining pipe cannot be considered a drift velocity.

To investigate further into why the experimental results do not fit to a straight line starting from 0, the following explanation can be established. The data fits to a straight line if the C_o coefficient is considered a constant. However, if the coefficient C_o varies with the Reynolds number, a curve instead of a straight line will be expected. It is known that for laminar flow $C_o = 2$ whereas it reduces with increasing the Reynolds number. Frechou (1986) proposed an empirical correlation [Eq. 2.24] for C_o as a function of Reynolds number. Another empirical correlation is proposed here, expressed in Equation [6.1].

$$C_0(Re_l) = C\ Re_l^{-n} \qquad [6.1]$$

Then the bubble velocity in horizontal flow can be calculated as:

$$V_b^h = C\ Re_l^{-n}\ U_{ms} \qquad [6.2]$$

The experimental results for horizontal pipes have been fitted to the equation [6.2]. The Reynolds number corresponds to that of the liquid phase moving at the mixture velocity. The coefficients obtained and the R^2 are shown in Table 6.3.

Table 6.3. Parameters C and n of the equation [6.2] that fit better with the experimental data in the horizontal position and the determination coefficient.

Angle	C	n	R^2
0	52.36	0.372	0.971

The two fittings are plotted in Figure 6.9. The blue line is a straight line considering $V_d^h > 0$. The red line has zero intercept ($V_d^h = 0$), C_0 decreases with increasing Reynolds number as in Equation [6.1].

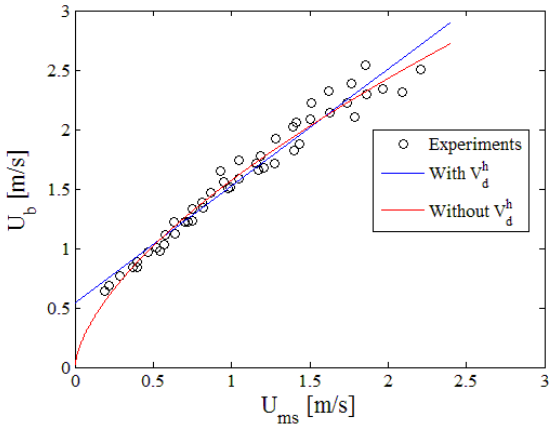


Figure 6.9 Fitting the experimental data in horizontal position to a straight line considering $V_d^h > 0$ (in blue) and fitting to a curve with zero intercept $V_d^h = 0$ (in red).

Bendiksen (1984) proposed a practical correlation to calculate the drift velocity for any angle from horizontal to vertical as a combination of two values V_d^h and V_d^v:

$$V_d = V_d^h \cos\alpha + V_d^v \sin\alpha \quad [6.3]$$

This equation combined with Niklin's equation is presented in equation [6.4]. It was found to fit very well with experimental data. The fitting coefficients C_o, V_d^h and V_d^v are shown in Table 6.4. The adjustment is very good (R^2 = 0.967), however this formula considers a value higher than zero for the drift velocity ($V_d^h > 0$) which, as elucidated earlier, has no physical explanation.

$$V_b = C_0 U_{ms} + V_d^h \cos\alpha + V_d^v \sin\alpha \quad [6.4]$$

Table 6.4. Distribution coefficient C_o, drift velocity in horizontal and vertical positions V_d^h , V_d^v and determination coefficient R^2.

Angle, α	C_o	V_d^h [m/s]	V_d^v [m/s]	R^2
0 - 90	1.136	0.448	0.757	0.967

Hasan and Kabir (1988) proposed another expression for the drift velocity for any angle of inclination from the vertical to the horizontal position. They performed a force balance between the buoyancy force and the drag force. The drag force was considered to increase with the inclination angle since the Taylor bubble becomes sharper with decreasing the inclination angle of the pipe. This variation follows the form of $(1 + \cos\alpha)^{2n}$. Following the force balance, the drift velocity is expressed as:

$$V_d = V_d^v \sqrt{\sin\alpha}\,(1 + \cos\alpha)^{1.2} \quad [6.5]$$

The above equation has a strong physical meaning since the drift velocity is based on a force balance whereby for horizontal pipes ($\alpha = 0$) the drift velocity is predicted as zero.

Substituting of the drift velocity of Hasan and Kabir (1988) equation into Niklin's formula is expressed in equation [6.6]. The coefficients are fitted to the experimental data and their values and determination coefficient R^2 are shown in Table 6.5.

$$V_b = C_0 U_{ms} + V_d^v \sqrt{\sin\alpha}\,(1+\cos\alpha)^{1.2} \qquad [6.6]$$

Table 6.5. Distribution coefficient C_o, drift velocity vertical positions V_d^v and determination coefficient. R^2

Angle	C_o	V_d^v [m/s]	R^2
0 - 90	1.286	0.471	0.939

Bendiksen (1984) expression for the drift velocity in inclined pipes gives a better prediction of the experimental results compared to the one by Hasan and Kabir (1988). Both expressions are plotted against the measured gas structure velocity values in Figure 6.10 and Figure 6.11. Bendiksen (1984) equation can be seen to overpredict the velocity for inclined pipes but always with a divergence lower than 20%. On the other hand, Hasan and Kabir's (1988) model predicts structure velocities better in inclined pipes whilst fails to give a satisfactory prediction for horizontal pipes (black dots in Figure 6.11). As reflected by Figure 6.11, the deviation in this case becomes much greater than 20%.

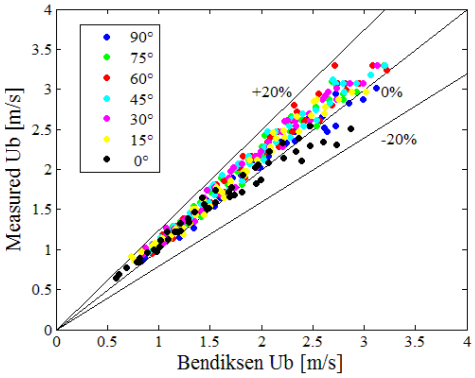


Figure 6.10. Comparison of experimental results with the values calculated using the correlation of Bendiksen (1984).

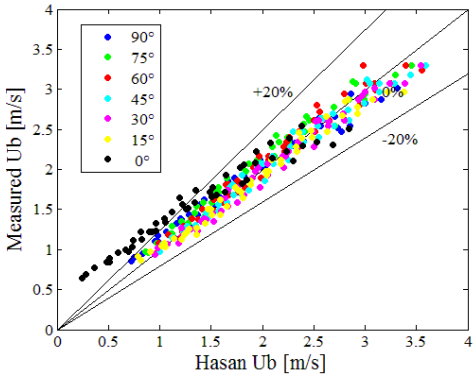


Figure 6.11. Comparison of experimental results with the values calculated using the correlation of Hasan and Kabir (1988).

Equation [6.6] represents a combination of Nicklin equation and Hasan and Kabir expression (Equation [2.29]) for the drift velocity. Further modification could be

achieved by considering C_0 to be a function of Reynolds number as elucidated before (Equation [6.1]).

$$V_b = C\ Re^{-n}\ U_{ms} + V_d^v \sqrt{\sin\alpha}\,(1+\cos\alpha)^{1.2} \qquad [6.7]$$

C, n and V_d^v parameters were adjusted to the experimental results and the obtained fitting can be judged very good. The resultant values are shown in Table 6.6 while the comparison against the experimental values is presented in Figure 6.12.

Table 6.6. Fitting parameters C and n, velocity in vertical positions V_d^v and determination coefficient R^2.

Angle, α	C	V_d^v [m/s]	n	R^2
0 - 90	1.53	0.328	0.237	0.968

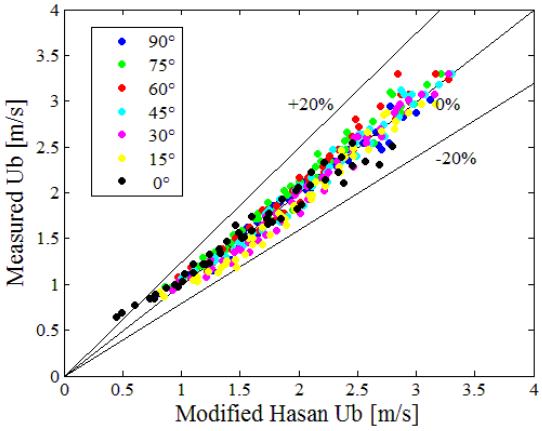


Figure 6.12 Comparison of experimental results against the values calculated using the correlation of Hasan and Kabir (1988) and C_0 as a function of the Reynolds number.

A new expression [6.7] is developed to calculate the gas structure velocity in intermittent flows in horizontal, vertical, and inclined pipes. The structure velocity is considered a sum of the drift velocity, V_d, and the maximum velocity at the centre of the pipe as suggested by Zuber and Findlay (1965). The drift velocity is predicted using the equation of Hasan and Kabir (1988) (equation [2.29]). It has also been considered that the maximum liquid velocity in the pipe is dependent on the Reynolds number as shown in equation [6.1]. The obtained expression's predictions agree very well with

experimental results. The determination coefficient is close to 1 (R^2 = 0.968) while the divergence in all the cases is lower than 20% as as depicted in Figure 6.12. The only 3 points of the 420 runs falling out of the 20% deviation in Figure 6.12 correspond to low gas superficial velocities in the horizontal position. This higher discrepancy can be referred to the fact that slugs might not be completely developed under these conditions. The agreement can be more clearly seen in the profiles presented in Figure 6.13, where the experimental results and the proposed model predictions are plotted together.

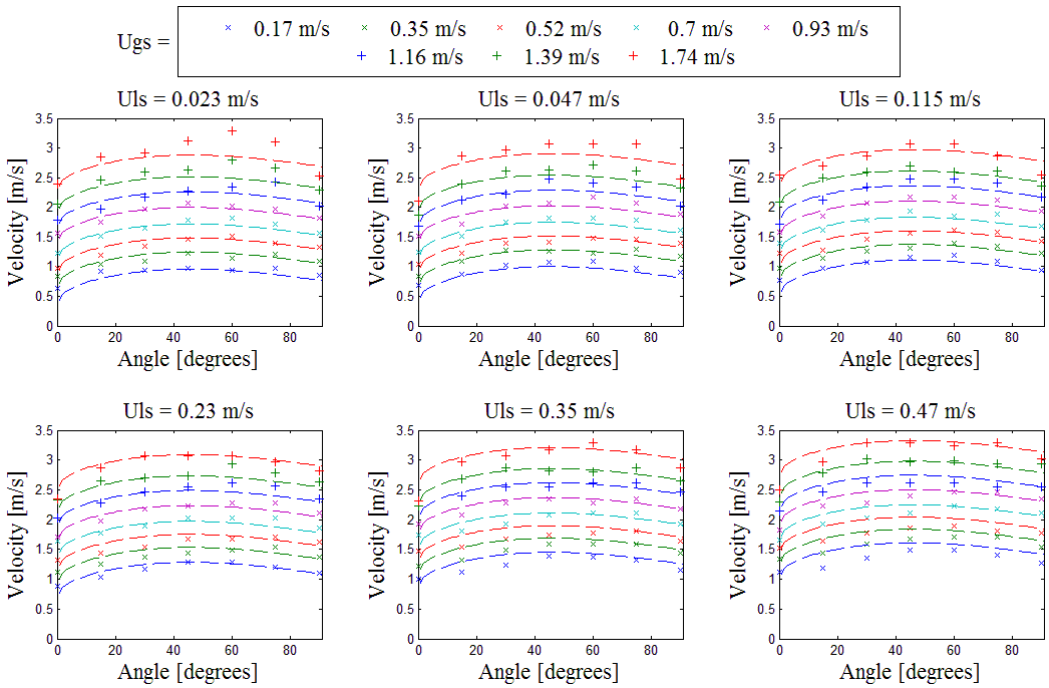


Figure 6.13 Comparison of the experimental values with the correlation function [6.7] at different U_{gs} and U_{ls} and at different angles of inclination.

6.4.2 Gas structures frequency

In this section, the experimentally obtained gas structure frequencies (Figure 6.8) are compared with the existing correlations. A new correlation is proposed following that existing correlations in the literature were either developed for horizontal flows or otherwise to calculate the frequency of big waves in annular flow, therefore failing to predict the frequencies for all inclination angles obtained in this study.

Figure 6.14 shows the gas structure frequencies obtained experimentally expressed as the dimensionless Strouhal number plotted against the Lockhard-Martinelli parameter in logarithmically scaled axes. Gas superficial velocity is used to compute the Strouhal number since it produces a better correlation compared to the liquid superficial velocity, the gas structures velocity, or the mixture velocity.

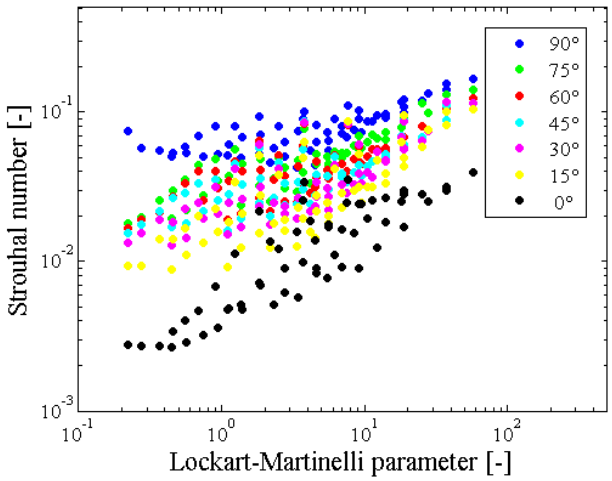


Figure 6.14 Strouhal number calculated using the U_{gs} plotted against Lockart-Martinelli parameter at different angle of inclination in logarithmic scale.

It can be seen in Figure 6.14 that the relationship between the Strouhal number and the Lockhart-Martinelli parameter is positive. This type of correlation was suggested by Azzopardi (1997) to calculate the frequency of the waves in annular flow where he found that Strouhal and Lockhart-Martinelli numbers are inversely proportional. The points of the graphs can be fitted to straight lines for each inclination angle, but in linear scale axis they follow a power law of the form:

$$St = \mathrm{a}\ \chi^{b} \qquad [6.8]$$

The values of a and b for each angle of inclination and the determination coefficients are presented in Table 6.7. It can be seen that the fitting is not very good, R^2 is not close to 1 but varies from 0.863 to 0.702. In addition, the coefficients of a and b are different for each angle.

Table 6.7. Parameters a and b of equation [6.8] that give better fitting with the experimental data and the determination coefficients R^2.

Angle, α	a	b	R^2
0	0.0074	0.4124	0.702
15	0.0138	0.4958	0.723
30	0.0190	0.4222	0.713
45	0.0227	0.3823	0.731
60	0.0261	0.3569	0.770
75	0.0283	0.3904	0.863
90	0.0173	0.0874	0.834

The experimental results frequency is employed to assess the performance of the correlation of Zabaras (1999). The comparison is presented in Figure 6.15. It can be noted that there is only some agreement around horizontal pipe (0°) data and the slightly inclined pipe (15°), however it fails to adequately predict the frequency for all the other angles. It must be noted that Zabaras (1999) equation is a modification of the correlation of Gregory and Scott (1969) for horizontal pipes. Whereby Zabaras (1999) only applied it for small deviations from the horizontal position (from 0 to 11°).

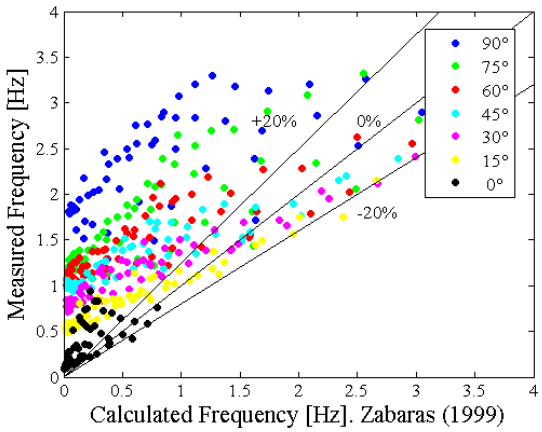


Figure 6.15 Comparison of experimental frequency against the predictions of Zabaras (1999) correlation.

Evidently, the former two correlations fail to predict the structure frequencies for all other angles of inclinations of the pipe when the flow is intermittent. For this reason, a new empirical correlation is proposed.

Inspecting closely the results in Figure 6.8, it can be seen that frequency

- increases linearly with U_{ls} for all the cases
- increases with the inclination angle of the pipe for all the cases.

Furthermore, the influence of the gas superficial velocity U_{gs} could be summarised as follows.

  - In vertical pipes: frequency increases at U_{ls} < 0.115 m/s and decreases at U_{ls} > 0.23 m/s
  - In inclined pipes: frequency decreases potentially at U_{gs} < 0.7 and then it stabilizes to a constant value
  - In horizontal pipes: frequency does not present significant variations with varying U_{gs}.

Considering that the frequency increases linearly with U_{ls}, decreases following a power law with U_{gs} and increases following a trigonometric function with increasing the inclination angle of the pipe (α), it can be expressed as a function of the form:

$$f = \mathrm{A} + \mathrm{B}\, U_{ls} + \mathrm{C}\, {U_{gs}}^{-s} + (E\, (\sin\alpha)^n + F(\cos\alpha)^m) \qquad [6.9]$$

This equation can be simplified only if the experiments in which U_{gs} was higher than 0.7 m/s are considered. Above this value, the frequency does not show significant changes with increasing U_{gs}. In that case equation [6.9] can be expressed as:

$$f = \mathrm{A} + \mathrm{B}\, U_{ls} + (E\, (\sin\alpha)^n + F(\cos\alpha)^m) \qquad [6.10]$$

The experimental points are fitted to the equation above. The coefficients obtained and the determination coefficient are shown in Table 6.8. As it can be seen, the fitting is excellent, $R^2 = 0.948$.

Table 6.8. Coefficients obtained by fitting experimental frequency to equation [6.10] and the determination coefficient obtained.

Angle, α	A [Hz]	B [Hz s/m]	E [Hz]	F [Hz]	N	m	R^2
0 - 90	1	1.95	1	-1	0.7	0.3	0.948

The equation with the fitting coefficients can be written now as:

$$f = 1.95\, U_{ls} + (1 + (\sin\alpha)^{0.7} - (\cos\alpha)^{0.3}) \qquad [6.11]$$

And for horizontal position($\alpha = 0$), the equation becomes:

$$f(\alpha = 0) = 1.95\, U_{ls} \qquad [6.12]$$

Equation [6.13] illustrates how the frequency, expressed as the gas-based Strouhal number is related to the Lockhart-Martinelli parameter. That relationship can be written as:

$$\frac{f\ D}{U_{gs}} = \mathrm{a}\left(\frac{U_{ls}}{U_{gs}}\sqrt{\frac{\rho_l}{\rho_g}}\right)^{b} \qquad [6.14]$$

considering b=1, it is possible to produce an explicit expression for the frequency as:

$$f = \mathrm{a}\frac{U_{ls}}{D}\sqrt{\frac{\rho_l}{\rho_g}} \qquad [6.15]$$

For a known pipe diameter and gas and liquid densities, equation [6.15] can have the same form as [6.12] if $\mathrm{a} = 1.95/\left(\frac{1}{\mathrm{D}}\sqrt{\frac{\rho_l}{\rho_g}}\right) = 0.0048$

This equivalency is only evident when the pipe is in horizontal position($\alpha = 0$), because at different inclinations the frequency is dependent of the angle as denoted in equation [6.11]. To obtain an expression similar to equation [6.15] for any other angle of inclination, a different velocity is used instead of the liquid superficial velocity in the calculation of the Lockhart-Martinelli parameter, this new velocity is calculated from equation [6.11] and it is equal to:

$$U'_{ls} = U_{ls} + 0.51 \cdot (1 + (\sin \alpha)^{0.7} - (\cos \alpha)^{0.3} \qquad [6.16]$$

The terms of the equation of U'_{ls} have physical meanings that will be discussed in Chapter 8.

Thereafter, substituting U'_{ls} (from equation [6.16]) for U_{ls} in equation [6.15], the frequency of the gas structures can be calculated as:

$$f = 0.0048 \, \frac{U_{ls} + 0.51 \cdot (1 + (\sin \alpha)^{0.7} - (\cos \alpha)^{0.3}}{D} \sqrt{\frac{\rho_l}{\rho_g}} \qquad [6.17]$$

This expression is only valid when the frequency does not vary significantly with increasing the gas superficial velocity, U_{gs}, in this case, it happens when $U_{gs} > 0.7$ m/s.

In Figure 6.16, the frequencies obtained from the experiments are plotted against those predicted by the expression [6.14]. It can be seen that the disparity of the values is mostly limited within 20%, whereby the biggest discrepancies appear when α=0 (horizontal pipes). It must be noted that in horizontal pipes the measurement of the frequency was much difficult because the flow was not fully developed, it was observed that some gas structures occupied the entire length of the pipe whereby the flow became stratified for a short period of time; in a way no any intermittency could be detected. For this reason the measured frequency of the gas structures probably is lower than it would have been had the length of the pipe been longer.

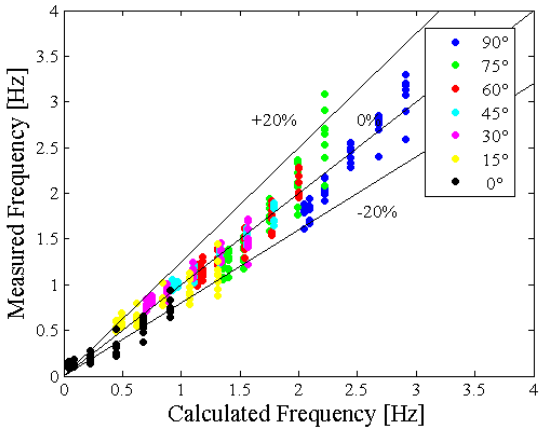


Figure 6.16 Comparison of the experimental frequency against the predictions of the new correlation presented in equation [6.14].

In Figure 2.1 the profiles of the experimental frequency are plotted again against gas superficial velocity as in Figure 5.6 but it also including the predictions obtained from expression [6.14] plotted in straight lines.

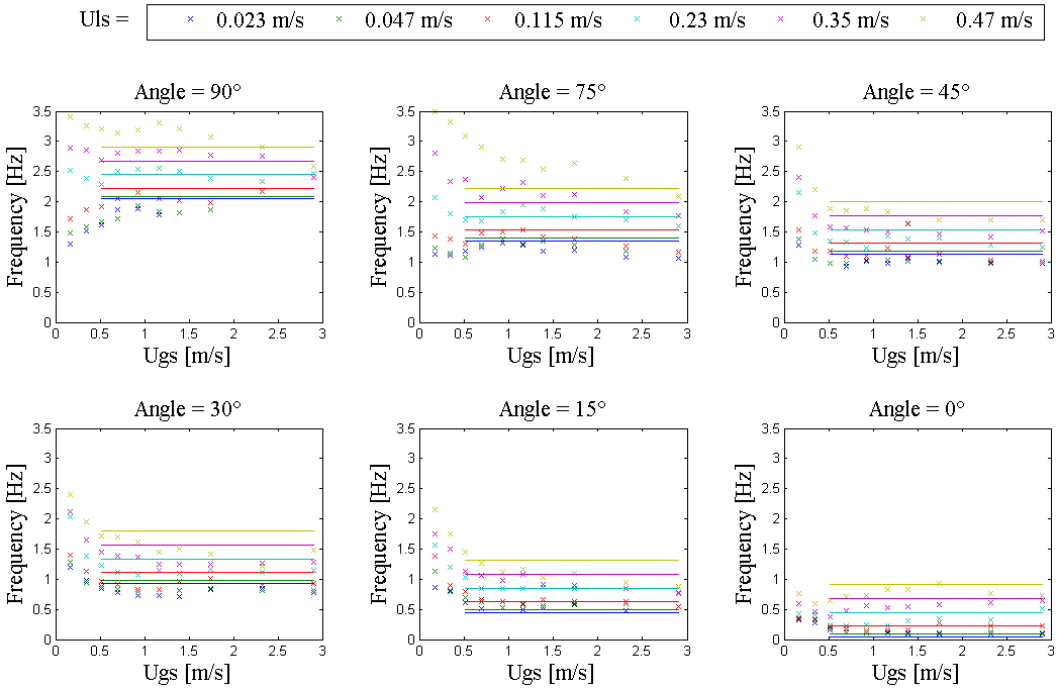


Figure 6.17 Comparison of the experimental frequency values against the predictions of the correlation of equation [6.14] at different U_{ls} and at different angles of inclination.

6.5 Conclusions

Intermittent flows were identified in the experimental data generated in this work at different gas and liquid superficial velocities while varying the angles of inclination. The flow regimes encountered were characterised as cap bubble, slug, plug, and churn flow regime depending on the inclination angle of the pipe, liquid superficial velocity ($U_{ls,}$), and gas superficial velocity (U_{gs}). Only in the case of low $U_{ls,}$ high U_{gs} in the vertical position intermittent structures were difficult to identify.

The velocity of the gas structures was observed to increase with both the gas and the liquid superficial velocity. It initially increases with increasing the inclination angle and then decreases after reaching a maximum around approximately 50°. These results came in agreement with the observations of Nicklin et al. (1962), Benjamin (1968), Bendiksen (1984), and Hasan and Kabir (1988) .

A new correlation is proposed to predict the gas structures velocities. This correlation is based on the model of Hasan and Kabir (1988). However, it does not considers C_0 a constant value but rather a function that decreases with increasing Reynolds number. This correlation's predictions were in good agreement with the experimental results across all the inclination angles from horizontal to vertical.

The gas structure frequency was observed to increase with increasing the liquid superficial velocity for all the angles. Analogous to the velocity, the frequency increases with increasing the angle of inclination of the pipe from its horizontal position. This is due to the increase in the number of structures passing through the measuring point, although they become shorter compared to the case at small inclination angles. With increasing the gas superficial velocity three different effects have been observed. Firstly, at 0° inclination the frequency does not show a significant dependency on gas

superficial velocity. Secondly, in inclined pipes, the frequency decreases with increasing gas superficial velocity until it reaches a constant value when the gas superficial velocity rises above 0.7 m/s. Thirdly, in vertical pipes, the frequency was observed to decrease with increasing gas superficial velocity at high liquid superficial velocities whilst it increases at low liquid superficial velocities.

The correlation proposed by Zabaras (1999), based on the model of Gregory and Scott (1969) does not adequately reproduce the frequencies obtained in the present experiments.

A correlation relating the frequency as an implicit function of the Strouhal number with a modified Lockhart-Martinelli parameter is presented. The Strouhal number is calculated using the gas superficial velocity while the Lockhart-Martinelli parameter is modified by adding to the liquid superficial velocity a fictional velocity dependent on the inclination angle of the pipe. This relationship produces predictions that come in good agreement with the experimental data when the gas superficial velocity is greater than 0.7 m/s across all the angles of inclination, from horizontal to vertical position.

CHAPTER 7.

THE INFLUENCE OF THE GAS INJECTOR

7.1 Introduction

One of the geometrical parameters influencing the flow development is the mixer geometry, because it defines the initial interface in between the two phases and induces different initial velocities and momentums to the gas and liquid phase. If air is introduced into the liquid through many small orifices, dispersed bubbles will be generated in the flow. However, if introduced through a single jet of air through a concentric pipe produces a plume with an irregular interface. The initial velocity value of the phase depends on the injection area; a small area induces higher velocities than a large area at a given constant flow rate. Moreover, the orientation of the injector has an influence as well: if a concentric air jet is introduced in the pipe, it would give the flow an axial momentum. The momentum would be zero in case the jet is perpendicular to the pipe, since the radial momentum gets immediately opposed by the walls. The lateral position is significant as well, injectors on the wall or in the centre of the pipe give different initial phase distribution.

It is easy to realise that the gas injection method has a big influence in the liquid-gas interface from observing the vicinity of the mixer. However, once the two phases advance together along the pipe, the divergence decreases. Some studies were carried out to observe the influence of the gas injection on the flow distribution at a certain distance from the inlet investigating different flow regimes. Prasser et al. (2002) studied air-water bubbly flow in a 53 mm diameter pipe using two mixers: 19 capillaries of 0.8 mm diameter and 8 orifices in the pipe wall of 4 mm diameter. Ohnuki and Akimoto

(1996) studied the influence of different mixers in bubble and churn flow in large pipe diameters (480 mm). Gill and Hewitt (1968) and later Brown et al. (1975) performed experiments with air-water in annular flow using two different liquid injections in a 32 mm pipes, but any detailed comparisons have been found in intermittent flows.

7.2 Experimental arrangement

The experiments were performed in the 67 mm rig, described in Chapter 3, fixed in the vertical position. This rig has an exchangeable gas-liquid mixer at the bottom of the test section. Three different mixers were installed in order to study the influence of the gas injection in the development of the flow.

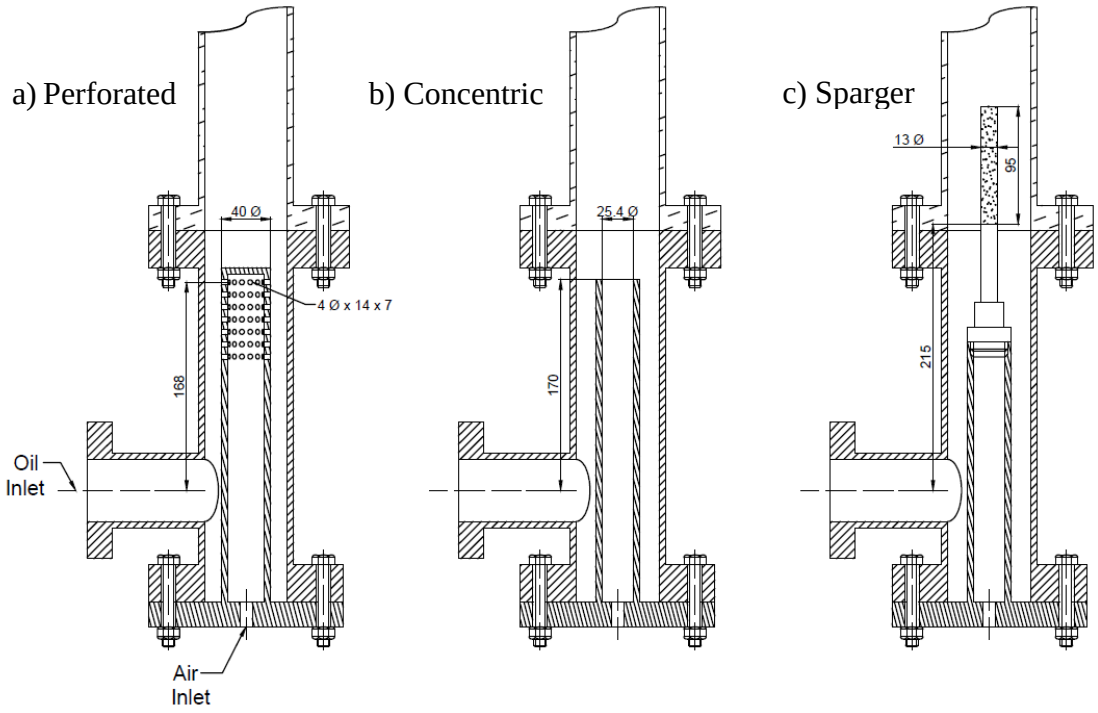


Figure 7.1. Gas Perforated, Concentric and Sparger mixers geometry.

The mixers used were inside a T-junction, where the liquid was introduced by the side arm of the Tee while the air from the rear part. Inside the T-junction, the gas was injected into the liquid phase. In the first mixer, the air is injected through a 25 mm pipe concentric to the test section. The second mixer is composed of a perforated cylinder

with 98 holes, each has a diameter of 4 mm. The last mixer is a porous sintered steel sparger that is 95 mm in length and 13 mm in diameter with pores of 50 µm. Figure 7.1 shows the schematic of the geometry of the three mixers (Perforated, Concentric and Sparger).

The two-phase flow was generated by injecting oil and air at different flow rates. Table 7.1 shows the gas and liquid superficial velocities selected. There are 7 oil superficial velocities combined with 7 air superficial velocities marking an experimental matrix of 49 runs in total. The same flow conditions were reproduced for the three mixers, here and thereafter referred to as: Perforated, Concentric and Sparger; resulting in a total experimental matrix of 7x7x3 runs.

The gas and liquid superficial velocities selected are presented in Figure 7.2 and plotted on Taitel et al. (1980) flow pattern map in the logarithmic scale. Looking at the map, it is expected to encounter bubble, slug and churn flow.

Table 7.1. Gas and liquid superficial velocities used in the experiments.

Liquid superficial velocities, U_{ls} [m/s]						
0	0.016	0.031	0.047	0.23	0.35	0.47
Gas superficial velocities, U_{gs} [m/s]						
0.06	0.17	0.35	0.52	0.70	0.93	1.16

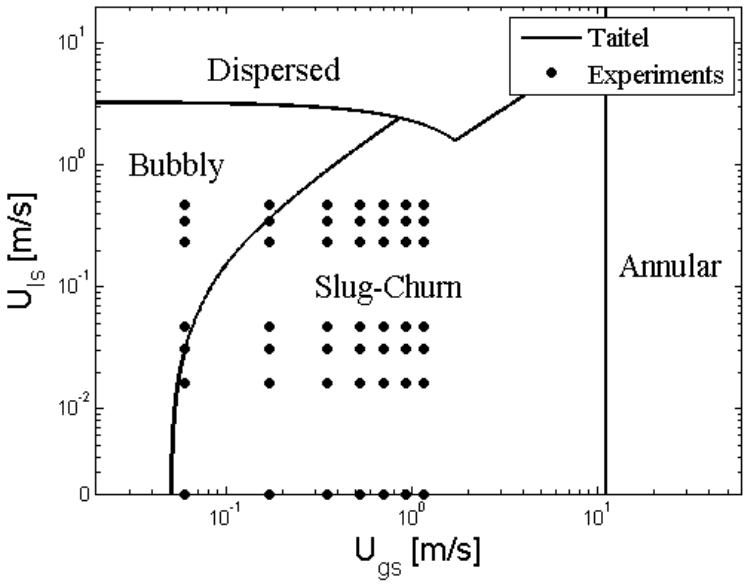


Figure 7.2. Gas and liquid superficial velocities chosen to test plotted on Taitel's (1980) flow patterns map.

7.3 Results and discussion

Visual inspections indicated that the three gas injectors produced different gas distributions in the vicinity of the mixer. The concentric mixer produces a jet of air with an axial momentum at the centre of the pipe that eventually breaks into bubbles. The perforated mixer introduces air in small jets or individual bubbles through the 98 holes close to the wall without inducing initial axial momentum. Moreover, the sparger generates a plume formed with very small bubbles (appear less than 1 mm in size) in the centre of the pipe, with no initial axial momentum observed. These initial gas structures evolve rapidly to the typical two-phase regimes by the breaking up and coalescence mechanism of the gas bubbles. The question posed here is what would the initial phase distribution develop into at 75 diameters length downstream the mixing point, which is the location where the sensors are stationed. To follow this inquest, the two-phase flow was measured at this axial distance for the various combinations of gas and liquid superficial velocities mentioned earlier employing the three mixers. The data gathered were analysed and compared in order to figure out if the flow evolves into the

same structure at 75 diameters. All the methods used to process the data were explained in Chapter 4.

First comparison pursued is for the statistical moments of the void fraction time series. Figure 7.3 shows two graphs: the first compares the average void fraction obtained from WMS and the ECT using the concentric mixer against that by the perforated mixer for all the gas and liquid superficial velocities studied. The second graph depicts the same comparison between the sparger and the perforated mixer. Three lines are shown in both graphs, indicating the perfect agreement and ± 10% deviation. It can be seen that both graphs reflect a very good agreement. The only appreciable divergence appears in the second graph at low gas superficial velocities (0.06 m/s marked by circles in Figure 7.3) where the void fraction given by the sparger is higher than the perforated and therefore higher than the concentric. A similar comparison is presented in Figure 7.4 but using the standard deviation instead of the mean. Again the difference appears only for the sparger at the lowest gas superficial velocity of which the standard deviation is lower. These differences could be explained from the observation of the flow; the sparger produces finely dispersed bubbles behaving like rigid spheres that do not coalesce immediately. On the contrary, the flow from the other mixers evolve rapidly forming small non-spherical bubbles of several millimetres and occasional large cap bubbles. The higher void fraction measured for the sparger at low gas superficial velocities is owed to the fact that small bubbles advance slowly in the riser compared to the larger bubbles produced by other mixers. On the other hand, the lower standard deviation reflected by Figure 7.4 shows that the dispersed bubbly flow does not pose void fraction variations as does the flow with big cap bubbles. This divergence at low gas superficial velocity diminishes once the liquid superficial velocity is high enough to reduce the

number of bubbles coalescing in the perforated and the concentric mixers and produce a flow regime closer to the dispersed bubbly flow.

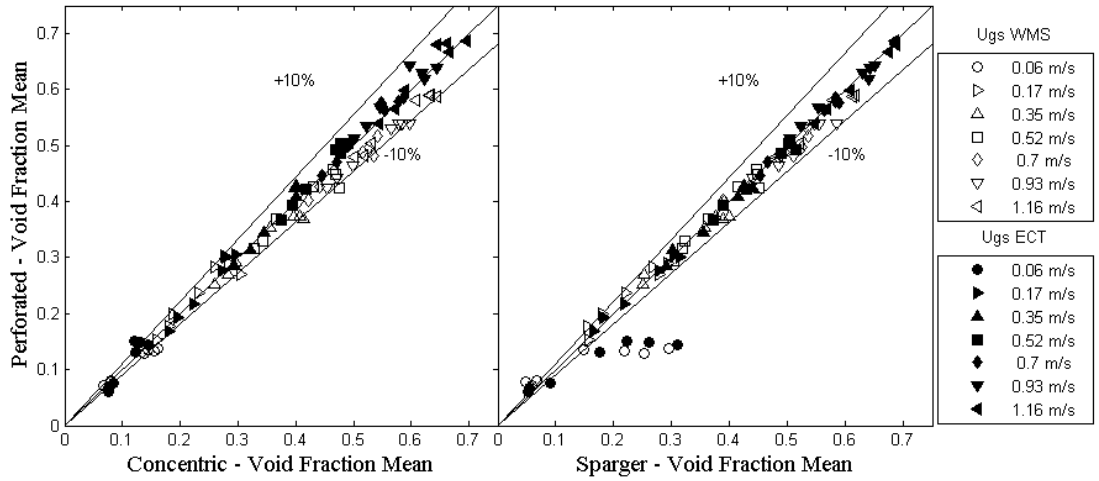


Figure 7.3 Concentric-Perforated and Sparger-Perforated void fraction average comparison for different gas and liquid flow rates using ECT and WMS sensors.

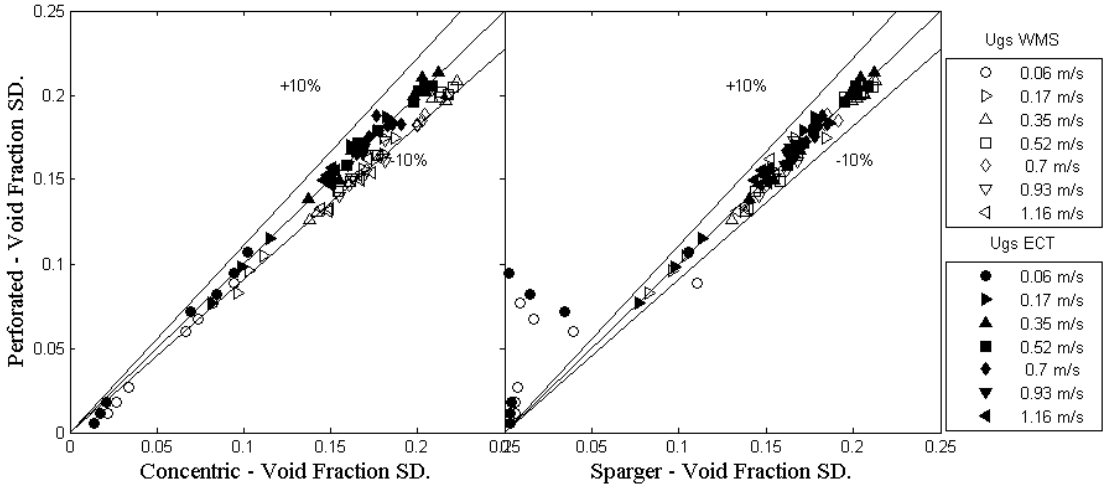


Figure 7.4 Concentric-Perforated and Sparger-Perforated void fraction standard deviation comparison for different gas and liquid flow rates using ECT and WMS sensors.

The earlier results manifest that at low gas superficial velocities the gas injection has a considerable influence on the development of the flow even after a long axial distance from the mixer (75 diameters). However, it cannot yet be established that at higher gas superficial velocities, the flow develops in the same way independent of the gas injection, just because the mean and the standard deviation of the void fraction are

matching. More detailed results of the void fraction distribution can be obtained from the probability density function (PDF) that explains how often each void fraction value would occur. Figure 7.5 shows the PDF of the void fraction obtained using the measurements from the WMS for four representative U_{gs} and U_{ls} values for the three mixers. PDFs for the three mixers overlap with each other for all U_{gs} and U_{ls} with the only exceptions observed at U_{gs}=0.06 m/s and low U_{ls}. In these cases, as explained earlier, the concentric and perforated mixers produce some cap bubbles followed by small dispersed bubbles while the sparger only produce small dispersed spherical bubbles. Again it can be seen that in the first column of graphs, corresponding to U_{gs}=0.06 m/s, that the difference in between the sparger PDF and the PDF corresponding to the other two mixers decrease with increasing the liquid superficial velocity. Figure 7.6 shows this behaviour more clearly, it represents the same as Figure 7.5 but with logarithmic scale on the y-axis.

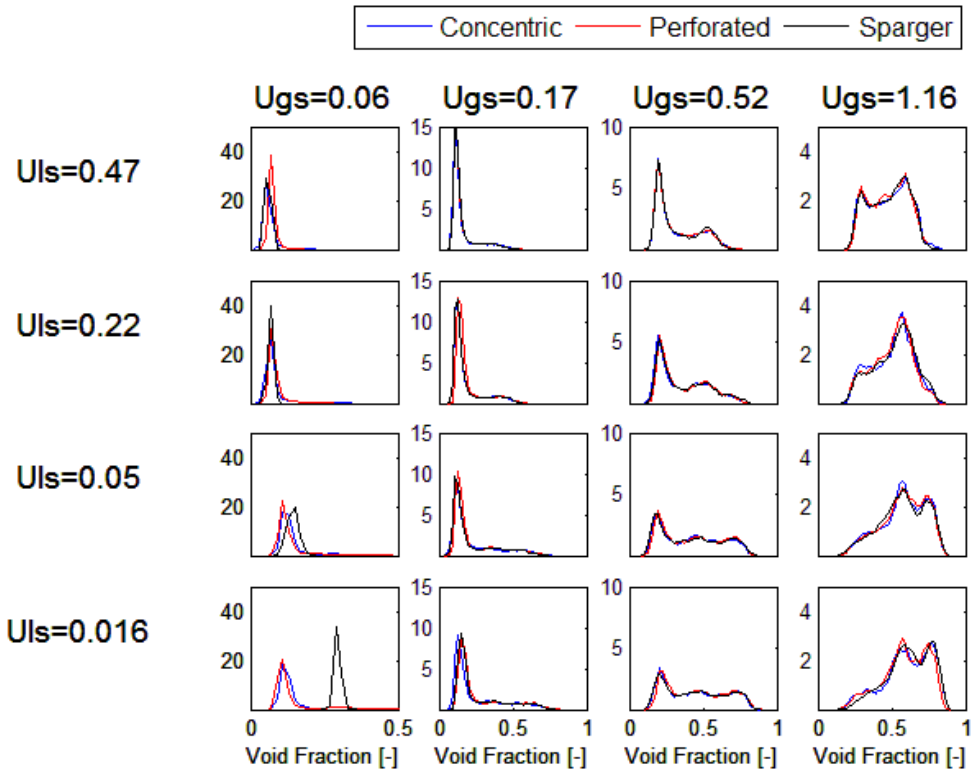


Figure 7.5. Probability Density Function of the void fraction in a cross section of the pipe for different U_{ls}, U_{gs} and gas-liquid mixers.

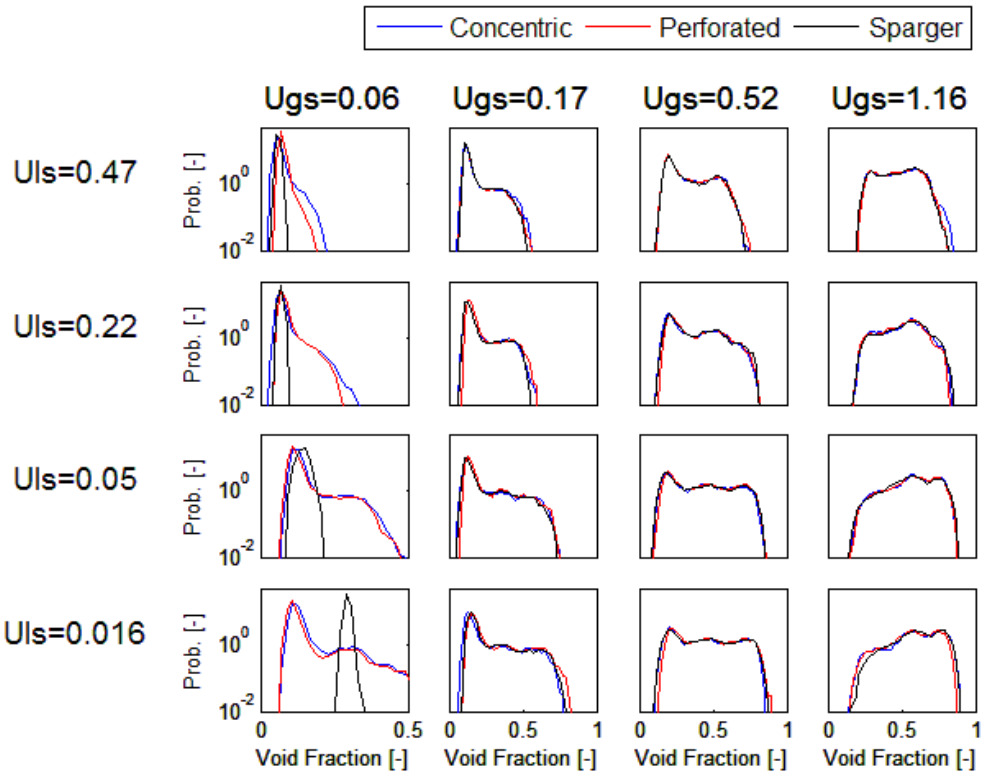


Figure 7.6 Logarithmic Probability Density Function of the void fraction in a cross section of the pipe for different U_{ls}, U_{gs} and gas-liquid mixers.

The PDFs from the Sparger at U_{gs}=0.06 m/s always exhibits a thin peak representing dispersed bubbly flow, this peak moves to lower void fractions with increasing liquid superficial velocity until it overlaps with the peaks of the concentric and perforated mixers. However, the PDFs of the concentric and perforated mixers peak at higher void fractions probabilities that correspond to the big bubbles appearing in the flow.

It has been demonstrated that the void fraction exhibits the same distribution independent of the mixer for gas superficial velocities higher than 0.17 m/s. From this observation, it can be deduced that the flow develops in the same way independent of the initial phase distribution. Nevertheless, there are different axial phase distributions that can produce to the same void fraction PDF. For example, a long and fast bubble could produce the same void fraction measurements during a time period as a short and slow bubble. Furthermore, the concentric mixer injects the air with and initial velocity

while the perforated and sparger mixers do not. For these reasons, one parameter needs to be considered and compared, which is the velocity of the gas structures. Gas structure velocity is measured by cross-correlating the void fraction time series from the dual ECT planes as explained in Chapter 4. The structure velocities obtained for the different injectors are compared in Figure 7.7 as well as in Figures 7.4 and 7.5 in a similar fashion to the void the fraction average and the standard deviation. The agreement exhibited by the perforated and concentric mixer is very good whereby the difference is always lower than 10%. Additionally, a similar agreement is observed between the perforated and the sparger mixers. The only difference is again observed at U_{gs}=0.06 m/s, owing to that the velocity of the big bubbles generated by the perforated mixer is higher than the velocity of the finely dispersed bubbles introduced by the sparger.

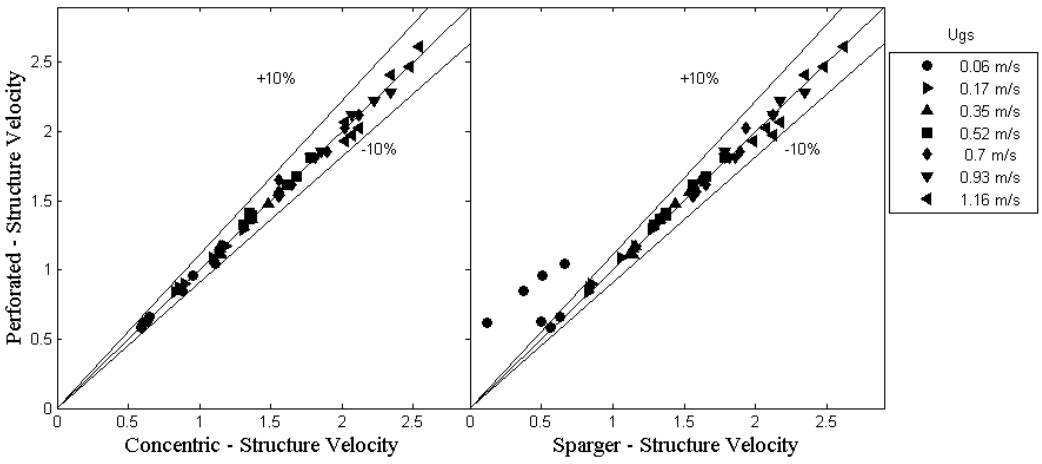


Figure 7.7 Concentric-Perforated and Sparger-Perforated structure velocities comparison for different gas and liquid flow rates using ECT twin plane sensor.

Furthermore, the influence of the injector on the frequency of the gas structures can be considered since one long bubble could produce the same void fraction distribution as two shorter bubbles. The frequency was calculated as the median of the inverse of period of the gas structures (detailed in Chapter 4). Figure 7.8 shows two comparisons of the structures frequency produced by the mixers: the concentric-perforated and sparger-perforated. Again, the results are similar for the Concentric-Perforated while

they differ only at U_{gs}=0.06 for the sparger-perforated case. That is because, in the dispersed bubbly flow caused by the sparger, no significant structure frequency is observed. On the other hand, the perforated and the concentric mixers generate big bubbles that are identifiable as gas structures, whose frequency can be measured.

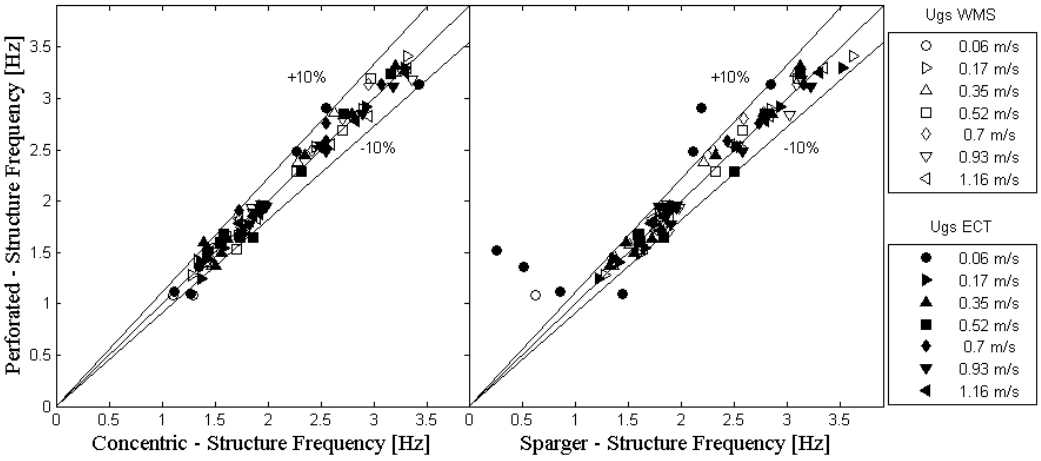


Figure 7.8 Concentric-Perforated and Sparger-Perforated structures frequency comparison for different gas and liquid flow rates using ECT and WMS sensors.

Another characteristic of the intermittent flows is the length of the gas structures. They have been measured by considering the starting point and the end point of the gas structures identified by Hazuku's method (explained in Chapter 4) and then multiplied by the average structure velocity calculated by cross-correlating the signal of the ECT twin planes sensor. The median of these lengths of structures is calculated for all the gas and liquid superficial velocities and mixers. Figure 7.9 compares the structure lengths obtained from the three mixers using the data from both WMS and ECT sensors. It can be seen the results are very similar to the concentric and the perforated mixer while they differ for the sparger and perforated mixer at low gas superficial velocity. That difference is referred to the gas structures generated by the sparger at these conditions are spherical bubbles that are much smaller than the cap bubbles produced by the perforated and concentric mixers.

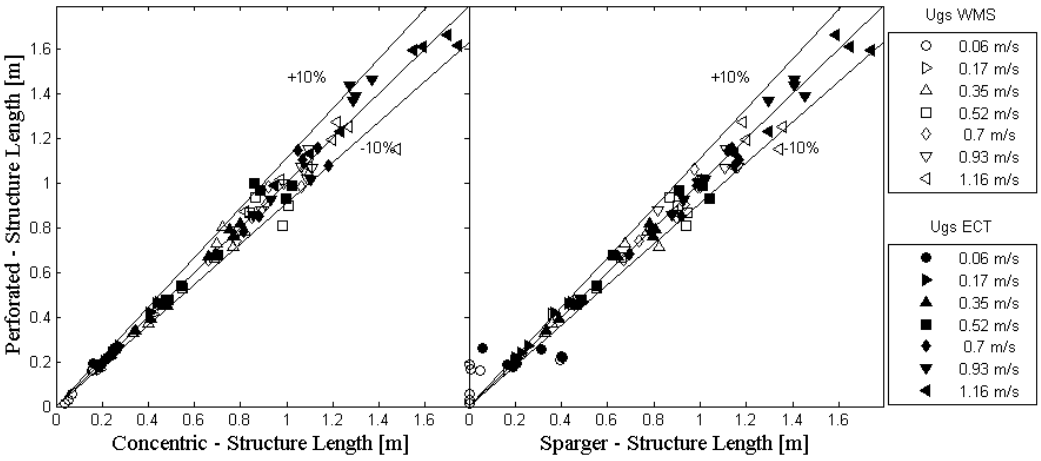


Figure 7.9 Concentric-Perforated and Sparger-Perforated structures length comparison for different gas and liquid flow rates using ECT and WMS sensors.

Another parameter investigated is the average radial distribution of the void fraction because the void fraction time series cannot distinguish if the gas moves in the centre of the pipe or next to the wall. Figure 7.10 presents the average void fraction distribution along the radius of the pipe for different gas and liquid superficial velocities for the three mixers. Each mixer is represented by a different colour line. It is evident that the three lines overlap at gas superficial velocities higher than 0.17 m/s and that some differences are appreciable at U_{gs}=0.06 m/s. The first difference is observed at U_{gs}=0.06 m/s and U_{gl}=0.016 m/s, whereby the concentric and perforated mixers produce a core peak distribution due to the big bubbles travelling on the centre pipe. Meanwhile, the sparger generates a uniform distribution of fine dispersed bubbles. Then, with increasing the U_{gl} to 0.22 m/s, a significant change in the void fraction radial distribution is observed for the perforated mixer and the sparger (red and black lines); the distribution presents a wall peak in both cases. However, for the concentric mixer, a core peak distribution is observed. This behaviour persists as is becomes more significant once the U_{ls} is increased up to 0.47 m/s

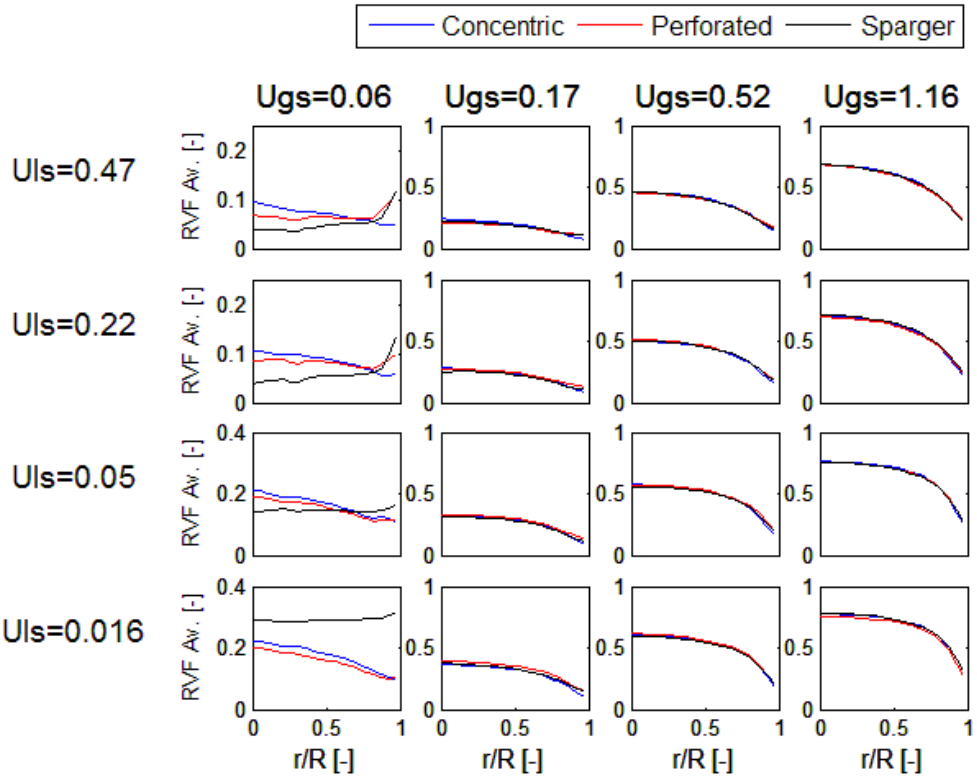


Figure 7.10. Radial distribution average of the void fraction in a cross section of the pipe for different U_{ls}, U_{gs} and gas-liquid mixers.

Finally, the void fraction distribution for clusters of bubbles with different diameters is computed (this kind of distributions are explained in detail in Chapter 4). Figure 7.11 compares these distributions obtained using the three mixers at different gas and liquid superficial velocities. The three lines, each line corresponds to a mixer, perfectly overlap when the gas superficial velocity is 0.17 m/s or higher. When it is equal to 0.06 m/s only the sparger (black line) shows discrepancies at low liquid superficial velocity. The difference is that the void fraction distribution is concentrated in bubbles of smaller diameter, that is represented in the graph as a high single peak at small bubble diameters in comparison to the concentric and perforated mixer lines that have a smaller peak with a tail towards larger bubble diameters.

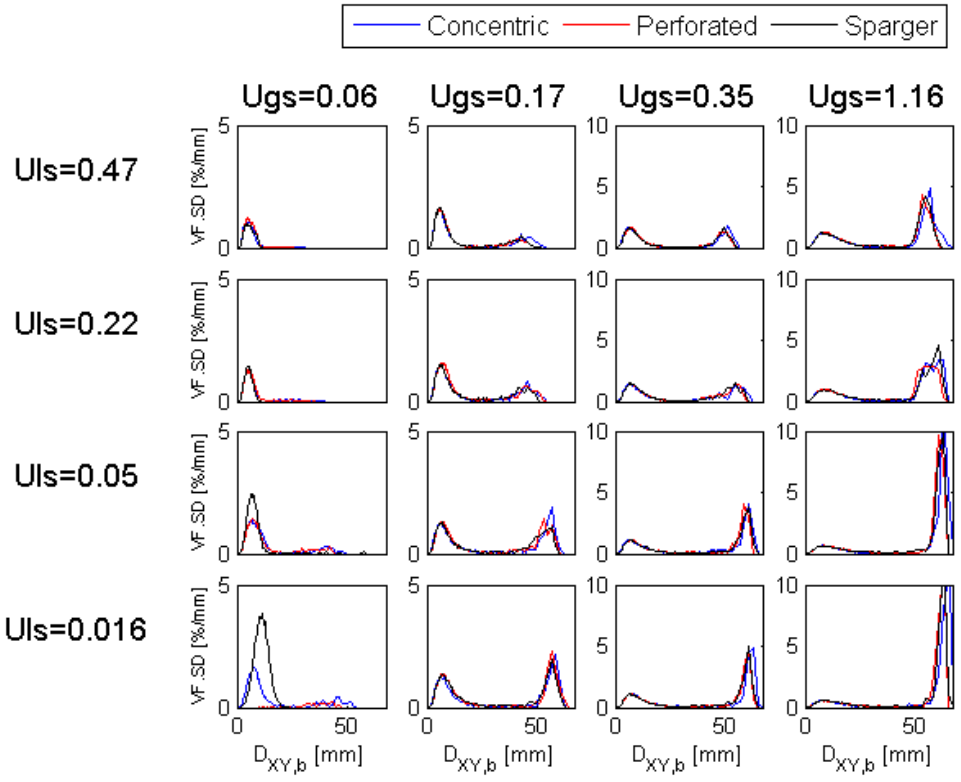


Figure 7.11. Distribution of the void fraction to clusters of bubbles of different bubbles sizes at selected values of U_{ls}, U_{gs} while using the three gas-liquid mixers.

7.4 Conclusions

The investigations carried out in this chapter suggests that oil–air multiphase flow develops in the same way at 75 diameter axial distance from the mixing point independent of the gas injection method at gas superficial higher than 0.17 m/s. This conclusion is reached since the mean and the standard deviation of the void fraction in the cross-section of the pipe, the velocity, frequency, and the length of the gas structures did not reflect an appreciable divergence when different mixers producing completely different phase distributions at the base of the test pipe are employed. Additionally, the PDFs and the average radial void fraction distribution profiles as well as the void fraction distribution to clusters of bubbles with varying diameters were found to be virtually identical. The discrepancies were always less than 10% and centred in zero reflecting no general trend indicating higher or lower values.

On the other hand, significant differences were observed at gas superficial velocities lower or equal to 0.06 m/s. The sparger mixer produces at these gas superficial velocities a fine dispersion of bubbles that do not coalesce to form bigger bubbles within the observed pipe length (5 m). These fine bubbles are highly influenced by the liquid superficial velocity (U_{ls}). The lateral distribution of void fraction revealed that these bubbles are distributed equally across the pipe diameter at U_{ls} lower than 0.05 m/s while they evolve into a wall peaking distribution at U_{ls} higher than 0.22 m/s. On the other hand, the concentric and the perforated mixers generate cap bubble flow in which intermittent big bubbles appear after the coalescence of small bubbles has taken place. The size and number of these big bubbles seem to decrease with increasing the liquid superficial velocity. Higher liquid flow drags the bubbles upwards once they are introduced into the pipe reducing the coalescence rate into bigger bubbles. This effect is more profound for the perforated mixer since the bubbles are introduced across 98 holes compared to the concentric mixer. As a result, at $U_{ls} > 0.22$m/s, it was found that big bubbles produced by the concentric mixer are larger than the big bubbles generated by the perforated mixer. Another notable effect is that at $U_{ls} > 0.22$ m/s core peaking radial distribution profile prevails when using the concentric mixer whilst wall peaking is reflected by the perforated mixer profile. With increasing the liquid superficial velocity the big bubbles produced by concentric and perforated injectors start to break down into small dispersed bubbles, the flow behaviour grows closer to that produced by the sparger mixer.

CHAPTER 8.

GENERAL DISCUSSIONS AND CONCLUSIONS

8.1 Introduction

The general discussions and the conclusions drawn from the different chapters of this thesis are presented in this chapter.

In the Chapter 5 the influence of the diameter of the pipe on the velocity and the frequency of the gas structures in intermittent flows was discussed. Following the analysis of the experimental results, a model to predict the velocity of the gas structures was developed. Additionally, a correlation to predict the frequency of the gas structures was proposed. In Chapter 6 a similar analysis was presented to investigate the influence of the inclination angle on the velocity and frequency of the gas structures. Two expressions, one to calculate the velocity and another to calculate the frequency of the gas structures at different angles of inclination of the pipe, were proposed.

In this chapter, the model proposed to calculate the velocity as a function of the diameter of the pipe and the other that is a function of the angle of inclination are combined in a single equation. A similar exercise is performed with the frequency models. The resultant equations must satisfy the experimental results presented in Chapters 5 and 6. These experimental results include the velocity and the frequency for intermittent two-phase flows generated at different gas and liquid superficial velocities, in 67 and 127 mm diameter pipes, and at a different angles of inclination from the horizontal to the vertical position. Moreover, the proposed models will also be tested against results extracted from the literature for different pipe diameters, distance from the mixing point, flow velocities, and fluids with different physical properties.

In the second part of this chapter, the main conclusions drawn from Chapters 5, 6 and 7 are summarised combined by general conclusions. Finally, recommendations for future work to improve and expand on the findings of this thesis are suggested.

8.2 General discussions

8.2.1 Velocity of the gas structures

The correlations proposed in Chapters 5 and 6 to calculate the velocity of the gas structures as a function of the pipe diameter and as a function of the angle of inclination of the pipe are based on the drift flux approach. Expressions to calculate the distribution coefficient, C_0, and the drift velocity, V_d, are developed. The distribution coefficients are presented as a negative power law of Reynolds number calculated using the liquid phase moving at the mixture velocity in Chapters 5 and 6. The fitting parameters of these equations *C* and *n* from both chapters (Table 5.5 and Table 6.6) appear to be very similar. On the other hand, the drift velocity is presented as a function of the diameter of the pipe in Chapter 5 (equation [5.8]) and as a function of the inclination angle in Chapter 6 (equation [6.7]). Combining these equations ([5.8] and [6.7]), the velocity of the gas structures as a function of the diameter and the angle of inclination can be expressed as:

$$V_b = C\ Re_l^{-n}\ U_{ms} + A\sqrt{\sin\alpha}\,(1+\cos\alpha)^{1.2}\,D \qquad [8.1]$$

Where U_{ms} is the mixture velocity, Re_l is the Reynolds number of the liquid phase moving at the mixture velocity, α is the angle of inclination of the pipe, *D* is the diameter of the pipe and *C*, *A* and *n* are fitting parameters. The fitting parameters adjusted to the experimental results and their determination coefficient are shown in Table 8.1.

Table 8.1. Fitting parameters and corresponding determination coefficient.

Angle, α	Diameters	C	N	A [s^{-1}]	R^2
0 - 90	67 and 127 mm	10.77	0.212	5.861	0.953

The final correlation with the fitting coefficients is presented in equation [8.2]. This correlation predicts the velocity of the gas structures as a function of Reynolds number, the mixture velocity, the diameter of the pipe and the angle of inclination. There are a number of particularities to be considered with this correlation compared to other models published in the literature. First, it is developed from a drift flux model where the distribution coefficient C_0, which is a function of Reynolds number, decreases with increasing the turbulence of the flow. And second, the drift velocity is considered to be zero in horizontal pipes as explained in Chapter 6.

$$V_b = 10.77\ Re_l^{-0.212}\ U_{ms} + 5.861[s^{-1}]\ \sqrt{\sin\alpha}\,(1+\cos\alpha)^{1.2}\ D \qquad [8.2]$$

The agreement with the experimental results is displayed in Figures 8.1 and 8.2. The values of the gas structure velocities reported in Chapter 5 are plotted against the predicted values using equation [8.2] in Figure 8.1. In a similar fashion, the results of Chapter 6 are plotted in Figure 8.2. It can be seen that a very good agreement is reflected by both figures. The data shown in Figure 8.1 represents different combinations of gas and liquid superficial velocities varying from 0.17 to 2.32 m/s and 0.115 to 0.47 m/s respectively, in two different pipe diameters: 67 and 127 mm. On the other hand, Figure 8.2 presents values corresponding to gas and liquid superficial velocities ranging from 0.17 to 1.74 m/s and 0.023 to 0.47 m/s respectively, for different angle of inclination of the pipe from the horizontal to vertical orientation in steps of 15 °.

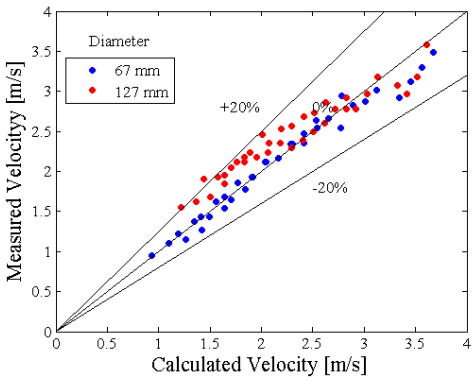


Figure 8.1. Comparison of the experimental gas structure velocity against the predicted values at different U_{gs} and U_{ls} in 67 and 127 diameter vertical pipes.

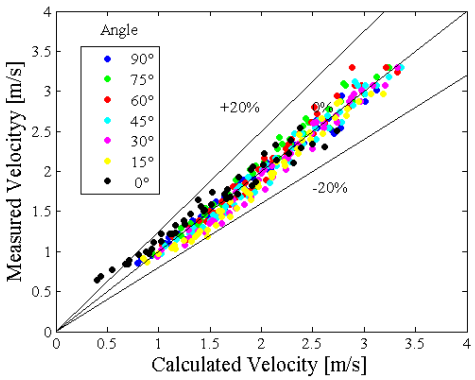


Figure 8.2. Comparison of the measured values against the predicted values at different U_{gs} and U_{ls} in a pipe of 67 mm diameter positioned at different inclinations as per the legend.

The proposed correlation must be further validated against data collected from the literature. Two cases were selected here from the few that are published: Van Hout et al. (2003) and Hernandez-Perez (2008). Van Hout et al. (2003) measured the velocity of the gas structures at different angles in pipes of 24 and 54 mm diameter using air and water. Later on, Hernandez-Perez (2008) presented a considerable amount of results in an inclinable rig of 38 mm in diameter using air and water as well. The experimental conditions of the studies of these authors and the conditions considered in the present experiments are summarised in Table 8.2. The table shows the fluids used, the diameter of the test pipe, the measuring distance from the mixing point expressed in diameters length, and the range of liquid and gas superficial velocities considered.

Table 8.2. Experimental conditions of the present experiments as well as those of Hernandez-Perez (2008) and (Van Hout et al., 2003).

	Fluids	D [mm]	L/D	Liq. R [m/s]	Gas R [m/s]
Present	Air-Oil	67	75	0.115-0.47	0.17-1.74
Hernandez (2008)	Air-Water	38	132	0.04-0.73	0.15-3.04
Van Hourt et al. (2003)	Air-Water	24	118	0.01-0.1	0.41-0.63
Van Hourt et al. (2003)	Air-Water	54	89	0.01-0.1	0.41-0.63

Figure 8.3 compares the results of Hernandez-Perez (2008) with the results obtained using the equation [8.2] under the same conditions. It can be seen that a good agreement is obtained at all the angles of inclination. Although experimental points on the plot present a scattering, yet they are all aligned at all the different inclination angles considered, from vertical to horizontal. The model seems to slightly under predict the experimental results. It must be considered that Hernandez used water in his experiments whilst the present correlation is developed from experiments employing oil of viscosity 5 times greater than that of the water. It must be said that the viscosity of the fluid was not included in the derivation of the drift velocity in the present model. Therefore, a new term considering the viscosity effect should be incorporated in the calculation of the drift velocity. However, this is out of the scope of this work which is only centred on the influence of geometrical parameters.

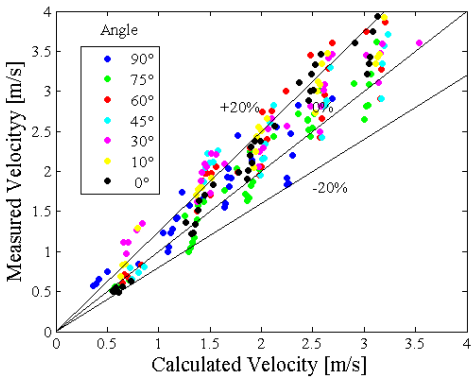


Figure 8.3. Comparison of experimental results of Hernandez-Perez (2008) with the values calculated using the correlation [8.2].

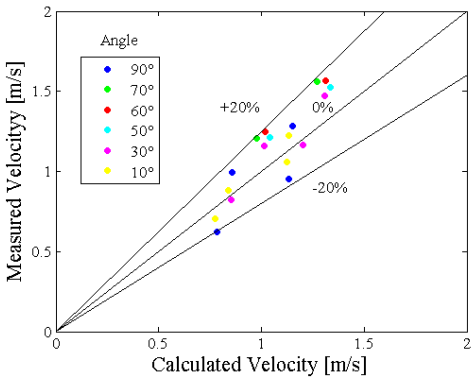


Figure 8.4. Comparison of experimental results of Van Hout et al. (2003) with the values calculated using the correlation [8.2].

Figure 8.4 depicts the experimental results of Van Hout et al. (2003) against the predictions of the correlation [8.2] . Van Hout used pipes of diameters of 24 and 54 mm, which are smaller than the 67 mm employed in the present experiments. Even though the agreement obtained is good, whereby most values cluster around 0% difference to a maximum discrepancy of 20% for all experimental conditions considered.

8.2.2 Frequency of the gas structures

Two correlations to predict the frequency of the gas structures are proposed in Chapter 5 and Chapter 6. One is a function of the diameter of the pipe and the other is a function of the angle of in inclination of the pipe. Both relate the Strouhal number, calculated using the gas superficial velocity as the flow velocity, and a modified version of the Lockhart-Martinelli parameter. The modification of the parameter consists of adding a term to the liquid superficial velocity. The term is a fictional value that represents the liquid which is contained in the pipe that cannot be drained by the gas when it pushes the liquid outside the pipe. This fictional term reaches the maximum when the pipe is in the vertical position while decreases with decreasing the angle of inclination reaching a value of zero in horizontal pipes. In horizontal pipes, the liquid is not held in the pipe by the action of the gravity; therefore it can be completely cleared out of the pipe by the gas registering a frequency equals to zero. The correlation proposed in Chapter 5, equation [5.13], is fitted to the experimental data obtained in the 67 and 127 mm pipes while at the vertical position. On the other hand, the expression given in Chapter 6, equation [6.17], is based on experiments performed in a 67 mm pipe at different angles of inclination ranging from the horizontal to the vertical position. Combining both formulations, it is expected that a general expression will be obtained in the form of:

$$f = \mathrm{A}\,\frac{B \cdot U_{ls} + (1 + (\sin\alpha)^{0.7} - (\cos\alpha)^{0.3})}{D}\sqrt{\frac{\rho_l}{\rho_g}} \qquad [8.3]$$

The coefficients A and B are evaluated now considering the experimental data of Chapter 5 (at different pipe diameters) and Chapter 6 (at different angles of inclination) together. They are presented in Table 8.3 together with the corresponding coefficient of determination. The fitting is reasonably agreeable with R^2 =0.953.

Table 8.3. Fitting parameters and determination coefficient for the frequency correlation.

Angle, α	Diameters	A	B	R^2
0 - 90	67 and 127 mm	0.0024	2.065	0.953

Finally, the correlation to calculate the frequency of the gas structures that considers both the diameter of the pipe and the angle of inclination can be written as:

$$f = 0.0024 \frac{2.065 \cdot U_{ls} + (1 + (\sin\alpha)^{0.7} - (\cos\alpha)^{0.3})}{D} \sqrt{\frac{\rho_l}{\rho_g}} \qquad [8.4]$$

The experimental results at different pipe diameters are plotted against calculated values using the expression [8.4] in Figure 8.5. Similarly, the experimental results for different angles of inclination are plotted against the predictions of the model above in Figure 8.6. It can be seen that equation [8.4] produce satisfactory predictions for both sets of data, considering both the diameter and the inclination angle of the pipe. I can be observed that the discrepancy is rarely more than 20%.

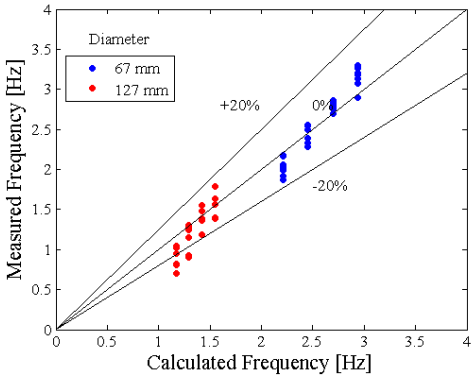


Figure 8.5. Comparison of the experimental frequency against that predicted by the new model at different U_{gs} and U_{ls} in 67 and 127 diameter vertical pipes.

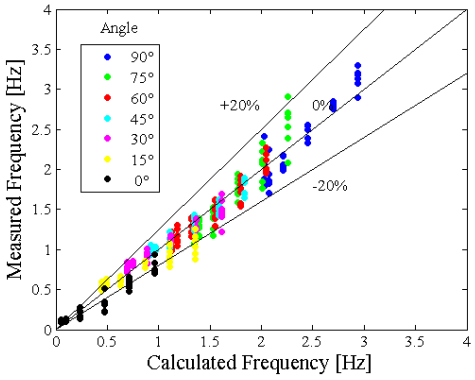


Figure 8.6. Comparison of the measured frequency values against the predicted values at different U_{gs} and U_{ls} in a pipe of 67 mm diameter with different inclinations.

The performance of the correlation developed here is investigated against data collected from the literature as well. Table 8.4 summarises the experimental conditions of

experiments produced by different authors. Zheng and Che (2006) performed experiments in a 35 mm vertical pipe using air and water. Cheng and Burkhardt (2003) carried out experiments in a 150 mm pipe employing air and water too. These two particular investigations are selected from the literature to test the performance in a smaller pipe diameter and in another larger with respect to the ones employed in the present experiments (67 and 127). On the other hand, the performance of the present correlation [8.4] is also compared to the data of Van Hout et al. (2003) who carried out experiments in an inclined 54 mm pipe using air and water, a similar size to the 67 mm diameter pipe used in the present experiments.

Table 8.4. Experimental conditions of the present experiments and the ones of Cheng and Burkhardt (2003), Zheng and Che (2006), and (Van Hout et al., 2003).

	Fluids	D [mm]	L/D	Orientation	Liq. R [m/s]	Gas R [m/s]
Present	Air-Oil	67	75	Vertical	0.115-0.47	0.17-2.32
Present	Air-Oil	127	85	Vertical	0.115-0.47	0.7-2.32
Zheng and Che (206)	Air-Water	35	100	Vertical	0.35-0.78	0.15-0.45
Cheng and Burkhardt (2003)	Air-Water	150	48	Vertical	0-1.85	0.03-1.66
Present	Air-Oil	67	75	Inclined	0.05-0.5	0.7-2.32
Van Hout et al (2003)	Air-Water	54	89	Inclined	0.01-0.21	0.13-0.63

Figure 8.7 compares the correlation with the data from vertical pipes with different diameters: 35 mm (Cheng and Burkhardt, 2003), 67 mm (present), 127 mm (present) and 150 mm (Zheng and Che, 2006). Regarding the present data, the correlation works well because the fitting parameters of the correlation are adjusted to them. However, the correlation appear to overpredict the frequency in smaller diameter pipes while under predict that of larger diameter pipes. This observation suggests that the frequency is not inversely proportional to the diameter of the pipe but follows a non-linear expression as already modelled by other authors (Greskovich and Shrier, 1972,

Heywood and Richardson, 1979, Legius et al., 1997, Kaji et al., 2009). However, that can be approximated to an inversely proportional expression when the pipe diameter is between 67 and 127 millimetres.

In Figure 8.8 the frequency results obtained by Van Hout et al. (2003) are plotted against the values calculated using the correlation [8.4]. It can be seen that there is a good agreement at small inclination angles (close to the horizontal position), while the correlation seem to over predict the experimental results with increasing the angle of inclination. This discrepancy could be explained considering the factors that influence the calculations. First is that the frequency is considered by the present correlation inversely proportional to the diameter of the pipe and it is not as explained earlier on. Moreover, the correlation overpredicts the experimental results for pipes of diameters smaller than 67 mm. Secondly, the viscosity of the liquid has an influence on the frequency of the gas structures. Van Hout et al (2003) used water which has a viscosity five times lower than that of the oil employed in the present work. Finally, the discrepancy can be inherent in the method executed to calculate the frequency; in vertical pipes, the gas structures are very irregular whereby different methods could be used to identify the frequency which can differ from one method to another.

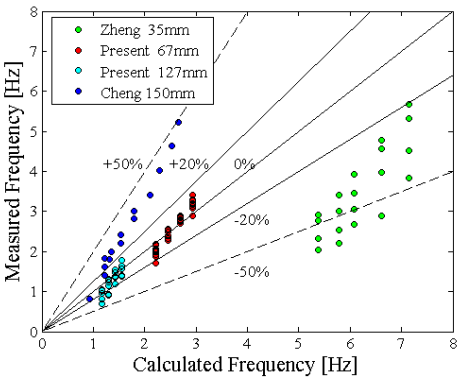


Figure 8.7. Comparison of experimental frequency of Cheng and Burkhardt (2003) and Zheng and Che (2006) against the predicted values by equation [8.4].

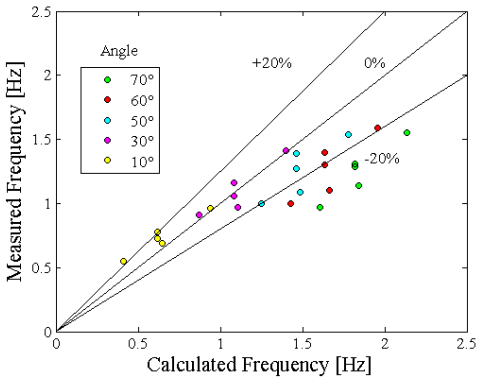


Figure 8.8. Comparison of experimental results of Van Hout et al. (2003) against the values predicted by equation [8.4].

8.3 General conclusions

Slug flow is inherently an intermittent flow, while bubble and churn flow can sometimes be considered intermittent when at a fixed observation point in the pipe, a gas dominated structure followed by a liquid dominated structure appear in a repeated manner a certain characteristic mean frequency.

The experimental investigations presented in this thesis suggest that the velocity of the gas structures increases with both the gas and the liquid superficial velocities. However, it decreases with the diameter of the pipe at low mixture velocities (U_{ms} > 1 m/s). With increasing the angle of inclination of the pipe, the velocity of the gas structures increases until it reaches a maximum around 50° above which it decreases.

A correlation is proposed to predict the velocity of the gas structures as a function of the gas and liquid superficial velocities, the Reynolds number of the liquid phase, the diameter of the pipe, and the angle of inclination. The correlation predictions are in good agreement with the data extracted from the present experiments. Its performance

is also tested against data collected from the literature, an acceptable agreement is obtained.

The frequency of the gas structures is found to increase with increasing the liquid superficial velocity. Contrarily, it is observed to decrease with increasing gas superficial velocity until it stabilises to a constant value around U_{gs} = 0.7 m/s. The frequency decreases as well with increasing the diameter of the pipe. Finally, the frequency was found to increase with increasing the inclination angle of the pipe, minimum at horizontal position and maximum at the vertical position.

A correlation is proposed to predict the frequency in two-phase intermittent flows where the frequency can be considered independent of the gas superficial velocity, in the present data this occurs when U_{gs} > 0.7 m/s. The proposed correlation is a function of the liquid superficial velocity, the diameter of the pipe, the angle of inclination, and the densities of the both fluids. The correlation was found to satisfactorily reproduce the experimental data of the present work. Some differences discrepancies are observed when the performance is contrasted against experimental data from the literature performed in a different range of pipe diameters and liquids with different viscosities.

The characteristics of the intermittent gas-liquid two-phase flows at 75 diameter length from the mixing point is found to be independent of the entrance effect.

A large amount of data (more than 600 runs) of gas-liquid intermittent flow have been collected using two different measurement techniques (ECT and WMS). The conditions at which this data has been obtained reproduce the conditions of oil wells and oil pipelines featuring large diameter pipes, liquids more viscous than water, and different angles of inclination of the pipe. This type of data is rather scarce in the literature,

therefore, oil industries demonstrated great interest by sponsoring this project in order to validate their models and simulation codes.

8.4 Recommendations for future work

The experiments in the present work were performed in two vertical pipes; one is 67 mm and the other is 127 mm to observe the influence of the diameter on the development of intermittent flows. Additionally, a second campaign was performed in the 67 mm pipe at different angles of inclination to investigate the influence of the angle of inclination on flow characteristics. No experiment was performed at different angles in the 127 mm pipe. It was assumed that the angle of inclination has the same influence on the 127 mm pipe to that observed in the 67 mm pipe. To complete the experimental matrix a new campaign must be carried out at different angles of inclination using a larger diameter pipe.

From the present data of the 67 and 127 mm pipes, it was observed that the frequency of the gas structures is inversely proportional to the diameter of the pipe. But this proportionality does not agree with the data from the literature where the pipes are smaller than 67 mm or larger than 127 mm. More experiments using different pipe diameters must be performed to determine more precisely how the frequency of the gas structure varies with the diameter of the pipe.

The scope of this thesis has been to study the influence of geometrical parameters on the development of intermittent flows. However, physical parameters must also be considered as well, since they dramatically influence flow characteristics. Further experimentation using liquids with different viscosities and gases with different densities will certainly broaden the understanding of the intermittent flows.

REFERENCES

ABDULAHI, A. 2014. *Investigating the effect of liquid viscosity on two-phase gas-liquid flows.* University of Nottingham.

ABDULKADIR, M., HERNANDEZ-PEREZ, V., LOWNDES, I., AZZOPARDI, B. & SAM-MBOMAH, E. 2016. Experimental study of the hydrodynamic behaviour of slug flow in a horizontal pipe. *Chemical Engineering Science,* 156**,** 147-161.

ABDULKAREEM, L. A. 2011. *Tomographic investigation of gas-oil flow in inclined risers.* University of Nottingham.

ALI, S. F. & YEUNG, H. 2014. Two-phase flow patterns in large diameter vertical pipes. *Asia-Pacific Journal of Chemical Engineering,* 9**,** 105-116.

ALVES, I. N., SHOHAM, O. & TAITEL, Y. 1993. Drift velocity of elongated bubbles in inclined pipes. *Chemical Engineering Science,* 48**,** 3063-3070.

AZZOPARDI, B. 1997. Drops in annular two-phase flow. *International Journal of Multiphase Flow,* 23**,** 1-53.

AZZOPARDI, B. J., ABDULKAREEM, L. A., ZHAO, D., THIELE, S., DA SILVA, M. J., BEYER, M. & HUNT, A. 2010. Comparison between Electrical Capacitance Tomography and Wire Mesh Sensor Output for Air/Silicone Oil Flow in a Vertical Pipe. *Industrial & Engineering Chemistry Research,* 49**,** 8805-8811.

AZZOPARDI, B. J., IJIOMA, A., YANG, S., ABDULKAREEM, L. A., AZZI, A. & ABDULKADIR, M. 2014. Persistence of frequency in gas–liquid flows across a change in pipe diameter or orientation. *International Journal of Multiphase Flow,* 67, Supplement**,** 22-31.

BENDIKSEN, K. H. 1984. An experimental investigation of the motion of long bubbles in inclined tubes. *International Journal of Multiphase Flow,* 10**,** 467-483.

BENJAMIN, T. B. 1968. Gravity currents and related phenomena. *Journal of Fluid Mechanics,* 31**,** 209-248.

BRATLAND, O. 2010. Pipe Flow 2: Multi-phase Flow Assurance. *Ove Bratland*.

BRENNEN, C. E. 2005. *Fundamentals of multiphase flow,* Cambridge University Press.

BROWN, D., JENSEN, A. & WHALLEY, P. 1975. *Non-equilibrium effects in heated and unheated annular two-phase flow,* American Society of Mechanical Engineers.

BYARS, M. 2001. Developments in Electrical Capacitance Tomography.

CHENG, D.-C. & BURKHARDT, H. 2003. Bubble tracking in image sequences. *International journal of thermal sciences,* 42**,** 647-655.

COSTIGAN, G. & WHALLEY, P. B. 1997. Slug flow regime identification from dynamic void fraction measurements in vertical air-water flows. *International Journal of Multiphase Flow,* 23**,** 263-282.

DA SILVA, M., DOS SANTOS, E., HAMPEL, U., RODRIGUEZ, I. & RODRIGUEZ, O. 2011. Phase fraction distribution measurement of oil–water flow using a capacitance wire-mesh sensor. *Measurement Science and Technology,* 22**,** 104020.

DA SILVA, M., SCHLEICHER, E. & HAMPEL, U. 2007. Capacitance wire-mesh sensor for fast measurement of phase fraction distributions. *Measurement Science and Technology,* 18**,** 2245.

DAVIES, R. & TAYLOR, G. The mechanics of large bubbles rising through extended liquids and through liquids in tubes. Proceedings of the Royal Society of London A: Mathematical, Physical and Engineering Sciences, 1950. The Royal Society, 375-390.

DUMITRESCU, D. T. 1943. Strömung an einer Luftblase im senkrechten Rohr. *ZAMM-Journal of Applied Mathematics and Mechanics/Zeitschrift für Angewandte Mathematik und Mechanik,* 23**,** 139-149.

ESCRIG, J., HEWAKANDAMBY, B., DIMITRAKIS, G. & AZZOPARDI, B. 2016. Influence of Inclination Angle on Intermittent Two Phase Flows. V01BT28A002.

FOSSA, M., GUGLIELMINI, G. & MARCHITTO, A. 2003. Intermittent flow parameters from void fraction analysis. *Flow Measurement and Instrumentation,* 14**,** 161-168.

FRECHOU, D. 1986. *Étude de l'écoulement vertical ascendant à trois fluides en conduite verticale*, Technip.

GALLENI, F. & ISSA, R. I. 2015. LINEAR STABILITY ANALYSIS OF THE DISCRETIZED ONE-DIMENSIONAL TWO-FLUID MODEL EQUATIONS FOR SLUG CAPTURING IN VERTICAL FLOW. 27**,** 215-227.

GILL, L. & HEWITT, G. 1968. Sampling probe studies of the gas core in annular two-phase flow-III distribution of velocity and droplet flowrate after injection through an axial jet. *Chemical Engineering Science,* 23**,** 677-686.

GREGORY, G. & SCOTT, D. 1969. Correlation of liquid slug velocity and frequency in horizontal cocurrent gas-liquid slug flow. *AIChE Journal,* 15**,** 933-935.

GRESKOVICH, E. J. & SHRIER, A. L. 1972. Slug Frequency in Horizontal Gas-Liquid Slug Flow. *Industrial & Engineering Chemistry Process Design and Development,* 11**,** 317-318.

HADAMARD, J. 1923. *Lectures on Cauchy's Problem in Linear Partial Differential Equations*, Yale University Press.

HARMATHY, T. Z. 1960. Velocity of large drops and bubbles in media of infinite or restricted extent. *AIChE Journal,* 6**,** 281-288.

HASAN, A. R. & KABIR, C. S. 1988. Predicting multiphase flow behavior in a deviated well. *SPE Production Engineering,* 3**,** 474-482.

HAZUKU, T., TAKAMASA, T. & MATSUMOTO, Y. 2008. Experimental study on axial development of liquid film in vertical upward annular two-phase flow. *International Journal of Multiphase Flow,* 34**,** 111-127.

HERNANDEZ-PEREZ , V. 2008. *Gas-liquid two-phase flow in inclined pipes.* University of Nottingham.

HERNANDEZ-PEREZ, V., ABDULKADIR, M. & AZZOPARDI, B. 2010. Slugging frequency correlation for inclined gas–liquid flow. *World Acad. Sci., Eng. Technol,* 6**,** 44-51.

HEWITT, G. F. & ROBERTS, D. 1969. Studies of two-phase flow patterns by simultaneous X-ray and flash photography. DTIC Document.

HEYWOOD, N. & RICHARDSON, J. 1979. Slug flow of air—water mixtures in a horizontal pipe: Determination of liquid holdup by γ-ray absorption. *Chemical Engineering Science,* 34**,** 17-30.

HUANG, S., STOTT, A., GREEN, R. & BECK, M. 1988. Electronic transducers for industrial measurement of low value capacitances. *Journal of Physics E: Scientific Instruments,* 21**,** 242.

HUBBARD, M. & DUKLER, A. 1966. The characterization of flow regimes for horizontal two-phase flow. *Proceedings of the 1996 Heat Transfer and Fluid***,** 100-121.

HUBBARD, M. G. 1965. *An analysis of horizontal gas-liquid slug.* University of Houston, Tex.

ISHII, M. 1975. *Thermo-fluid dynamic theory of two-phase flow,* [Paris], Eyrolles.

ISHII, M. & HIBIKI, T. 2010. *Thermo-fluid dynamics of two-phase flow,* Springer Science & Business Media.

ISSA, R. I. & GALLENI, F. 2015. MECHANISTIC SIMULATION OF SLUG FLOW IN VERTICAL PIPES USING THE ONE-DIMENSIONAL TWO-FLUID MODEL. 27**,** 229-245.

KAJI, R., AZZOPARDI, B. J. & LUCAS, D. 2009. Investigation of flow development of co-current gas–liquid vertical slug flow. *International Journal of Multiphase Flow,* 35**,** 335-348.

KANU, A. 2013. *Characterisation of churn flow coalescers (CFC) in vertical pipes.* University of Nottingham.

LEGIUS, H. J. W. M., VAN DEN AKKER, H. E. A. & NARUMO, T. 1997. Measurements on wave propagation and bubble and slug velocities in cocurrent upward two-phase flow. *Experimental Thermal and Fluid Science,* 15**,** 267-278.

MALNES, D. 1983. *Slug Flow in Vertical, Horizontal and Inclined Pipes*, Institute for Energy Technology.

MATTAR, L. & GREGORY, G. 1974. Air-oil slug flow in an upward-inclined pipe-I: Slug velocity, holdup and pressure gradient. *Journal of Canadian Petroleum Technology,* 13.

MISHIMA, K. & ISHII, M. 1984. Flow regime transition criteria for upward two-phase flow in vertical tubes. *International Journal of Heat and Mass Transfer,* 27**,** 723-737.

MOORE, E. H. 1920. On the Reciprocal of the General Algebraic Matrix. *Bulletin of the American Mathematical Society*.

NICHOLSON, M., AZIZ, K. & GREGORY, G. 1978. Intermittent two phase flow in horizontal pipes: predictive models. *The Canadian Journal of chemical engineering,* 56**,** 653-663.

NICKLIN, D., WILKES, J. & DAVIDSON, J. 1962. Two-phase flow in vertical tubes. *Trans. Inst. Chem. Eng,* 40**,** 61-68.

OHNUKI, A. & AKIMOTO, H. 1996. An experimental study on developing air-water two-phase flow along a large vertical pipe: effect of air injection method. *International Journal of Multiphase Flow,* 22**,** 1143-1154.

OMEBERE-IYARI, N. K., AZZOPARDI, B. J., LUCAS, D., BEYER, M. & PRASSER, H. M. 2008. The characteristics of gas/liquid flow in large risers at high pressures. *International Journal of Multiphase Flow,* 34**,** 461-476.

PEÑA, H. F., BONILLA, A., HERNANDEZ, I. & RODRIGUEZ, O. 2013. Evaluation of Permittivity Models for Holdup Measurement of Viscous-Oil in Water Dispersed Flow. *In:* FLOW, T. I. C. O. M. (ed.) *8th International Conference on Multiphase Flow*. Jeju, Coreia do Sul.

PENROSE, R. A generalized inverse for matrices. Proc. Cambridge Philos. Soc, 1955. Cambridge Univ Press, 406-413.

PRASSER, H.-M., KREPPER, E. & LUCAS, D. 2002. Evolution of the two-phase flow in a vertical tube—decomposition of gas fraction profiles according to bubble size classes using wire-mesh sensors. *International journal of thermal sciences,* 41**,** 17-28.

PRASSER, H. M., BÖTTGER, A. & ZSCHAU, J. 1998. A new electrode-mesh tomograph for gas–liquid flows. *Flow Measurement and Instrumentation,* 9**,** 111-119.

PRASSER, H. M., MISAWA, M. & TISEANU, I. 2005. Comparison between wire-mesh sensor and ultra-fast X-ray tomograph for an air–water flow in a vertical pipe. *Flow Measurement and Instrumentation,* 16**,** 73-83.

PRASSER, H. M., SCHOLZ, D. & ZIPPE, C. 2001. Bubble size measurement using wire-mesh sensors. *Flow Measurement and Instrumentation,* 12**,** 299-312.

SHARAF, S., DA SILVA, M., HAMPEL, U., ZIPPE, C., BEYER, M. & AZZOPARDI, B. 2011. Comparison between wire mesh sensor and gamma densitometry void measurements in two-phase flows. *Measurement Science and Technology,* 22**,** 104019.

SIMPSON, H., ROONEY, D., GRATTAN, E. & ALSAMARRAE, F. 1981. Two-phase flow studies in large diameter horizontal tubes. *NASA STI/Recon Technical Report N,* 82**,** 23507.

SINGH, G. & GRIFFITH, P. 1970. Determination of the pressure drop optimum pipe size for a two-phase slug flow in an inclined pipe. *Journal of Engineering for Industry,* 92**,** 717-726.

SPEDDING, P., CHEN, J. & NGUYEN, V. T. 1982. Pressure drop in two phase gas-liquid flow in inclined pipes. *International Journal of Multiphase Flow,* 8**,** 407-431.

TAITEL, Y., BORNEA, D. & DUKLER, A. 1980. Modelling flow pattern transitions for steady upward gas-liquid flow in vertical tubes. *AIChE Journal,* 26**,** 345-354.

TAITEL, Y. & DUKLER, A. 1976. A model for predicting flow regime transitions in horizontal and near horizontal gas-liquid flow. *AIChE Journal,* 22**,** 47-55.

VAN HOUT, R., SHEMER, L. & BARNEA, D. 2003. Evolution of hydrodynamic and statistical parameters of gas–liquid slug flow along inclined pipes. *Chemical Engineering Science,* 58**,** 115-133.

WALLIS, G. B. 1969. *One-dimensional two-phase flow*, McGraw-Hill New York.

WALTRICH, P. J., FALCONE, G. & BARBOSA JR, J. R. 2013. Axial development of annular, churn and slug flows in a long vertical tube. *International Journal of Multiphase Flow,* 57**,** 38-48.

WEBER, M. E. 1981. Drift in intermittent two-phase flow in horizontal pipes. *The Canadian Journal of chemical engineering,* 59**,** 398-399.

WEISMAN, J. 1983. Two-phase flow patterns. *In:* CHEREMISINOFF, N. P. & GUPTA, R. (eds.) *Handbook of Fluids in Motion.* Ann Arbor Science Publ.

WEISMAN, J. & KANG, S. 1981. Flow pattern transitions in vertical and upwardly inclined lines. *International Journal of Multiphase Flow,* 7**,** 271-291.

WELCH, P. 1967. The use of fast Fourier transform for the estimation of power spectra: a method based on time averaging over short, modified periodograms. *IEEE Transactions on audio and electroacoustics,* 15**,** 70-73.

WIENER, O. 1910. Zur Theorie der Refraktionskonstanten. *Berichte über die Verhandlungen der Königlich-Sächsischen Gesellschaft der Wisseschaften zu Leipzig,* 62**,** 256–277.

YAN, H., LIU, C. & GAO, J. Electrical capacitance tomography image reconstruction based on singular value decomposition. Intelligent Control and Automation, 2004. WCICA 2004. Fifth World Congress on, 2004. IEEE, 3783-376a Vol. 4.

YANG, W. & PENG, L. 2003. Image reconstruction algorithms for electrical capacitance tomography. *Measurement Science and Technology,* 14**,** R1.

ZABARAS, G. Prediction of slug frequency for gas-liquid flows. SPE Annual Technical Conference and Exhibition, 1999. Society of Petroleum Engineers.

ZHENG, D. & CHE, D. 2006. Experimental study on hydrodynamic characteristics of upward gas–liquid slug flow. *International Journal of Multiphase Flow,* 32**,** 1191-1218.

ZUBER, N. & FINDLAY, J. 1965. Average volumetric concentration in two-phase flow systems. *Journal of heat transfer,* 87**,** 453-468.

ZUKOSKI, E. 1966. Influence of viscosity, surface tension, and inclination angle on motion of long bubbles in closed tubes. *Journal of Fluid Mechanics*, 25**,** 821-837.

A. ANALYSIS OF ERRORS

There are two types of data considered in the error analysis, the data read directly with the measuring instruments such as: flowmeters, pressure gauges or the WMS and ECT sensors; and the data calculated from the measured quantities, for example: velocity of the gas structures or the gas superficial velocity corrected by pressure. The uncertainty of direct measurements is embedded in the error of the instrument that measures. On the other hand, the uncertainty of the indirect measurements, R, that is dependent of x_i variables $R(x_1, x_2, x_3, \dots x_n)$, is calculated as:

$$\Delta R = \sum_{i=1}^{n} \left| \frac{\delta R}{\delta x_i} \Delta x_i \right|$$

Where ΔR is the error of the variable R, and Δx_i are the errors of the variables x_i .

A.1. Uncertainty of the liquid superficial velocity

The liquid superficial velocity is calculated as:

$$U_{ls} = \frac{\frac{Q_l}{60000}}{\pi \frac{D^2}{4}}$$

Where $Q_l$the volumetric flow read from the flowmeter in litres per minute and D is the diameter of the pipe measured with a calibre. The error of the liquid superficial velocity can be calculated then as:

$$\Delta U_{ls} = \frac{\frac{1}{60000}}{\pi \frac{D^2}{4}} \Delta Q_l + \frac{2 \frac{Q_l}{60000}}{\pi \frac{D^3}{4}} \Delta D$$

The error of the diameter of the pipe was found to be 0.1 mm and the error of the volumetric liquid flow ΔQ_l varies with the flowmeter used.

	Type	Rig	Range Q_l	Error ΔQ_l
Flowmeter 1	Volume	67	0 – 10 l/min	0.2 l/min
Flowmeter 1	Volume	67	24 – 100 l/min	2 l/min
Flowmeter 2	Mass	127	0 – 1670 l/min	2%

A.2. Uncertainty of the gas superficial velocity

The volumetric flowmeters measure in litres per minute. They were calibrated at the atmospheric pressure, therefore their measurements had to be corrected since the gas line was at an elevated pressure (P). The mass flowmeters measured the flow in normal litres per minute, therefore no correction is required for the pressure. The gas superficial velocity is calculated from the readings of the gas flowmeter as:

$$U_{gs} = \frac{\frac{Q_g}{6000}}{\pi\frac{D^2}{4}} = \frac{\frac{Q'_g}{6000}\sqrt{\frac{P}{P_0}}}{\pi\frac{D^2}{4}}$$

Where Q'_g the volumetric flow obtained from the flowmeter, P is the pressure of the gas after the flowmeter, P_0 is the atmospheric pressure and D is the diameter of the pipe measured with a calibre. The error of the gas superficial velocity can be calculated therefore as:

$$\Delta U_{gs} = \frac{\frac{1}{60000}\sqrt{\frac{P}{P_0}}}{\pi\frac{D^2}{4}}\Delta Q'_g + \frac{\frac{Q'_g}{60000}\,2\sqrt{\frac{P}{P_0}}}{\pi\frac{D^3}{4}}\Delta D + \frac{\frac{Q'_g}{60000}\sqrt{\frac{1}{P_0}}}{2\sqrt{\frac{P}{P_0}}\pi\frac{D^2}{4}}\Delta P$$

The error of the diameter of the pipe was found to be 0.1 mm. The error of the pressure gauge ΔP is 0.04 bar while that of the volumetric liquid flow ΔQ_l depends of the flowmeter used.

	Type	Rig	Range of Q'_g	Error $\Delta Q'_g$
Flowmeter 1	Volume	67	10 – 100 l/min	1 l/min
Flowmeter 2	Volume	67	100 – 1000 l/min	10 l/min
Flowmeter 3	Mass	127	100-1670 l/min	0.5%+1.6 l/min

A.3. Uncertainty of the gas structure velocity

The velocity of the gas structures was calculated by dividing the distance between two planes of the ECT by the time that needed by the gas structure to advance from one plane to the other which can be expressed as:

$$U_b = \frac{d}{t}$$

Where *d* is the distance and *t* is the time. The error of the gas structure velocity ΔU_b is expressed as:

$$\Delta U_b = \frac{1}{t}\Delta d + \frac{2d}{t^2}\Delta t$$

Where Δd is 1 mm and Δt is the inverse of the acquisition frequency of the ECT.

B. EXPERIMENTAL MATRIX AND RESULTS

B.1. Experimental campaign 1 (Chapter 5)

Flow values and their uncertainty of the experiment in the 67 mm pipe

DIAMETER 67 mm							
	Q_l (l/min)	U_{ls} (m/s)	ΔU_{ls} (m/s)	Q_g (l/min)	P [bar]	U_{gs} (m/s)	ΔU_{gs} (m/s)
run 1	24	0.12	0.01	30	0.5	0.17	0.01
run 2	24	0.12	0.01	60	0.5	0.35	0.02
run 3	24	0.12	0.01	90	0.5	0.52	0.03
run 4	24	0.12	0.01	120	0.5	0.7	0.08
run 5	24	0.12	0.01	160	0.5	0.93	0.09
run 6	24	0.12	0.01	200	0.5	1.2	0.1
run 7	24	0.12	0.01	240	0.5	1.4	0.1
run 8	24	0.12	0.01	300	0.5	1.7	0.1
run 9	24	0.12	0.01	400	0.5	2.3	0.1
run 10	49	0.23	0.01	30	0.5	0.17	0.01
run 11	49	0.23	0.01	60	0.5	0.35	0.02
run 12	49	0.23	0.01	90	0.5	0.52	0.03
run 13	49	0.23	0.01	120	0.5	0.7	0.08
run 14	49	0.23	0.01	160	0.5	0.93	0.09
run 15	49	0.23	0.01	200	0.5	1.2	0.1
run 16	49	0.23	0.01	240	0.5	1.4	0.1
run 17	49	0.23	0.01	300	0.5	1.7	0.1
run 18	49	0.23	0.01	400	0.5	2.3	0.1
run 19	74	0.35	0.01	30	0.5	0.17	0.01
run 20	74	0.35	0.01	60	0.5	0.35	0.02
run 21	74	0.35	0.01	90	0.5	0.52	0.03
run 22	74	0.35	0.01	120	0.5	0.7	0.08
run 23	74	0.35	0.01	160	0.5	0.93	0.09
run 24	74	0.35	0.01	200	0.5	1.2	0.1
run 25	74	0.35	0.01	240	0.5	1.4	0.1
run 26	74	0.35	0.01	300	0.5	1.7	0.1
run 27	74	0.35	0.01	400	0.5	2.3	0.1
run 28	99	0.47	0.02	30	0.5	0.17	0.01
run 29	99	0.47	0.02	60	0.5	0.35	0.02
run 30	99	0.47	0.02	90	0.5	0.52	0.03
run 31	99	0.47	0.02	120	0.5	0.7	0.08
run 32	99	0.47	0.02	160	0.5	0.93	0.09
run 33	99	0.47	0.02	200	0.5	1.2	0.1
run 34	99	0.47	0.02	240	0.5	1.4	0.1
run 35	99	0.47	0.02	300	0.5	1.7	0.1
run 36	99	0.47	0.02	400	0.5	2.3	0.1

Results of the velocity and the frequency of the gas structures in the 67 mm pipe

DIAMETER 67 mm			
	U_b (m/s)	ΔU_b (m/s)	Freq (Hz)
run 1	0.95	0.03	1.7
run 2	1.22	0.05	1.9
run 3	1.44	0.06	1.9
run 4	1.68	0.08	2.1
run 5	1.9	0.1	2.2
run 6	2.2	0.1	2.0
run 7	2.36	0.06	2.0
run 8	2.54	0.06	2.0
run 9	2.92	0.08	2.2
run 10	1.10	0.04	2.5
run 11	1.37	0.06	2.4
run 12	1.62	0.08	2.3
run 13	1.9	0.1	2.5
run 14	2.1	0.1	2.5
run 15	2.3	0.1	2.6
run 16	2.64	0.07	2.5
run 17	2.83	0.08	2.4
run 18	3.12	0.09	2.3
run 19	1.16	0.04	2.9
run 20	1.44	0.06	2.9
run 21	1.65	0.08	2.7
run 22	1.9	0.1	2.8
run 23	2.2	0.1	2.8
run 24	2.5	0.2	2.8
run 25	2.66	0.07	2.8
run 26	2.87	0.08	2.8
run 27	3.3	0.1	2.8
run 28	1.27	0.05	3.4
run 29	1.53	0.07	3.3
run 30	1.78	0.09	3.2
run 31	2.1	0.1	3.1
run 32	2.3	0.1	3.2
run 33	2.5	0.2	3.3
run 34	2.94	0.08	3.2
run 35	3.02	0.09	3.1
run 36	3.5	0.1	2.9

Flow values and their uncertainty of the experiment in the 127 mm pipe

DIAMETER 127 mm						
	Q_l (l/min)	U_{ls} (m/s)	ΔU_{ls} (m/s)	Q_g (l/min)	U_{gs} (m/s)	ΔU_{gs} (m/s)
run 1	91	0.120	0.004	129	0.17	0.01
run 2	91	0.120	0.004	266	0.35	0.01
run 3	91	0.120	0.004	396	0.52	0.01
run 4	91	0.120	0.004	532	0.70	0.01
run 5	91	0.120	0.004	708	0.93	0.02
run 6	91	0.120	0.004	883	1.16	0.02
run 7	91	0.120	0.004	1058	1.39	0.02
run 8	91	0.120	0.004	1324	1.74	0.03
run 9	91	0.120	0.004	1674	2.20	0.03
run 10	175	0.23	0.01	129	0.17	0.01
run 11	175	0.23	0.01	266	0.35	0.01
run 12	175	0.23	0.01	396	0.52	0.01
run 13	175	0.23	0.01	533	0.70	0.01
run 14	175	0.23	0.01	708	0.93	0.02
run 15	175	0.23	0.01	883	1.16	0.02
run 16	175	0.23	0.01	1057	1.39	0.02
run 17	175	0.23	0.01	1324	1.74	0.03
run 18	175	0.23	0.01	1672	2.20	0.03
run 19	265	0.35	0.01	128	0.17	0.01
run 20	265	0.35	0.01	266	0.35	0.01
run 21	265	0.35	0.01	395	0.52	0.01
run 22	265	0.35	0.01	533	0.70	0.01
run 23	265	0.35	0.01	708	0.93	0.02
run 24	265	0.35	0.01	883	1.16	0.02
run 25	265	0.35	0.01	1058	1.39	0.02
run 26	265	0.35	0.01	1324	1.74	0.03
run 27	265	0.35	0.01	1672	2.20	0.03
run 28	357	0.47	0.02	129	0.17	0.01
run 29	357	0.47	0.02	266	0.35	0.01
run 30	357	0.47	0.02	395	0.52	0.01
run 31	357	0.47	0.02	533	0.70	0.01
run 32	357	0.47	0.02	708	0.93	0.02
run 33	357	0.47	0.02	883	1.16	0.02
run 34	357	0.47	0.02	1058	1.39	0.02
run 35	357	0.47	0.02	1324	1.74	0.03
run 36	357	0.47	0.02	1673	2.20	0.03

Results of the velocity and the frequency of the gas structures in the 127 mm pipe

DIAMETER 127 mm			
	U_b (m/s)	ΔU_b (m/s)	Freq. (Hz)
run 1	1.55	0.07	1.6
run 2	1.9	0.1	1.7
run 3	2.0	0.1	1.6
run 4	2.1	0.1	1.0
run 5	2.2	0.1	0.9
run 6	2.3	0.1	1.0
run 7	2.49	0.06	0.8
run 8	2.77	0.07	0.8
run 9	3.07	0.09	0.7
run 10	1.62	0.08	1.7
run 11	1.9	0.1	1.9
run 12	2.1	0.1	1.9
run 13	2.2	0.1	1.3
run 14	2.4	0.2	1.3
run 15	2.4	0.2	1.2
run 16	2.61	0.07	0.9
run 17	2.77	0.07	0.9
run 18	2.97	0.08	1.1
run 19	1.69	0.08	1.8
run 20	2.0	0.1	2.0
run 21	2.2	0.1	2.3
run 22	2.4	0.2	2.1
run 23	2.6	0.2	1.6
run 24	2.7	0.2	1.5
run 25	2.77	0.07	1.4
run 26	2.97	0.08	1.2
run 27	3.19	0.09	1.4
run 28	1.8	0.1	2.3
run 29	2.2	0.1	2.1
run 30	2.5	0.2	2.9
run 31	2.5	0.2	2.5
run 32	2.7	0.2	1.8
run 33	2.9	0.2	1.6
run 34	2.9	0.08	1.6
run 35	3.19	0.09	1.4
run 36	3.6	0.1	1.4

B.2. Experimental campaign 2 (Chapter 6)

Flow values and the uncertainty of the experiment of Chapter 6

	Q_l (l/min)	U_{ls} (m/s)	ΔU_{ls} (m/s)	Q_g (l/min)	P [bar]	U_{gs} (m/s)	ΔU_{gs} (m/s)
run 1	5	0.023	0.001	30	0.5	0.17	0.01
run 2	5	0.023	0.001	60	0.5	0.35	0.02
run 3	5	0.023	0.001	90	0.5	0.52	0.03
run 4	5	0.023	0.001	120	0.5	0.70	0.09
run 5	5	0.023	0.001	160	0.5	0.93	0.09
run 6	5	0.023	0.001	200	0.5	1.2	0.1
run 7	5	0.023	0.001	240	0.5	1.4	0.1
run 8	5	0.023	0.001	300	0.5	1.7	0.1
run 9	5	0.023	0.001	400	0.5	2.3	0.1
run 10	5	0.023	0.001	500	0.5	2.9	0.1
run 11	10	0.047	0.002	30	0.5	0.17	0.01
run 12	10	0.047	0.002	60	0.5	0.35	0.02
run 13	10	0.047	0.002	90	0.5	0.52	0.03
run 14	10	0.047	0.002	120	0.5	0.70	0.09
run 15	10	0.047	0.002	160	0.5	0.93	0.09
run 16	10	0.047	0.002	200	0.5	1.2	0.1
run 17	10	0.047	0.002	240	0.5	1.4	0.1
run 18	10	0.047	0.002	300	0.5	1.7	0.1
run 19	10	0.047	0.002	400	0.5	2.3	0.1
run 20	10	0.047	0.002	500	0.5	2.9	0.1
run 21	24	0.115	0.01	30	0.5	0.17	0.01
run 22	24	0.115	0.01	60	0.5	0.35	0.02
run 23	24	0.115	0.01	90	0.5	0.52	0.03
run 24	24	0.115	0.01	120	0.5	0.70	0.09
run 25	24	0.115	0.01	160	0.5	0.93	0.09
run 26	24	0.115	0.01	200	0.5	1.2	0.1
run 27	24	0.115	0.01	240	0.5	1.4	0.1
run 28	24	0.115	0.01	300	0.5	1.7	0.1
run 29	24	0.115	0.01	400	0.5	2.3	0.1
run 30	24	0.115	0.01	500	0.5	2.9	0.1
run 31	49	0.23	0.01	30	0.5	0.17	0.01
run 32	49	0.23	0.01	60	0.5	0.35	0.02
run 33	49	0.23	0.01	90	0.5	0.52	0.03
run 34	49	0.23	0.01	120	0.5	0.70	0.09
run 35	49	0.23	0.01	160	0.5	0.93	0.09
run 36	49	0.23	0.01	200	0.5	1.2	0.1
run 37	49	0.23	0.01	240	0.5	1.4	0.1
run 38	49	0.23	0.01	300	0.5	1.7	0.1
run 39	49	0.23	0.01	400	0.5	2.3	0.1
run 40	49	0.23	0.01	500	0.5	2.9	0.1

	Q_l (l/min)	U_{ls} (m/s)	ΔU_{ls} (m/s)	Q_g (l/min)	P (bar)	U_{gs} (m/s)	ΔU_{gs} (m/s)
run 41	74	0.35	0.01	30	0.5	0.17	0.01
run 42	74	0.35	0.01	60	0.5	0.35	0.02
run 43	74	0.35	0.01	90	0.5	0.52	0.03
run 44	74	0.35	0.01	120	0.5	0.70	0.09
run 45	74	0.35	0.01	160	0.5	0.93	0.09
run 46	74	0.35	0.01	200	0.5	1.2	0.1
run 47	74	0.35	0.01	240	0.5	1.4	0.1
run 48	74	0.35	0.01	300	0.5	1.7	0.1
run 49	74	0.35	0.01	400	0.5	2.3	0.1
run 50	74	0.35	0.01	500	0.5	2.9	0.1
run 51	99	0.47	0.02	30	0.5	0.17	0.01
run 52	99	0.47	0.02	60	0.5	0.35	0.02
run 53	99	0.47	0.02	90	0.5	0.52	0.03
run 54	99	0.47	0.02	120	0.5	0.70	0.09
run 55	99	0.47	0.02	160	0.5	0.93	0.09
run 56	99	0.47	0.02	200	0.5	1.2	0.1
run 57	99	0.47	0.02	240	0.5	1.4	0.1
run 58	99	0.47	0.02	300	0.5	1.7	0.1
run 59	99	0.47	0.02	400	0.5	2.3	0.1
run 60	99	0.47	0.02	500	0.5	2.9	0.1

Results of the velocity and the frequency of the gas structures in the 67 mm rig at different angle of inclination

Angle 0° (horizontal)							
	U_b (m/s)	ΔU_b (m/s)	Freq. (Hz)		U_b (m/s)	ΔU_b (m/s)	Freq. (Hz)
run 1	0.64	0.02	0.32	run 31	0.89	0.03	0.42
run 2	0.84	0.03	0.27	run 32	1.11	0.04	0.42
run 3	0.98	0.03	0.17	run 33	1.33	0.05	0.25
run 4	1.22	0.05	0.12	run 34	1.65	0.08	0.22
run 5	1.56	0.07	0.11	run 35	1.71	0.09	0.23
run 6	1.78	0.09	0.11	run 36	2.0	0.1	0.23
run 7	2.06	0.05	0.10	run 37	2.33	0.06	0.31
run 8	2.39	0.06	0.10	run 38	2.34	0.06	0.34
run 9	2.16	0.05	0.09	run 39	2.37	0.06	0.32
run 10	2.41	0.06	0.10	run 40	2.51	0.06	0.51
run 11	0.68	0.02	0.36	run 41	1.00	0.03	0.59
run 12	0.84	0.03	0.32	run 42	1.22	0.05	0.47
run 13	1.03	0.04	0.19	run 43	1.47	0.07	0.37
run 14	1.24	0.05	0.13	run 44	1.75	0.09	0.48
run 15	1.51	0.07	0.11	run 45	1.9	0.1	0.56
run 16	1.68	0.08	0.12	run 46	2.2	0.1	0.52
run 17	1.87	0.04	0.10	run 47	2.23	0.05	0.55
run 18	2.11	0.05	0.10	run 48	2.31	0.06	0.58
run 19	3.12	0.09	0.13	run 49	2.21	0.05	0.61
run 20	2.68	0.07	0.11	run 50	2.74	0.07	0.65
run 21	0.77	0.02	0.34	run 51	1.13	0.04	0.76
run 22	0.97	0.03	0.35	run 52	1.34	0.06	0.60
run 23	1.22	0.05	0.20	run 53	1.51	0.07	0.64
run 24	1.39	0.06	0.17	run 54	1.66	0.08	0.71
run 25	1.59	0.07	0.14	run 55	1.8	0.1	0.73
run 26	1.71	0.09	0.16	run 56	2.1	0.1	0.83
run 27	2.08	0.05	0.16	run 57	2.30	0.06	0.83
run 28	2.54	0.06	0.27	run 58	2.51	0.06	0.93
run 29	2.85	0.08	0.22	run 59	2.85	0.08	0.75
run 30	3.18	0.09	0.23	run 60	3.5	0.1	0.73

Angle 15°							
	U_b (m/s)	ΔU_b (m/s)	Freq. (Hz)		U_b (m/s)	ΔU_b (m/s)	Freq. (Hz)
run 1	0.92	0.03	0.9	run 31	1.03	0.04	1.6
run 2	1.05	0.04	0.8	run 32	1.25	0.05	1.2
run 3	1.19	0.04	0.6	run 33	1.44	0.06	1.0
run 4	1.51	0.07	0.5	run 34	1.78	0.09	0.8
run 5	1.75	0.09	0.5	run 35	2.0	0.1	0.8
run 6	1.98	0.1	0.5	run 36	2.3	0.1	0.8
run 7	2.46	0.06	0.5	run 37	2.66	0.07	0.9
run 8	2.85	0.08	0.6	run 38	2.87	0.08	0.8
run 9	3.49	0.1	0.5	run 39	3.5	0.1	0.8
run 10	3.87	0.1	0.5	run 40	4.2	0.1	0.8
run 11	0.87	0.03	1.1	run 41	1.13	0.04	1.8
run 12	1.09	0.04	0.8	run 42	1.33	0.05	1.5
run 13	1.22	0.05	0.7	run 43	1.53	0.07	1.1
run 14	1.51	0.07	0.6	run 44	1.82	0.09	1.1
run 15	1.71	0.09	0.5	run 45	2.1	0.1	1.0
run 16	2.12	0.1	0.6	run 46	2.4	0.2	1.1
run 17	2.39	0.06	0.6	run 47	2.68	0.07	0.9
run 18	2.87	0.08	0.6	run 48	2.97	0.08	0.9
run 19	3.56	0.1	0.6	run 49	3.6	0.1	0.8
run 20	4.14	0.1	0.5	run 50	4.2	0.1	0.8
run 21	0.98	0.03	1.4	run 51	1.19	0.04	2.2
run 22	1.14	0.04	0.9	run 52	1.44	0.06	1.7
run 23	1.27	0.05	0.8	run 53	1.65	0.08	1.4
run 24	1.62	0.08	0.7	run 54	1.9	0.1	1.3
run 25	1.85	0.1	0.6	run 55	2.2	0.1	1.1
run 26	2.12	0.1	0.6	run 56	2.5	0.2	1.2
run 27	2.49	0.06	0.7	run 57	2.78	0.07	1.0
run 28	2.70	0.07	0.6	run 58	2.97	0.08	1.1
run 29	3.42	0.1	0.6	run 59	3.6	0.1	1.0
run 30	4.00	0.1	0.6	run 60	4.1	0.1	0.9

Angle 30°							
	U_b (m/s)	ΔU_b (m/s)	Freq. (Hz)		U_b (m/s)	ΔU_b (m/s)	Freq. (Hz)
run 1	0.94	0.03	1.2	run 31	1.03	0.04	1.6
run 2	1.09	0.04	1.0	run 32	1.25	0.05	1.2
run 3	1.35	0.06	0.8	run 33	1.44	0.06	1.0
run 4	1.65	0.08	0.8	run 34	1.78	0.09	0.8
run 5	1.98	0.1	0.7	run 35	2.0	0.1	0.8
run 6	2.17	0.1	0.7	run 36	2.3	0.1	0.8
run 7	2.60	0.07	0.7	run 37	2.66	0.07	0.9
run 8	2.92	0.08	0.8	run 38	2.87	0.08	0.8
run 9	3.60	0.1	0.8	run 39	3.5	0.1	0.8
run 10	3.91	0.1	0.8	run 40	4.2	0.1	0.8
run 11	1.02	0.04	1.3	run 41	1.13	0.04	1.8
run 12	1.27	0.05	0.9	run 42	1.33	0.05	1.5
run 13	1.39	0.06	0.9	run 43	1.53	0.07	1.1
run 14	1.75	0.09	0.8	run 44	1.82	0.09	1.1
run 15	2.02	0.1	0.8	run 45	2.1	0.1	1.0
run 16	2.23	0.1	0.8	run 46	2.4	0.2	1.1
run 17	2.62	0.07	0.8	run 47	2.68	0.07	0.9
run 18	2.97	0.08	0.9	run 48	2.97	0.08	0.9
run 19	3.79	0.1	0.8	run 49	3.7	0.1	0.8
run 20	4.24	0.1	0.8	run 50	4.2	0.1	0.8
run 21	1.07	0.04	1.4	run 51	1.19	0.04	2.2
run 22	1.25	0.05	1.1	run 52	1.44	0.06	1.7
run 23	1.46	0.06	1.0	run 53	1.65	0.08	1.4
run 24	1.78	0.09	0.9	run 54	1.9	0.1	1.3
run 25	2.07	0.1	0.8	run 55	2.2	0.1	1.1
run 26	2.34	0.1	0.8	run 56	2.5	0.2	1.2
run 27	2.60	0.07	1.0	run 57	2.78	0.07	1.0
run 28	2.87	0.08	1.0	run 58	2.97	0.08	1.1
run 29	3.56	0.1	0.9	run 59	3.6	0.1	1.0
run 30	4.09	0.1	0.9	run 60	4.1	0.1	0.9

Angle 45°							
	U_b (m/s)	ΔU_b (m/s)	Freq. (Hz)		U_b (m/s)	ΔU_b (m/s)	Freq. (Hz)
run 1	0.98	0.03	1.3	run 31	1.29	0.05	2.1
run 2	1.22	0.05	1.0	run 32	1.44	0.06	1.5
run 3	1.46	0.06	1.0	run 33	1.68	0.08	1.4
run 4	1.78	0.09	0.9	run 34	2.0	0.1	1.3
run 5	2.07	0.1	1.0	run 35	2.2	0.1	1.2
run 6	2.28	0.1	1.0	run 36	2.5	0.2	1.4
run 7	2.64	0.07	1.1	run 37	2.74	0.07	1.4
run 8	3.12	0.09	1.0	run 38	3.07	0.09	1.4
run 9	3.67	0.1	1.0	run 39	3.6	0.1	1.3
run 10	4.24	0.1	1.0	run 40	4.1	0.1	1.2
run 11	1.07	0.04	1.4	run 41	1.39	0.06	2.4
run 12	1.25	0.05	1.0	run 42	1.59	0.07	1.8
run 13	1.41	0.06	1.0	run 43	1.75	0.09	1.6
run 14	1.82	0.09	1.0	run 44	2.1	0.1	1.6
run 15	2.07	0.1	1.0	run 45	2.3	0.1	1.5
run 16	2.47	0.2	1.0	run 46	2.5	0.2	1.5
run 17	2.64	0.07	1.0	run 47	2.83	0.08	1.6
run 18	3.07	0.09	1.0	run 48	3.18	0.09	1.5
run 19	3.75	0.1	1.0	run 49	3.9	0.1	1.4
run 20	3.96	0.1	1.0	run 50	4.2	0.1	1.5
run 21	1.16	0.04	1.5	run 51	1.48	0.07	2.9
run 22	1.31	0.05	1.2	run 52	1.68	0.08	2.2
run 23	1.56	0.07	1.2	run 53	1.8	0.1	1.9
run 24	1.93	0.1	1.1	run 54	2.1	0.1	1.9
run 25	2.17	0.1	1.1	run 55	2.4	0.2	1.9
run 26	2.47	0.2	1.2	run 56	2.6	0.2	1.8
run 27	2.70	0.07	1.1	run 57	2.97	0.08	1.6
run 28	3.07	0.09	1.1	run 58	3.3	0.1	1.7
run 29	3.56	0.1	1.0	run 59	3.7	0.1	1.7
run 30	4.24	0.1	1.0	run 60	4.1	0.1	1.7

Angle 60°							
	U_b (m/s)	ΔU_b (m/s)	Freq. (Hz)		U_b (m/s)	ΔU_b (m/s)	Freq. (Hz)
run 1	0.95	0.03	1.2	run 31	1.29	0.05	2.0
run 2	1.14	0.04	1.1	run 32	1.48	0.07	1.5
run 3	1.51	0.07	1.1	run 33	1.68	0.08	1.4
run 4	1.82	0.09	1.1	run 34	2.0	0.1	1.4
run 5	2.02	0.1	1.2	run 35	2.3	0.1	1.5
run 6	2.34	0.1	1.2	run 36	2.6	0.2	1.6
run 7	2.80	0.08	1.1	run 37	2.94	0.08	1.6
run 8	3.30	0.1	1.0	run 38	3.07	0.09	1.5
run 9	3.46	0.1	1.0	run 39	3.4	0.1	1.3
run 10	4.09	0.1	1.0	run 40	4.3	0.2	1.4
run 11	1.09	0.04	1.3	run 41	1.37	0.06	2.6
run 12	1.22	0.05	1.1	run 42	1.59	0.07	1.8
run 13	1.48	0.07	1.1	run 43	1.78	0.09	1.8
run 14	1.82	0.09	1.1	run 44	2.1	0.1	1.8
run 15	2.17	0.1	1.3	run 45	2.3	0.1	1.7
run 16	2.41	0.2	1.3	run 46	2.6	0.2	1.9
run 17	2.72	0.07	1.3	run 47	2.80	0.08	1.9
run 18	3.07	0.09	1.2	run 48	3.3	0.1	1.8
run 19	3.87	0.1	1.0	run 49	3.6	0.1	1.5
run 20	4.24	0.1	1.1	run 50	4.3	0.2	1.6
run 21	1.19	0.04	1.6	run 51	1.48	0.07	2.9
run 22	1.39	0.06	1.2	run 52	1.71	0.09	2.6
run 23	1.62	0.08	1.2	run 53	1.9	0.1	2.3
run 24	1.85	0.1	1.3	run 54	2.2	0.1	2.3
run 25	2.17	0.1	1.4	run 55	2.5	0.2	2.0
run 26	2.47	0.2	1.4	run 56	2.6	0.2	2.2
run 27	2.60	0.07	1.4	run 57	2.99	0.08	2.0
run 28	3.07	0.09	1.2	run 58	3.2	0.1	2.0
run 29	3.83	0.1	1.2	run 59	3.6	0.1	2.1
run 30	4.09	0.1	1.2	run 60	4.2	0.1	2.0

Angle 75°							
	U_b (m/s)	ΔU_b (m/s)	Freq. (Hz)		U_b (m/s)	ΔU_b (m/s)	Freq. (Hz)
run 1	0.98	0.03	1.1	run 31	1.20	0.05	2.1
run 2	1.20	0.05	1.1	run 32	1.53	0.07	1.8
run 3	1.39	0.06	1.2	run 33	1.71	0.09	1.7
run 4	1.71	0.09	1.3	run 34	2.0	0.1	1.7
run 5	1.98	0.1	1.3	run 35	2.3	0.1	1.8
run 6	2.42	0.2	1.3	run 36	2.6	0.2	1.9
run 7	2.66	0.07	1.2	run 37	2.78	0.07	1.9
run 8	3.10	0.09	1.2	run 38	2.97	0.08	1.8
run 9	3.67	0.1	1.1	run 39	3.7	0.1	1.7
run 10	3.91	0.1	1.1	run 40	4.2	0.1	1.6
run 11	0.97	0.03	1.2	run 41	1.32	0.05	2.8
run 12	1.29	0.05	1.2	run 42	1.59	0.07	2.3
run 13	1.46	0.06	1.1	run 43	1.82	0.09	2.4
run 14	1.78	0.09	1.3	run 44	2.1	0.1	2.1
run 15	2.07	0.1	1.4	run 45	2.3	0.1	2.2
run 16	2.34	0.1	1.3	run 46	2.6	0.2	2.3
run 17	2.62	0.07	1.3	run 47	2.87	0.08	2.1
run 18	3.07	0.09	1.3	run 48	3.18	0.09	2.1
run 19	3.56	0.1	1.2	run 49	3.7	0.1	1.8
run 20	3.96	0.1	1.2	run 50	4.0	0.1	1.8
run 21	1.09	0.04	1.4	run 51	1.41	0.06	3.5
run 22	1.35	0.06	1.4	run 52	1.71	0.09	3.3
run 23	1.59	0.07	1.3	run 53	1.82	0.09	3.1
run 24	1.89	0.1	1.5	run 54	2.2	0.1	2.9
run 25	2.12	0.1	1.5	run 55	2.5	0.2	2.7
run 26	2.41	0.2	1.5	run 56	2.5	0.2	2.7
run 27	2.62	0.07	1.4	run 57	2.94	0.08	2.5
run 28	2.87	0.08	1.4	run 58	3.3	0.1	2.6
run 29	3.56	0.1	1.3	run 59	3.6	0.1	2.4
run 30	4.14	0.1	1.2	run 60	4.3	0.2	2.1

Angle 90°							
	U_b (m/s)	ΔU_b (m/s)	Freq. (Hz)		U_b (m/s)	ΔU_b (m/s)	Freq. (Hz)
run 1	0.86	0.03	1.3	run 31	1.10	0.04	2.5
run 2	1.10	0.04	1.5	run 32	1.37	0.06	2.4
run 3	1.33	0.05	1.6	run 33	1.62	0.08	2.3
run 4	1.56	0.07	1.9	run 34	1.8	0.1	2.5
run 5	1.82	0.09	1.9	run 35	2.1	0.1	2.5
run 6	2.02	0.1	1.8	run 36	2.3	0.1	2.6
run 7	2.30	0.06	1.8	run 37	2.64	0.07	2.5
run 8	2.52	0.06	2.1	run 38	2.83	0.08	2.4
run 9	2.83	0.08	2.4	run 39	3.12	0.09	2.3
run 10	2.74	0.07	3.1	run 40	3.6	0.1	2.5
run 11	0.90	0.03	1.5	run 41	1.16	0.04	2.9
run 12	1.17	0.04	1.6	run 42	1.44	0.06	2.9
run 13	1.39	0.06	1.7	run 43	1.65	0.08	2.7
run 14	1.62	0.08	1.7	run 44	1.9	0.1	2.8
run 15	1.89	0.1	1.9	run 45	2.2	0.1	2.8
run 16	2.02	0.1	1.8	run 46	2.5	0.2	2.8
run 17	2.33	0.06	1.8	run 47	2.66	0.07	2.8
run 18	2.47	0.06	1.9	run 48	2.87	0.08	2.8
run 19	2.83	0.08	2.3	run 49	3.3	0.1	2.8
run 20	3.12	0.09	2.4	run 50	3.8	0.1	2.4
run 21	0.95	0.03	1.7	run 51	1.27	0.05	3.4
run 22	1.22	0.05	1.9	run 52	1.53	0.07	3.3
run 23	1.44	0.06	1.9	run 53	1.78	0.09	3.2
run 24	1.68	0.08	2.1	run 54	2.1	0.1	3.1
run 25	1.93	0.1	2.2	run 55	2.3	0.1	3.2
run 26	2.17	0.1	2.0	run 56	2.5	0.2	3.3
run 27	2.36	0.06	2.0	run 57	2.94	0.08	3.2
run 28	2.54	0.06	2.0	run 58	3.02	0.09	3.1
run 29	2.92	0.08	2.2	run 59	3.5	0.1	2.9
run 30	3.36	0.1	2.6	run 60	4.0	0.1	2.6

B.3. Experimental campaign 3 (Chapter 7)

Flow values and their uncertainty of the experiment of Chapter 7

	Q_l (l/min)	U_{ls} (m/s)	ΔU_{ls} (m/s)	Q_g (l/min)	P (bar)	U_{gs} (m/s)	ΔU_{gs} (m/s)
run 1	0	0	0	10	0.5	0.06	0.01
run 2	0	0	0	30	0.5	0.17	0.01
run 3	0	0	0	60	0.5	0.35	0.02
run 4	0	0	0	90	0.5	0.52	0.08
run 5	0	0	0	120	0.5	0.70	0.09
run 6	0	0	0	160	0.5	0.9	0.1
run 7	0	0	0	200	0.5	1.2	0.1
run 8	3	0.016	0.001	10	0.5	0.06	0.01
run 9	3	0.016	0.001	30	0.5	0.17	0.01
run 10	3	0.016	0.001	60	0.5	0.35	0.02
run 11	3	0.016	0.001	90	0.5	0.52	0.08
run 12	3	0.016	0.001	120	0.5	0.70	0.09
run 13	3	0.016	0.001	160	0.5	0.9	0.1
run 14	3	0.016	0.001	200	0.5	1.2	0.1
run 15	7	0.031	0.001	10	0.5	0.06	0.01
run 16	7	0.031	0.001	30	0.5	0.17	0.01
run 17	7	0.031	0.001	60	0.5	0.35	0.02
run 18	7	0.031	0.001	90	0.5	0.52	0.08
run 19	7	0.031	0.001	120	0.5	0.70	0.09
run 20	7	0.031	0.001	160	0.5	0.9	0.1
run 21	7	0.031	0.001	200	0.5	1.2	0.1
run 22	10	0.047	0.002	10	0.5	0.06	0.01
run 23	10	0.047	0.002	30	0.5	0.17	0.01
run 24	10	0.047	0.002	60	0.5	0.35	0.02
run 25	10	0.047	0.002	90	0.5	0.52	0.08
run 26	10	0.047	0.002	120	0.5	0.70	0.09
run 27	10	0.047	0.002	160	0.5	0.9	0.1
run 28	10	0.047	0.002	200	0.5	1.2	0.1
run 29	49	0.23	0.01	10	0.5	0.06	0.01
run 30	49	0.23	0.01	30	0.5	0.17	0.01
run 31	49	0.23	0.01	60	0.5	0.35	0.02
run 32	49	0.23	0.01	90	0.5	0.52	0.08
run 33	49	0.23	0.01	120	0.5	0.70	0.09
run 34	49	0.23	0.01	160	0.5	0.9	0.1
run 35	49	0.23	0.01	200	0.5	1.2	0.1
run 36	74	0.35	0.01	10	0.5	0.06	0.01
run 37	74	0.35	0.01	30	0.5	0.17	0.01
run 38	74	0.35	0.01	60	0.5	0.35	0.02
run 39	74	0.35	0.01	90	0.5	0.52	0.08
run 40	74	0.35	0.01	120	0.5	0.70	0.09
run 41	74	0.35	0.01	160	0.5	0.9	0.1
run 42	74	0.35	0.01	200	0.5	1.2	0.1
run 43	99	0.47	0.02	10	0.5	0.06	0.01

	Q_l (l/min)	U_{ls} (m/s)	ΔU_{ls} (m/s)	Q_g (l/min)	P (bar)	U_{gs} (m/s)	ΔU_{gs} (m/s)
run 44	99	0.47	0.02	30	0.5	0.17	0.01
run 45	99	0.47	0.02	60	0.5	0.35	0.02
run 46	99	0.47	0.02	90	0.5	0.52	0.08
run 47	99	0.47	0.02	120	0.5	0.70	0.09
run 48	99	0.47	0.02	160	0.5	0.9	0.1
run 49	99	0.47	0.02	200	0.5	1.2	0.1